

EFFECT OF SOLID STATE DIFFUSION
ON
MICROSEGREGATION IN STEELS

MASTER OF ENGINEERING (1972)

McMASTER UNIVERSITY

(Metallurgy)

Hamilton, Ontario

TITLE: Effect of Solid State Diffusion on
Microsegregation in Steels

AUTHOR: Dipak Bhimrao Moharil, B. Tech. (Met. Eng.)
Indian Institute of Tech-
nology, Bombay)

SUPERVISOR: Professor G. R. Purdy

NUMBER OF PAGES: xiv, 136

SCOPE AND CONTENTS:

Controlled solidification of Fe-2wt% Ni binary and Fe-2 wt% Ni-Xwt%C ternary alloys was carried out in a travelling furnace. Metallographic studies were used to observe the effect of carbon on the morphology of growth. Electron probe microanalysis was carried out to obtain quantitative results on the microsegregation of Ni in the binary and ternary alloys. The extent of homogenisation of Ni, occurring both during and after solidification was quantitatively estimated.

ACKNOWLEDGEMENT

I wish to express a deep sense of gratitude to Dr. G. R. Purdy for suggesting this research topic, and his encouragement and guidance throughout this work. I would specially like to thank my colleague Mr. Iljoon Jin, whose advice and help in all phases of this work proved invaluable.

Finally, I am grateful to the technical staff of the Department of Metallurgy and Materials Science, McMaster University, for their help in the experimental work and to American Iron and Steel Institute for their financial support.

CONTENTS

<u>Chapter</u>	<u>Title</u>	<u>Page</u>
1	INTRODUCTION	1
2	REVIEW OF LITERATURE	3
	2.1 Basic Solidification Process	3
	2.2 Redistribution of Solute during Solidification	4
	2.3 Transitions in Segregation Structure	8
	2.4 Microsegregation of Solute in Dendritic Solidification	13
	2.5 Effect of Carbon on Microsegregation of Elements	18
	2.6 Homogenisation of Solute After Solidification	22
3	THEORETICAL CONSIDERATIONS	28
	3.1 Phase Diagram Study	28
	3.1.1 Fe-Ni Binary Phase Diagram	28
	3.1.2 Fe-C Binary Phase Diagram	29
	3.1.3 Fe-Ni-C System, Liquidus and Solidus Relationships	29
	3.2 Microsegregation Model and Segregation Paths in Ternary	30
	3.3 Object of Present Investigation	35

<u>Chapter</u>	<u>Title</u>	<u>Page</u>
4	EXPERIMENTAL TECHNIQUES	37
	4.1 Solidification Apparatus	37
	4.2 Diffusion Experiment	38
	4.3 Solidification Experiments	39
	4.3.1 Casting Experiments	39
	4.3.2 Controlled Solidification Experiments	40
	4.4 Metallographic Preparation of Specimens	41
	4.5 Preparation of Probe Standards	42
	4.6 Electron Probe Microanalysis	43
5	RESULTS AND DISCUSSION	45
	5.1 Diffusivity of Ni in δ -Fe	46
	5.2 Solidification	48
	5.2.1 Casting Studies	48
	5.2.2 Controlled Solidification Studies	52
6	CONCLUSIONS	71
	REFERENCES	72
	TABLES	76
	FIGURES	93

LIST OF TABLES

<u>Table</u>		<u>Page</u>
3.2.1	Scheil Chipman Plot for Ni in Fe-2.06 wt% Ni Binary Alloy	76
3.2.2	Scheil Chipman Plot for Ni in Fe-2.01 wt% Ni -0.58 wt% C ternary alloy	77
3.2.3	Scheil Chipman Plot for C in Fe-2.01 wt% Ni -0.58 wt% C Ternary Alloy	78
4.2.1	Chemical Analysis of Materials used in the Preparation of Alloy Specimens	79
4.3.1	Analysis of Alloys used for Directional Solidification Studies (for microprobe studies)	80
5.1.1 (a)	Electron Microprobe Data on Fe-Fe-2 wt% Ni Diffusion Couple Reacted at 1473 ^o C for 1800 secs.	81
(b)	Concentration Penetration Curve of Ni at 1473 ^o C	81
5.1.2 (a)	Electron Microprobe Data on Fe-Fe-2 wt% Ni Diffusion Couple Reacted at 1484 ^o C for 1500 secs.	82
(b)	Concentration Penetration Curve of Ni at 1484 ^o C	82
5.1.3 (a)	Electron Microprobe Data on Fe-Fe-2 wt% Ni Diffusion Couple Reacted at 1494 ^o C for 1200 secs.	83
(b)	Concentration Penetration Curve of Ni at 1494 ^o C	83

<u>Table</u>	<u>Page</u>
5.1.4 (a) Diffusivity of Ni in δ -Fe	84
(b) Data for Arrhenius Plot for $D_{Ni}^{\delta-Fe}$	84
5.1.5 (a) Data on Diffusivities of Ni in Different Phases of Iron (α -Fe, γ -Fe, δ -Fe, Liquid-Fe)	85
(b) Activation Energies and D_0 values for Ni in α -Fe, γ -Fe and δ -Fe	86
5.2.1 (a) Electron Microprobe Data for Ni Concentration Profile in Fe-1.92 wt% Ni Alloy (Elliptical Button)	86
(b) Electron microprobe Data for Ni concentration Profile in Fe-2.04 wt% Ni-0.32 wt% C Alloy (Elliptical Button)	87
5.2.2 Segregation Indices of Ni in Fe-1.92 wt% Ni Binary and Fe-2.04 wt% Ni-0.32 wt% C Ternary Alloys (Elliptical Buttons)	87
5.2.3 Composition of Directionally Solidified Specimens	88
5.2.4 Electron Microprobe Data for Ni concentration Profiles for Ni in Fe-2.06 wt% Ni Alloy	88
(a) Top Transverse Section	88
(b) Bottom Transverse Section	89
5.2.5 Electron Microprobe Data for Ni Concentration Profiles in Fe-2.01 wt% Ni - 0.58 wt% C Alloy	89
(a) Top Transverse Section	89
(b) Bottom Transverse Section	90
5.2.6 Results on Microsegregation of Ni in Fe-2.06 wt% Ni Alloy	90

<u>Table</u>		<u>Page</u>
5.2.7	Results on Microsegregation of Ni in Fe-2.01 wt% Ni - 0.58 wt% C Alloy	91
5.2.8	Residual Segregation in Fe-2.06 wt% Ni Binary and Fe-2.01 wt% Ni - 0.58 wt% C Ternary Alloys.	91
5.2.9	Comparison of Segregation Indices of Ni in Fe-2.06 wt% Ni Binary and Fe-2.01 wt% Ni -0.58 wt% C Ternary alloys.	92

LIST OF FIGURES

<u>Figure</u>		<u>Page</u>
2.2.1	(a) } Solidus liquidus relationships for a (b) } dilute binary alloy (c) Relationships between equilibrium compositions of solid and liquid	93
2.2.2	(a) Geometry of unidirectional solidification (b) } Steady state distribution of solute (c) } (d) Distribution of solute during uniaxial solidification	94
2.2.3	Distribution of solute during initial transient	95
2.2.4	(a) Distribution of solute during terminal transient (b) Final solute distribution (c) Effect of mixing on diffusion zone	96
2.3.1	(a) Variation of concentration and liquidus temperature ahead of solid-liquid interface (b) Constitutional supercooling ahead of planar interface (c) Development of cellular Interface	97
2.3.2	Conditions for cellular solidification	98
3.1.1	Peritectic region of Fe-Ni binary equilibrium diagram and tie line section for ternary	99

<u>Figure</u>		<u>Page</u>
3.1.2	Peritectic region of Fe-C binary equilibrium diagram	100
3.1.3 (a)	Liquidus surface of Fe-Ni-C system	101
(b)	Solidus surface of Fe-Ni-C system	
3.2.1 (a)	Mass balance at the S-L interface in unidirectional solidification assuming complete mixing in liquid.	102
(b)	Scheil Chipman plot for Ni in Fe-2.06% Ni binary alloy	
3.2.2 (a)	Mass balance at the S-L interface in unidirectional solidification assuming complete mixing in both solid and liquid	103
(b)	Scheil Chipman plots for Ni and C in Fe-2.01% Ni-0.58% C ternary alloy	
3.2.3	Segregation paths for Fe-2.01% Ni-0.58% C ternary alloy	104 105
4.1.1	Sectional view of the resistance furnace	106
4.2.1	Temperature Profile for diffusivity experiment	107
4.3.1	Temperature profile for a solidification run	108
4.3.2	Sectional view of the sample assembly	109
5.1.1	Ni concentration penetration curve for Fe-Fe-2 wt% Ni diffusion couple reacted at 1473 ^o C for 1800 seconds	110
5.1.2	Ni concentration penetration curve for Fe-Fe-2 wt% Ni diffusion couple reacted at 1484 ^o C for 1500 seconds	111

<u>Figure</u>		<u>Page</u>
5.1.3	Ni concentration penetration curve for Fe-Fe-2 wt% Ni diffusion couple reacted at 1494°C for 1200 seconds	112
5.1.4	Temperature dependence of $D_{Ni}^{\delta-Fe}$	113
5.1.5	Extrapolation of Arrhenius' plot for $D_{Ni}^{\alpha-Fe}$ to δ -Fe range	114
5.1.6	Ni diffusivities in different phases of Fe	115
5.2.1 (a)	Growth morphology in Fe-1.92 wt% Ni alloy (Argon arc ingot section parallel to overall growth direction)	116
(b)	Growth morphology in Fe-2.04% Ni- 0.207% C alloy (Argon arc ingot section parallel to overall growth direction)	
5.2.2 (a)	Directionally solidified portion of Fe-1.92 wt% Ni alloy (elliptical button solidified in Ar arc melting unit)	117
(b)	Directionally solidified portion of Fe-2.04 wt% Ni - 0.32 wt% C alloy	
(c)	Overall growth morphology in Fe-1.92 wt% Ni binary alloy (elliptical button)	118
(d)	Overall growth morphology in Fe-2.04 wt% Ni- 0.32 wt% C alloy	
5.2.3	Dendritic structure and Ni concentration profile in transverse section of Fe-1.92% Ni alloy (elliptical button)	119

<u>Figure</u>		<u>Page</u>
5.2.4	Dendritic structure and Ni concentration profile in transverse section of Fe-2.04% Ni -0.32% C alloy	120
5.2.5 (a)	Directionally solidified Fe-2.06 wt% Ni alloy, section parallel to macroscopic growth direction. $G = 22.7^{\circ}\text{C./cm}$ $R = 100 \text{ mm/hr}$	121
(b)	Directionally solidified Fe-1.98 wt% Ni -0.48 wt% C alloy, section parallel to macroscopic growth direction. $G = 22.7^{\circ}\text{C/cm}$ $R = 100 \text{ mm/hr.}$	
5.2.6 (a)	Directionally solidified Fe-2.01 wt% Ni -0.58 wt% C alloy, section parallel to macroscopic growth direction. $G = 22.7^{\circ}\text{C/cm}$ $R = 100 \text{ mm/hr.}$	122
(b)	Directionally solidified Fe-2.02 wt% Ni -0.4 wt% C alloy, section parallel to macroscopic growth direction. $G = 22.7^{\circ}\text{C/cm}$ $R = 100 \text{ mm/hr.}$	
5.2.7	Directionally solidified Fe-2.9028 wt% Ni alloy, section parallel to macroscopic growth direction. $G = 22.7^{\circ}\text{C/cm.}$ $R = 100 \text{ mm/hr.}$	123
5.2.8	Transverse sections of the directionally solidified Fe-2.06 wt% Ni alloy (a) top section, (b) 3.6 mm from top.	124
5.2.9	Transverse sections of the directionally solidified Fe-1.98 wt% Ni -0.48 wt % C alloy (a) top section (b) 3.1mm from top.	125

<u>Figure</u>		<u>Page</u>
5.2.10	Transverse sections of the directionally solidified Fe-2.02 wt% Ni - 0.4 wt% C alloy (a) top section (b) 5.1 mm from top.	126
5.2.11	Transverse sections of the directionally solidified Fe-2.01 wt% Ni-0.58 wt% C alloy (a) top section (b) 3.07 mm from top.	127
5.2.12 (a)	Dendritic structure and Ni concentration profile in the top transverse section of Fe-2.06 wt% Ni alloy	128
(b)	Dendritic structure and Ni concentration profile in the bottom transverse section of Fe-2.06 wt% Ni alloy	129
5.2.13	Dendritic structure and Ni concentration profile in the bottom transverse section of Fe-2.06 wt% alloy	130
5.2.14	Dendritic structure and Ni concentration profile in top transverse section of Fe-2.01 wt% Ni - 0.58 wt% C alloy	131
5.2.15	Dendritic structure and Ni concentration profile in bottom transverse section of Fe-2.01 wt% Ni - 0.58 wt% C alloy	132
5.2.16	Comparison of Scheil Chipman plot with the electron probe data for Fe-2.06 wt% Ni binary alloy.	133
5.2.17	Decay of the segregation profile in Fe-2.06 wt% Ni alloy	134

<u>Figure</u>		<u>Page</u>
5.2.18	Computed decay curves for the dendritic solidification for Fe-2.06% Ni alloy assuming cylindrical geometry	135
5.2.19	Homogenisation during solidification for Fe-2.06 wt% Ni Binary alloy	136

CHAPTER 1

INTRODUCTION

The purpose of this thesis is to study the micro-segregation and homogenisation of Ni in Fe-2% Ni binary and Fe-2% Ni -X%C ternary alloys under controlled solidification conditions which are maintained the same in both cases. Inspection of the phase diagram indicates that, during solidification, the binary alloy undergoes a L- δ transformation and the ternary alloy undergoes a L- γ transformation.

The influence of carbon on morphological aspects of the growth of solid phase and on the microsegregation of elements was previously studied by many investigators, but, the experimental conditions in terms of thermal gradient in liquid G , and rate of L-S interface advance R were not precisely defined in their work. Also, with an exception of the study of Fe-1.5% Cr-1%C system by Doherty and Melford²⁷, the effect of interaction of other solutes, which were present in their systems was not taken into account. These difficulties were avoided in the present work, by comparing the behaviour of Fe-2%Ni and Fe-2%Ni-C alloys under identical and controlled growth conditions.

The extent of back diffusion, which eventually results in a degree of homogenisation of the solute distribution, is essentially controlled by the diffusivity of solute

in the solid phase. This takes place both during and after solidification. The quantitative calculations on the experimental data show conclusively that the homogenisation occurring after solidification forms a major part of the total homogenisation effect for the binary alloy.

The experimental data obtained on the diffusivity of Ni in δ -Fe (designated as $D_{Ni}^{\delta-Fe}$) in this work, indicate that at the L-S transformation temperatures the value of $D_{Ni}^{\delta-Fe}$ is about two orders of magnitude higher than that of $D_{Ni}^{\gamma-Fe}$. This clearly implies that the extent of homogenisation after solidification is much higher in the binary alloy than in the ternary. This implication was confirmed by the experimental results obtained on the directionally solidified samples of these alloys.

Metallographic studies were used in qualitative observations on microsegregation, growth morphology and homogenisation of solute. Quantitative results were obtained through electron-probe microanalysis.

CHAPTER 2

REVIEW OF LITERATURE

This chapter begins with a review of the basic solidification process. Redistribution of the solute during solidification has been dealt with in detail. Micro segregation, arising from the instability of planar solid liquid interface has been studied by many investigators. A brief review of this is presented. In iron-base alloys the level of carbon plays a major role in determining the final solute distribution. Various studies on this aspect have been reviewed. Finally, a discussion of homogenisation of solute during and after solidification is presented.

2.1 Basic Solidification Process:

A brief definition of solidification can be given as a process in which a solid phase grows at the expense of a liquid.

Alloy solidification can be classified into three types:

- (i) Equilibrium solidification.
- (ii) Non-equilibrium solidification.
- (iii) Diffusionless solidification.

In the equilibrium solidification, participating phases are homogeneous and the transformation rates are extremely low.

The solidification products at a given temperature can be predicted from the average composition of the alloy, provided the phase diagram is known.

Non-equilibrium solidification occurs at higher transition rates; the phases are not homogeneous, and equilibrium may or may not be attained at the solid-liquid interface.

Diffusionless solidification occurs at still higher transformation rates; equilibrium does not obtain at the interface but the participating phases are homogeneous. Cole¹ has given an example of diffusionless solidification of an alloy. Biloni and Chalmers² have shown that when a liquid is supercooled below its solidus temperature solid forms with the same composition as that of the liquid.

For the purposes of this work, only equilibrium and non-equilibrium solidification will be reviewed in detail.

2.2 Redistribution of Solute During Solidification

It is convenient to start the discussion of the way in which the solute is redistributed by considering an idealised case in which the liquidus and solidus lines are both straight, as illustrated in Fig. 2.2.1. The salient feature of solid-liquid relationships can be described by a distribution coefficient k which can be defined in two ways: (i) equilibrium distribution coefficient (k_0) and (ii) effective distribution coefficient (k_E) which are defined as follows:

$$k_o = \frac{c_S}{c_L} \text{-----} \quad (2.2.1)$$

where c_S and c_L are obtained from the equilibrium diagram, and

$$k_E = \frac{c_S}{c_o} \text{-----} \quad (2.2.2)$$

where c_o is the average concentration of the liquid and c_S is again from the equilibrium diagram.

As can be seen from figs.2.2.1(a,b) k_o can be greater or less than unity. $k_o < 1$ is the most common case, but the analysis is essentially similar in both cases.

It is a necessary consequence of the equilibrium relationships between solids and liquids, that the composition of the liquid must change when solid is formed from it. If $k_o < 1$, solute will be rejected at the solid-liquid interface into the liquid. This gives rise to the segregation of solute, which has been studied mathematically in great detail.

Tiller et.al.³ have examined the segregation of solute under the following assumptions.

1. Diffusion in the solid is negligible.
2. The value of k_o (equilibrium is maintained at all times) is constant.
3. Mixing of the rejected solute in the liquid is by diffusion only (convection is negligible).
4. Solidification is unidirectional (Fig. 2.2.2a).

The distribution of solute in the liquid at any time takes the form shown in Fig. 2.2.2(d). A steady state con-

dition can exist between the amount of solute rejected at the solid-liquid interface and the one diffused away from it. Under these conditions, a solid of composition, the same as that of the original liquid will be formed as indicated in Fig. 2.2.2(b) and (c). The equation obtained at the interface is:

$$D \frac{d^2c}{dx^2} + R \frac{dc}{dx} = 0 \quad (2.2.3)$$

where; D = diffusivity of solute in liquid in cm^2/sec .

R = Rate of solid-liquid interface advance in cm/sec .

c = concentration of solute at distance x cms from the interface.

The solution to this equation is;

$$c_L = c_a \exp.(-\frac{R}{D} x') + c_o \quad (2.2.4)$$

where; c_o = original liquid composition.

At steady state; $c_a = \frac{c_o}{k_o}$.

Hence,

$$c_L = c_o [1 + \frac{1-k_o}{k_o} \exp.(-\frac{Rx'}{D})] \quad (2.2.5)$$

x' being the distance from the interface at which the solute concentration is c_L .

The first solid to form from a liquid of composition c_o must have a composition $k_o \cdot c_o$. Hence, the steady state condition will not be reached until the solidification has proceeded for a substantial amount of solute to have been rejected. This initial state is called the 'initial transient'.

Tiller et.al.³ described the composition of solid c_S as a function of distance by;

$$c_S = c_0 \{(1-k_0) [1 - \exp.(-k_0 \frac{R}{D} x)] + k_0\} . \quad (2.2.6)$$

This is illustrated in Fig. 2.2.3. It was later shown by Smith et. al.⁴ that the assumption of exponential approach to the steady state is not quite correct and the exact solution is:

$$\frac{c_S}{c_0} = \frac{1}{2} \left\{ 1 + \operatorname{erf} \left(\frac{\sqrt{(R/D)x}}{2} \right) + (2k_0 - 1) \exp. \left[-k_0 (1-k_0) \frac{R}{D} x \right] \right. \\ \left. \operatorname{erfc} \left[\frac{(2k_0 - 1) \sqrt{(R/D)x}}{2} \right] \right\} . \quad (2.2.7)$$

Once the steady state has been established, it will be maintained so long as ; (a) there is sufficient liquid ahead of the interface for the forward diffusion of solute to occur without hindrance and (b) R remains constant.

The first condition is not satisfied when the boundary of the liquid is approached as indicated in Fig. 2.2.4(a). It is evident that the concentration of the solid that is formed begins to rise above c_0 in order to accommodate the excess solute, which must all appear in the terminal region. Smith et.al.⁴ have shown that the concentration reached at the end of the terminal zone approaches the limit imposed by the alloy system as the quantity of liquid approaches zero. The overall solute distribution is shown in Fig. 2.2.4(b).

Another interesting case of solute redistribution

is to assume a complete or partial mixing of liquid and no diffusion in solid. Liquid is assumed to be completely mixed except that in the stagnation zone as indicated in Fig. 2.2.4(c). The concentration of solute in solid is given by²⁰;

$$c_S = k_E c_O (1-g)^{k_O - 1} \quad (2.2.8)$$

where; g = fraction of the liquid that has solidified

k_E = Effective distribution coefficient.

k_E is related to k_O by a relation

$$k_E = \frac{k_O}{k_O + (1-k_O) \exp. \left(-\frac{Rd}{D}\right)} \quad (2.2.9)$$

where, R = rate of the interface advance

D = diffusivity of the solute in the liquid

d = thickness of the stagnation zone.

$\frac{R \cdot d}{D}$ is a dimensionless number and is designated as 'normalized growth velocity'.

2.3 Transitions in Segregation Structure

As we have seen in section 2.2, the liquid in contact with an advancing solid-liquid interface, will in general have a composition that differs from that of the bulk liquid. Hence the liquidus temperature of the liquid in contact with the interface, is lower than that of the liquid at a greater distance from the interface. The consequence of this conclusion is that the temperature of the interface, in an alloy, is lower than the liquidus temperature of the bulk liquid. The solute distribution and the corresponding temperature

distribution ahead of the solid-liquid interface are indicated in Fig. 2.3.1(a). This corresponds to a case in which the whole of the liquid is at a temperature above that of the interface and yet the liquid is supercooled in the sense that it is below its liquidus temperature. Supercooling arising in this way is called "constitutional supercooling", which is diagrammatically illustrated in Fig. 2.3.1(b). A small amount of constitutional supercooling is enough to set up an instability in the steady state advance of the planar solid-liquid interface, which is schematically shown in Fig. 2.3.1(c). This instability of the solid-liquid interface is in fact responsible for the transitions in the segregation structure.

The principle of constitutional supercooling was first used by Rutter and Chalmers⁵ to explain the formation of cellular solidification front. The quantitative studies of this were done by Tiller et al³, who derived the following condition for no constitutional supercooling hence planar growth conditions.

$$\frac{G}{R} = \frac{mc_o}{D} \cdot \frac{1-k_o}{k_o} \quad (2.3.1)$$

for $\frac{G}{R} < \frac{mc_o}{D} \frac{1-k_o}{k_o}$ planar interface changes into cellular as indicated in Fig. 2.3.1. (c)

where; G = Actual temperature gradient in the liquid

c_o = Initial average composition of liquid

R = Rate of interface advance

k_0 = Equilibrium distribution coefficient

D = diffusivity of the solute in liquid.

This criterion has been extended to ternary systems by Coates et al.⁶. The data of Rutter⁷ on planar-cellular transition are indicated in Fig. 2.3.2. Although the parametric condition for planar-cellular transition is exactly determined, it is not so with cellular-cellular dendritic or cellular-dendritic transition.

Chalmers et al.⁸ first suggested that the dendritic structure was a development of the cellular structure and was induced by imposing a greater constitutional supercooling. Morris et al.⁹ undertook experiments on Pb-Sn alloys to determine the conditions of solidification under which the cellular to dendritic transition takes place. Their results indicated that it occurs at a definite $\frac{G}{R}$ ratio, for each composition. There was however a scatter in their results and there was apparently no co-relation between G , c_0 and R .

Tiller and Rutter¹⁰ showed that conditions corresponding to the onset of dendritic solidification were also dependent upon the crystallographic orientation of the solid with respect to macroscopic growth conditions. They studied the alloys of lead containing tin, silver and gold. For alloys of tin and lead, the limits of orientation range were

linear, when the average solute distribution was plotted as a function of the ratio $\frac{G}{\sqrt{R}}$.

$$c_o = B_H \frac{G}{\sqrt{R}} \quad (2.3.2)$$

and

$$c_o = B_L \frac{G}{\sqrt{R}} \quad (2.3.3)$$

where, B_H and B_L are proportionality constants and $B_L > B_H$. If $c_o > B_H \frac{G}{\sqrt{R}}$, cells of high misorientation with respect to the macroscopic growth direction broke down into dendrites, and if $c_o > B_L \frac{G}{\sqrt{R}}$ cells of low misorientation broke down into dendrites.

Tiller¹¹ later proposed a more explicit and a general criterion for transition,

$$\frac{G}{\sqrt{R}} = A' d_\theta \frac{c_o}{k_o} \quad (2.3.4)$$

where, A' = a proportionality constant

d_θ = width of the cells at breakdown for a particular orientation θ

k_o = equilibrium distribution coefficient

c_o = initial average composition .

Holmes et al.¹² obtained roughly coincident results with that of Tiller and Rutter¹⁰ for Pb-Sn alloys.

Coulthard and Elliott¹³ conducted experiments on alloys of lead-tin, lead-indium and tin-lead systems. They failed to establish a dependence of cell size on the solidification

parameters, in deciding the criterion for cellular-dendritic transition and hence they concluded that the validity of equation 2.3.4. can be doubted. However, they also concluded that the equation of the form

$$\frac{G}{R} \propto A_{\theta} \cdot \frac{c_0}{k_0} \quad (2.3.5)$$

where, A_{θ} = a proportionality constant, gave a better fit to the data.

A statistical and numerical analysis given by Davies¹⁴ indicated a general lack of significance in the measurements and also indicated an absence of a simple criterion to describe the transition.

In summary, it may be concluded from these studies that the formation of dendrites is favoured by increasing the constitutional supercooling i.e. by increasing c_0 and decreasing the $\frac{G}{R}$ ratio and k_0 . It is also favoured if the size and misorientation of the cells, which break down into dendrites, are large.

The experimental work on growth morphology of iron alloys, reported by Subramanian et.al.¹⁵ revealed that both the planar-cellular and cellular-cellular dendritic transitions occur in the same ingot. It was also concluded that, the constitutional supercooling steadily decreased throughout the process, probably as a result of reduction in growth rate and levelling of solute gradients in the small remaining volumes of the liquid.

Biloni¹⁶ reported following steps in the transition, planar - cellular - dendritic.

- (i) planar interface
- (ii) ordered nodes
- (iii) two dimensional or elongated cells
- (iv) regular or hexagonal cells
- (v) distorted cells or hexagonal cells with branches
- (vi) dendrites or cellular dendrites

2.4 Microsegregation of solute in dendritic solidification

As reviewed in section 2.3, the onset of constitutional supercooling produces an instability in the steady advance of a planar interface. The interface breaks down into cellular and eventually into cellular dendritic shape. This change in the interface morphology gives rise to a solute segregation which is perpendicular to the macroscopic direction of advance of the liquid solid front. This is essentially a short range segregation and hence, is called microsegregation. Microsegregation in dendritic freezing has been studied in substantial detail, because of its influence on mechanical and other properties of the castings and ingots. During solidification of the dendritic structure, solute is rejected into the interdendritic space and the centres of the dendrites are depleted of solute. Detailed studies²¹ on dendritic structures generally show that microsegregation is somewhat more severe between primary arms than between secondary arms.

Convenient quantitative measures of microsegregation of solute, which have been employed are:

- (i) minimum measured solute concentration; c_m
- (ii) maximum measured solute concentration; c_M
- (iii) segregation ratio $S = \frac{c_M}{c_m}$

and (iv) amount of non-equilibrium second phase

The simplest quantitative approach to determine the microsegregation in dendritically freezing alloys is the non-equilibrium lever rule derived by Scheil¹⁷, Gulliver¹⁸, Chipman¹⁹, Pfann²⁰ and others. The calculated solute distribution is given by:

$$C_S^* = K_O C_O (1-g)^{K_O-1} \quad (2.4.1)$$

where;

C_S^* = interface solute concentration in solid

K_O = equilibrium distribution coefficient

C_O = initial solute concentration

g = fraction solidified

The assumptions made in deriving eq. 2.4.1 are as follows:

(i) There is negligible undercooling before nucleation or from curvature and kinetic effects.

(ii) There is no mass flow in or out of the volume element considered.

(iii) Diffusion in the liquid within the volume element considered is complete (i.e. the liquid has a uniform composition

at any time).

(iv) The equilibrium partition coefficient K_0 is independent of concentration.

(v) Back diffusion in the solid is negligible. The equation 2.4.1 can be extended to any no. of non-interacting solutes in a system (Ref. 24)

$$C_{s_i}^* = K_{O_i} C_{O_i} (1-g)^{K_{O_i} - 1} \quad (2.4.2)$$

where; $i = 1, 2, \dots$

Some aspects of equation 2.4.1 are interesting:

(i) It is valid for systems which solidify slowly enough that the diffusion process levels the solute distribution in the liquid phase, but not so slowly, that diffusion in the solid becomes important.

(ii) It is independent of time.

(iii) It defines the maximum limit of segregation in the system.

The small scale of dendritic structure and the large differences in concentration between the initial and terminal transient regions, give rise to very steep concentration gradients in the alloy as it solidifies. It is therefore to be expected that some homogenisation should take place by diffusion while the alloy is solidifying and also in the post-solidification cooling period.

Brody and Flemings²¹ have studied the effect of homogenisation during solidification on solute redistribution.

Their equation is essentially a modified form of eq. 2.4.1. They made following assumptions in deriving the final solute distribution equation.

(i) Negligible undercooling before nucleation of solid phases or from curvature or kinetic effects.

(ii) No net flow of solute into or out of the volume element.

(iii) Complete diffusion in the liquid within the volume element.

(iv) Platelike dendrite morphology.

In addition to these basic assumptions they also assumed the following:

(i) Solute transport within the solid is by diffusion only.

(ii) Rate of thickening of dendrite is a continuous function (linear and parabolic rates of thickening were studied).

(iii) Liquid and solid densities are equal and constant.

The final equations that they obtained are as follows:

$$C_S^* = K_O \cdot C_O \left| 1 - \frac{g}{1 + \alpha_S K_O} \right|^{K_O - 1} \quad (2.4.3)$$

for linear rate of thickening and;

$$C_S^* = K_O \cdot C_O \left| 1 - (1 - 2\alpha_S K_O) g \right|^{\frac{K_O - 1}{1 - 2\alpha_S K_O}} \quad (2.4.4)$$

for parabolic rate of thickening.

$$\text{where; } \alpha_S = \frac{D_S \cdot t_f}{L^2}$$

and D_s = diffusivity of solute in liquid.

t_f = local solidification time

L = half the dendrite arm spacing.

The validity of assuming complete mixing in liquid was shown by considering a factor $\alpha_L = \frac{D_L \cdot t_f}{L^2}$ where, D_L = solute diffusivity in liquid. It was shown that α_L , which measures the extent of diffusion in liquid is usually $\gg 1$, and hence liquid can be assumed to have a uniform composition at any time. A reasonably good agreement was obtained between calculated and experimental results in the case of Al - 4.5% Cu alloy; provided a factor 0.32 was applied to the measured dendrite arm spacing.

Kirkwood and Evans²² have criticized the use of a correction factor of 0.32, applied by Brody and Flemings²¹ in their analysis and suggested that it could be obviated by choosing a diffusion coefficient about an order of magnitude larger. Murphy²³ has also commented upon the values of diffusivities used for these calculations and has shown that it is actually an order of magnitude higher than the value used by Brody and Flemings²¹.

A more comprehensive and precise model for solidification of a ternary system, which considers diffusion in both liquid and solid phases during solidification is given by Hone²⁴. It is based on the following assumptions.

- (i) The solidifying system is unidimensional and finite.
- (ii) The solid-liquid interface is planar
- (iii) Local equilibrium obtains at the interface.

(iv) The on-diagonal coefficients of the diffusion matrix are finite and constant for both phases.

(v) The off-diagonal coefficients are neglected.

(vi) The interface temperature is known as a function of time.

(vii) The tie-lines of the phase diagram are known.

For detailed calculations and equation for final solute distribution, a reference is made to the original work²⁴.

2.5 Effect of Carbon on Microsegregation of Elements

A first study of the influence of C on microsegregation of alloying elements in steel was reported by DeBeaulieu and Kohn²⁵. They studied the influence of carbon on segregation of As, Cr, Co, Cu, Mn, Mo and W, by autoradiography and did not detect any segregation of these elements in absence of carbon. A weak segregation of Cr, Co and Mo was observed in a melt containing 0.4wt%C. In the same melt, Cu, Mn, W segregated strongly and As was intensely segregated. They reasoned that this could be due to the increased range of solidification in presence of carbon, i.e. the difference between the liquidus and solidus temperatures.

Philibert et al.²⁶ observed that carbon influences the segregation index of the alloying elements in steel. The increasing order of influence was given as:

Ni, Mn, Si, Cr, Mo, As, Sn, P, Nb and S.

The influence of C on microsegregation of Ni was apparently not significant. However, a reasonably high value of segregation

index of Ni was evident in the case of steels containing other elements e.g. Cr, Mn etc. The Ni segregation index was as high as that of Cr and Mn in nickel-chrome steels. It was therefore suggested that the interaction parameter between the solute elements may be responsible for this.

The influence of carbon on segregation of X in Fe-C-X alloys was characterized by Philibert et al²⁶ by the thermodynamical interaction parameter between the two elements C and X in solution in iron, which was expressed as follows:

$$\epsilon_{\text{C}}^{\text{X}} = \left(\frac{\partial \log f_{\text{C}}}{\partial X} \right)_{\text{X}} \quad (2.5.1)$$

where; f_{C} = the activity coefficient of carbon

X = concentration of the alloying element.

From the experimental data, based on electron-microprobe analysis, it was concluded that the segregation index of element X in Fe-C-X alloys is higher, the higher the absolute value of the thermodynamical interaction parameter.

Two reasons were suggested to explain the correlation between the interaction parameter and the segregation index.

(i) The stronger the interaction, the broader is the solidification range and higher the concentration peak of the enriched layer.

(ii) This interaction also modifies the activity coefficient, changes the activity gradient of the alloying elements in the enriched layer and thus the diffusion flux; and finally the

thickness of this layer.

The double effect was thought to be responsible for the influence of carbon on the segregation ability of the alloying elements. The explanation however, is qualitative in nature.

A more detailed study of Fe-1%C-1.5% Cr system was conducted by Doherty and Melford²⁷, in which the influence of carbon on segregation index and equilibrium distribution coefficient of Cr was investigated. Their conclusions can be summarized in two parts.

(i) A series of ternary alloys were made up of Fe-1.5% Cr-X%C where X was varied from 0% to 2.2%C. The values of segregation index S were measured in each case. S increased steadily up to 1.5%C but afterwards it showed an apparent decrease.

(ii) The value of K_0 for chromium was obtained by equilibrating the alloy in liquid-solid region and brine quenching it; consequently, the concentrations of both liquid and solid were retained. Carbon decreased the value of K_0 up to 1.25%C but beyond this it showed an increase.

These experiments then confirmed the results of Philibert et al²⁶ viz. carbon increased the segregation index of chromium.

Weinberg and Buhr's²⁸ experiments on unidirectionally solidified castings of AISI 4340 steel (composition wt% 0.41%C - 0.95%Cr - 0.66% Mn - 0.28% Mo - 1.88% Ni - 0.010%P - 0.12%S - 0.35% Si) indicated that segregation indices of Mn and Cr

were affected by presence of carbon. Constitutional super-cooling calculations were used for the quantitative studies of influence of C on microsegregation.

Turkdogan and Grange²⁹ evaluated in an approximate manner the isothermal variation of the manganese distribution coefficient K_{Mn} as a function of carbon content at 1490°C in the γ -Fe-liquid region of the Fe-Mn-C system. Their results showed that K_{Mn} decreased by a factor of two as carbon content increased and hence, it enhanced the segregation of manganese. However, these calculations were shown to be in error by Hone²⁴ especially at low Mn and C concentrations.

Flemings et al.³⁰ studied the microsegregation of Fe-Cr, Fe-Cr-C, Fe-Ni and Fe-Ni-C alloys. It was found that the addition of carbon to an alloy containing 26% Ni did not make any difference to the segregation ratio of Ni, though it did enhance the segregation of Cr in Fe-1.5% Cr alloy.

In addition to its influence on the segregation index of the alloying elements carbon also affects the morphology of the resulting dendritic structure.

Subramanian et al.¹⁶ studied the growth morphology of Fe-base alloys. They found that the growth morphology is predominantly dendritic in the presence of carbon. Higher order of dendritic branching was also observed in the presence of carbon. It reduced the extent of back diffusion of solute and hence the extent of homogenisation during solidification.

Flemings et al³⁰ observed that addition of 0.4%C to Fe-26% Ni alloy produces dendrites that appear more fully developed. They reasoned that this might be due to the better etching provided. The morphologies of Fe-1.5% Cr-1%C and Fe-26%Ni - 0.4%C were similar to each other and comparable to the morphology of the AISI4340 steel studied by Weinburg and Buhr²⁸.

In a more recent study by Hone²⁴, on controlled solidification of Fe-Mn base alloys, it was shown that in Fe-Mn-C alloy, because of weak interaction between manganese and carbon both in liquid and solid the partition or distribution coefficients of Mn and C were only slightly affected. However, it was also concluded that the strong negative interaction of carbon with certain solute elements in steel enhances their segregation, especially in the final stage of solidification, where the interdendritic liquid is highly enriched.

2.6 Homogenisation of solute after solidification

As reviewed in the earlier sections of this chapter large concentration gradients are created due to the redistribution of solute during solidification. Back diffusion of solute takes place during solidification because of these concentration gradients. Homogenisation resulting from this back diffusion has been already dealt with in section 2.4. In this section an attempt is made to present some models proposed to study the homogenisation taking place after solidification.

Kattamis and Flemings³¹ in their studies on the homogenisation of low alloy steel, proposed a quantitative model which is based on the following assumptions:

- (i) There is a complete symmetry. Dendrites are columnar and are symmetrically placed.
- (ii) There is no mass transfer along the columnar growth direction. Hence, all the diffusion paths are horizontal, i.e. perpendicular to columnar growth direction.

The applicable diffusion equation is:

$$\frac{\partial^2 c}{\partial x^2} + \frac{\partial^2 c}{\partial y^2} = \frac{1}{D} \frac{\partial c}{\partial t} \quad (2.6.1)$$

where; c = solute concentration

x, y = dimensional co-ordinates

D = diffusion coefficient of solute ($\text{cm}^2/\text{sec.}$)

t = time (sec.)

The solution finally obtained for an arbitrary initial distribution after applying the proper boundary conditions is:

$$c(x, y, t) = \sum_{n=0}^{\infty} \sum_{m=0}^{\infty} \{K_{nm} \cos \left(\frac{n\pi x}{l} \right) \cos \left(\frac{m\pi y}{l'} \right) \times e^{-\left(\frac{n^2}{l^2} + \frac{m^2}{l'^2} \right) \pi^2 D t} + \bar{c} \quad (2.6.2)$$

where; \bar{c} = average solute concentration

l, l' = half dendrite arm spacings in x, y directions

$c(x, y, t)$ = solute concentration at a point (x, y) and time t .

and K_{nm} can be evaluated from the initial distribution function.

Equation 2.6.2 yields a solute concentration at any time t .

They also defined a factor to estimate the extent of homogenisation called as 'index of residual segregation', δ_i and given by

$$\delta_i = \frac{C_M^t - C_m^t}{C_M^o - C_m^o} \quad (2.6.3)$$

where; C_M^t, C_m^t = Maximum and minimum solute concentrations after time t .

C_M^o, C_m^o = Initial Maximum and minimum solute concentrations.

A good agreement between experimental results and the values predicted by the model was obtained for AISI 4340 steel. Index of residual segregation was found to be a single valued function of a dimensionless parameter ' $\frac{D_s \cdot t_h}{l^2}$ '

where; D_s = diffusion coefficient of the solute

t_h = homogenisation time

l = half the dendrite arm spacing.

Weinburg and Buhr³² used essentially similar approach to the homogenisation studies of AISI4340 steel. They described the reduction of amplitude of an initial sinusoidal solute distribution by an amplitude factor; f where f is given by

$$f = \frac{\text{original amplitude}}{\text{reduced amplitude}} = \frac{(H_t+1)(H_o-1)}{(H_t-1)(H_o+1)} \quad (2.6.4)$$

where $H_t = \frac{C_{\max}}{C_{\min}}$ at time t and $H_0 = \frac{C_{\max}}{C_{\min}}$ at $t = 0$

Time and temperature dependence of the amplitude factor f is given as $\frac{1}{f} = \exp.\left(\frac{-\pi^2 Dt}{l^2}\right)$ (2.6.5)

where, D = diffusivity of the segregating element

t = time of homogenisation

$2l$ = wavelength of the solute distribution.

Lavender and Jones³³ utilised the same approach in their studies on homogenisation. Ward³⁴ also employed the same quantitative analysis in his studies on homogenisation of Mn in manganese steels.

In their comprehensive paper on "Homogenisation by diffusion", Purdy and Kirkaldy³⁵ have treated both binary and multicomponent systems.

The basic diffusion equation is:

$$\frac{\partial c_1}{\partial t} = \text{div. } \tilde{D} \nabla c_1 = \tilde{D} \nabla^2 c_1 \quad (2.6.6)$$

where, \tilde{D} = diffusivity of the solute (assumed to be independent of concentration) .

Assuming the initial solute distribution to be sinusoidal and given by

$$c_1(x, 0) = \bar{c}_1 + A \sin \frac{\pi x}{l} \quad (2.6.7)$$

(the subscript '1' refers to solute '1').

where \bar{c}_1 = average solute concentration

A = amplitude of sinusoidal distribution

$2l$ = wavelength of solute distribution.

The general solution of equation 2.6.6 is given by

$$c_1(x,t) = \bar{c}_1 + A \sin\left(\frac{\pi x}{l}\right) \exp\left(-\frac{Dt\pi^2}{l^2}\right) \quad (2.6.8)$$

The characteristic time or the time required to reach $\frac{1}{e}$ times the original amplitude is given by

$$\tau = \frac{l^2}{\pi^2 D} \quad (2.6.9)$$

The solute concentration profile at any time can be represented as a sum of non-interacting sinusoidal components each associated with a characteristic time τ , proportional to the square of the wavelength.

A more general solution may be written as

$$c_1(x,t) = \bar{c}_1 + \int_{-\infty}^{+\infty} A(\bar{\beta}) e^{-\bar{\beta}^2 Dt} e^{i\bar{\beta}x} d\bar{\beta} \quad (2.6.10)$$

where $A(\bar{\beta})$ is obtained by the fourier transform of the initial distribution given by,

$$A(\bar{\beta}) = \frac{1}{2\pi} \int_{-\infty}^{+\infty} \{c_1(\bar{x}, 0) - \bar{c}_1\} e^{-i\bar{\beta}\bar{x}} d\bar{x} \quad (2.6.11)$$

where, $\bar{\beta}$ is the wave vector.

For a typical cellular solidification case, where cylindrical approximation is valid the concentration is given

by,

$$c(r,t) = \frac{2}{a^2} \left\{ \int_0^a r' f(r') dr' + \sum_{n=1}^{\infty} e^{-D\alpha_n^2 t} \frac{J_0(r\alpha_n)}{J_0^2(a\alpha_n)} \right. \\ \left. \times \int_0^a r' f(r') J_0(\alpha_n r) dr' \right\} \quad (2.6.12)$$

The quantitative calculations on a cellular solidification, in Fe-8 wt% Ni alloy (Jin and Purdy in Ref. 35) based on eq. 2.6.12 have been shown to agree with the experimental results. The equation 2.6.12 is applied in this study to dendritic solidification Fe-2.06 wt% Ni binary alloy, with the assumption of cylindrical geometry.

CHAPTER 3

THEORETICAL CONSIDERATIONS

This chapter briefly deals with the theoretical background essential for the study of modes of solidification in Fe-2 wt% Ni binary and Fe-2 wt% Ni-C ternary alloys. The binary alloy undergoes a Liquid- δ Fe transformation and the ternary a Liquid- γ Fe.

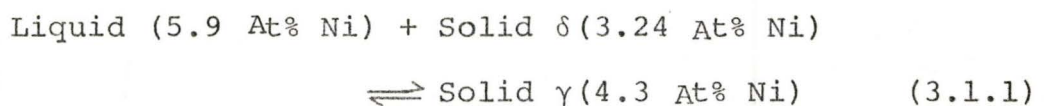
Initially, the nature of the relevant regions of Fe-Ni and Fe-C binary equilibrium phase diagrams is discussed. This is followed by a discussion on the liquidus and solidus relationships in Fe-Ni-C ternary system. A model has been presented for microsegregation in ternary and segregation paths have been determined for the same. Finally, a detailed statement of the object of this investigation is presented.

3.1 Phase Diagrams

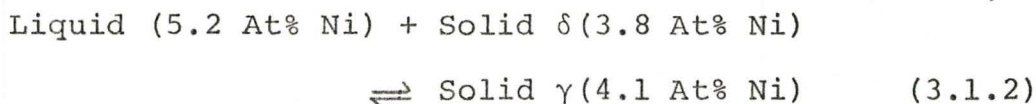
3.1.1 Fe-Ni Binary Equilibrium Diagram:

The high temperature (peritectic) region of the Fe-Ni equilibrium diagram has been shown in Fig. 3.1.1. The diagram is taken from Hansen³⁸.

The iron-nickel binary phase diagram is of the open γ -field type and δ Liquidus and solidus curves fall smoothly to a peritectic horizontal at 1512°C; corresponding to a reaction,



The peritectic reaction, reported by Hume Rothery and Helawell³⁹, which is slightly different from eq. 3.1.1 is as follows:

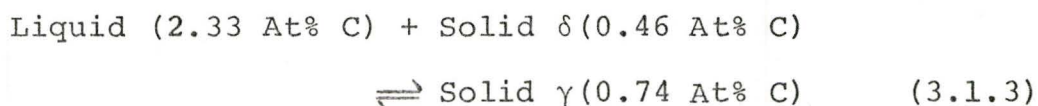


The peritectic temperature reported by them is 1511°C. According to fig. 3.1.1, the δ -Fe temperature range for Fe-2 wt% Ni alloy is 61°C.

3.1.2 Fe-C Binary Phase Diagram:

A large amount of work has been reported on Fe-C equilibrium diagram. The relevant region of the diagram has been indicated in fig. 3.1.2 (Hansen³⁸).

Kirkaldy and Purdy⁴⁰ have reformulated the metastable Fe-Fe₃C system, but the nature of the high temperature peritectic region is unchanged. The peritectic horizontal occurs at 1496°C and is governed by the reaction:



3.1.3 Fe-Ni-C System, Liquidus and Solidus Relationships

Marsh⁴¹ reviewed the early work on the ternary system Fe-Ni-C and outlined the general form of the diagram to be expected from the contiguous binary diagrams. Kase⁴² determined the liquidus surface of the ternary system up to the eutectic composition for carbon and to about 80% Ni, but the results were not reliable because of the use of impure

materials. Andrew and Bottomly⁴³ prepared alloys containing 0.4% C by weight and up to 20 wt% Ni. Liquidus, solidus and peritectic transformation temperatures were measured by thermal analysis. The figures were questionable because the figures given for the peritectic temperatures of the binary systems were inaccurate.

A recent and more precise analysis of the liquidus solidus relationships has been given by Buckley and Hume Rothery⁴⁴. They used thermal analysis technique and alloys containing up to 5 wt% carbon and 40 wt% nickel to determine the liquidus, solidus and peritectic transformation surfaces. The results of the thermal analysis arrests were plotted into the liquidus and solidus surfaces of Fe-C-Ni system which are shown in fig. 3.1.3 (a) and (b).

They made the following conclusions from their results:

(i) The δ -liquidus surface is almost planar so that this surface may be represented by a plane joining the two liquidus lines of the binary systems. The γ -liquidus surface is slightly curved with the concave face uppermost.

(ii) The δ -solidus surface is planar and the limit of δ -solid solubility follows a straight line course. The γ solidus surface falls very steeply from the nickel-rich side to the carbon-rich side of the system.

3.2 Microsegregation Model and segregation Paths in Ternary

For calculating the microsegregation of solute during alloy solidification the simplest approach that can be applied

is relating the solute concentration at the interface in the solid C_S^* with the fraction solidified g . This approach has been utilised by many workers to calculate the micro-segregation of solute.

As reviewed in section 2.4 the relation is expressed as

$$C_S^* = K_O C_O (1-g)^{K_O-1} \quad (3.2.1)$$

where;

C_S^* = Interface solute concentration in solid

K_O = Equilibrium Distribution Coefficient

C_O = Average Initial Solute Concentration

g = Fraction solidified

The equation is based on the following assumptions:

- (i) Solidification takes place unidirectionally
- (ii) back diffusion in the solid is negligible
- (iii) complete mixing exists in liquid at all times
- (iv) the equilibrium distribution coefficient is constant

The derivation of equation 3.2.1 consists in applying a mass balance at the liquid solid interface as indicated in fig. 3.2.1(a)

$$V_L dc_L^* = (C_L^* - C_S^*) (-dV_L) \quad (3.2.2)$$

where,

V_L = volume of the liquid

and C_L^* = interface solute concentration in the liquid

If the system has a unit cross section,

$$V_L = \lambda - z \quad (3.2.3)$$

hence,

$$(\lambda-z) dC_L^* = (C_L^* - C_S^*) dz \quad (3.2.4)$$

Now $g = \frac{z}{\lambda}$ (3.2.5)

and $C_L^* = \frac{C_S^*}{K_O}$ (3.2.6)

Substituting eqs. 3.2.5 and 3.2.6 in eq. 3.2.4 and integrating, we obtain,

$$K_O C_O \int_{C_S^*}^{C_S^*} \frac{dC_S^*}{C_S^*} = (1-K_O) \int_0^g \frac{dg}{1-g} \quad (3.2.7)$$

From this, eq. 3.2.1 can be easily deduced. Equation 3.2.1 has been plotted for Fe-Ni binary alloy (fig. 3.2.1(b)) with

$$K_O = 0.545$$

$$C_O = 2.06 \text{ wt\% Ni}$$

and $g = 0\% \text{ to } 90\%$

This equation can be easily extended to any number of solutes in a system, provided negligible interaction exists and hence solute distribution coefficients remain constant.

In case of a ternary alloy solidification, where the two solutes (designated '1' and '2') satisfy the above condition, their distributions can be described by two independent equations, viz.

$$C_{S1}^* = K_{O1} C_{O1} (1-g)^{K_{O1}-1} \quad (3.2.8)$$

$$C_{S2}^* = K_{O2} C_{O2} (1-g)^{K_{O2}-1} \quad (3.2.9)$$

Eliminating the common parameter 'g' we get;

$$g = 1 - \left(\frac{C_{s1}^*}{K_{O1} C_{O1}} \right) \frac{1}{K_{O1}^{-1}} \quad (3.2.10)$$

and

$$g = 1 - \left(\frac{C_{s2}^*}{K_{O2} C_{O2}} \right) \frac{1}{K_{O2}^{-1}} \quad (3.2.11)$$

Hence,

$$C_{s1}^* = K_{O1} C_{O1} \left(\frac{C_{s2}^*}{K_{O2} C_{O2}} \right) \frac{K_{O1}^{-1}}{K_{O2}^{-1}} \quad (3.2.12)$$

Equation 3.2.12 can be utilised in studying the relationship between the interface solute concentrations C_{s1}^* and C_{s2}^* in a ternary system.

For the specific case of Fe-Ni-C ternary, which is of prime interest in the present work, nickel (designated as solute '1') satisfies all the conditions required by eq. 3.2.1 and hence its distribution can be described as

$$C_{s1}^* = K_{O1} C_{O1} (1-g) K_{O1}^{-1} \quad (3.2.13)$$

However, in the case of carbon (solute '2') back diffusion coefficient in solid phase is also extremely high ($\sim 10^{-5}$ cm²/sec) and an additional assumption of complete back diffusion may be a reasonable approximation. The validity of this added assumption imposes different mass balance at the solid-liquid interface for carbon, which is shown in fig. 3.2.2(a).

The equation which applies in this case is:

$$(C_o - C_s^*)g = (C_L^* - C_o)(1-g) \quad (3.2.14)$$

substituting, $C_L^* = \frac{C_s^*}{K_o}$ (3.2.15)

we obtain, $C_s^* = \frac{K_o C_o}{1-g + K_o g}$ (3.2.16)

Since carbon is designated as solute '2', this equation is rewritten as

$$C_{s_2}^* = \frac{K_{o_2} C_{o_2}}{1-g + K_{o_2} g} \quad (3.2.17)$$

For negligible interaction between carbon and nickel

($\epsilon_{NiC} = \epsilon_{C-Ni} = +2.9$) the equations 3.2.17 and 3.2.13 have been plotted for Fe-Ni-C alloy in fig. 3.2.2(b), the data for which are as follows:

$$K_{o_1} = 0.67$$

$$C_{o_1} = 2.01 \text{ wt}\%$$

$$K_{o_2} = 0.315$$

$$C_{o_2} = 0.58 \text{ wt}\%$$

As stated earlier, equations 3.2.13 and 3.2.17 can be co-related to obtain the relationship between $C_{s_1}^*$ and $C_{s_2}^*$ by eliminating the common parameter 'g'. The equation obtained is:

$$C_{s_1}^* = K_{o_1} C_{o_1} \left[1 - \frac{C_{s_2}^* - K_{o_2} C_{o_2}}{(1-K_{o_2}) C_{s_2}^*} \right]^{K_{o_1} - 1} \quad (3.2.18)$$

The utility of the solute distribution equations can be extended to obtain the segregation paths in a ternary system. In the case of Fe-Ni-C system at a particular value of g , there exist two interface concentrations for the solutes in the solid phase corresponding to nickel and carbon. The values of $C_{S_i}^*$ can be computed from eqs. 3.2.17 and 3.2.13 and $C_{L_i}^*$ values can be obtained correspondingly. The paths obtained on the liquidus and solidus surfaces by using these values have been shown in fig. 3.2.3.

The segregation paths indicate a steady increase in the interface concentrations for both nickel and carbon. It is also apparent that the course of solidification for Fe-2.01 wt% Ni-0.58 wt% C alloy is completely of a liquid- γ -Fe type. It does not touch the peritectic surface at any time during solidification. The plots have been terminated at $g = 90\%$ because eq. 3.2.13 yields a meaningless result at the value of $g = 100\%$.

3.3 Object of Present Investigation

The main object of this work was to study the effect of solid state diffusion of solute on its microsegregation. For this, a comparative study of segregation of Ni in Fe-2 wt% Ni binary and Fe-2 wt% Ni-C ternary alloy, under identical and controlled solidification conditions was proposed.

During solidification, the binary alloy undergoes a L- δ transformation and the ternary alloy undergoes a L- γ one. Consequently, a higher degree of solute homogenization was expected in the binary alloy as compared to the ternary.

This could be studied through the concentration profiles of Ni, obtained by the electron probe microanalysis of the transverse sections of directionally solidified specimens.

The nature of the present study is basically different from the ones mentioned in section 2.5 in that the solidification conditions are more precisely defined (in terms of G and R) in this work. This facilitates the interpretation of the results obtained.

Similar to the study conducted by Doherty and Melford²⁷ on Fe-1.5% Cr - 1%C ternary alloy, the effect of interaction of solutes other than carbon on Ni segregation was eliminated by choosing the Fe-Ni-C ternary system. The effect of carbon on growth morphology was studied through metallographic techniques.

CHAPTER 4

EXPERIMENTAL TECHNIQUES

4.1 Solidification Apparatus:

A sectional view of the resistance furnace used for directional solidification studies is presented in fig. 4.1.1. The apparatus consists of a furnace drum of stainless steel encasing alumina powder insulation. The alumina furnace tube was held in vertical position by O-ring seals at the top and bottom. Mo wire (0.050 in. dia.) wound around the furnace tube and protected by 20% H₂-80%N₂ gas mixture, served as a heating element. The O-ring seals and the nylon bushings for electrical feed-throughs were cooled by maintaining a constant flow of water. The furnace was balanced by a cylindrical counterweight. During a solidification experiment, the furnace travelled up the fixed alumina tube containing the specimen, thereby forcing the solid-liquid interface to move upwards. This was achieved through a motor and reduction gear assembly coupled with the counterweight. Oxidation of the specimen could be prevented by flushing argon (Matheson) purified grade 99.99%) into the furnace working tube.

A comprehensive review of the directional solidification techniques and description of the other accessories used in the experimental set up is to be found in the original work²⁴.

4.2 Diffusion Experiment:

The experimental procedure followed in determining the diffusivity of Ni in δ -Fe is outlined below.

The first step consisted in the preparation of diffusion couples of pure Fe and Fe-2 wt% Ni alloy. For this, ingots of pure Fe and Fe-2 wt% Ni alloy (size 3" x 3/8" dia.) were cast in Edwards argon arc melting unit. A typical analysis of the materials used in the preparation of alloys is indicated in table 4.2.1. The ingots were then sealed into silica tubes under argon atmosphere and homogenisation annealed at 1000°C for 72 hours. Fe-2 wt% Ni alloy was chemically analysed for Ni.

The ingots were rolled into strips of thickness 3/32" and the strips were cut into samples of size 1/2" x 1/4" x 3/32". The rolled faces of the samples were successively hand ground on 220, 320, 400 and 600 grade emery papers, lubricated with water and polished on 6 and 1 micron diamond impregnated cloths lubricated with kerosene. The polished sides of the samples of pure Fe and Fe-2% Ni alloy were pressure welded at 900°C. Oxidation of the samples was prevented by passing hydrogen at a slow rate. The pressure weld provided an ideal interface for the diffusion of nickel.

The furnace described in section 4.1 was utilised to carry out the diffusion anneal. Temperature profile inside the furnace working tube was carefully measured after it was stabilised to within $\pm 2^\circ\text{C}$. The profile is shown in fig. 4.2.1. The diffusion couple which was held in a long sample tube and supported by a thin alumina tube, was steadily

introduced into the furnace working tube under a constant flow of argon. During this, care was taken that the sample did not reach the δ - γ transition temperature for Fe-2 wt% Ni alloy. This was assured by moving the furnace sufficiently upwards. The furnace working tube was sealed from the bottom. It was then evacuated and back filled with argon 2 to 3 times. The furnace was lowered so that the sample reached the desired reaction temperature. Diffusion anneal was carried out.

Following an air quench, the couple was prepared metallographically, (techniques as summarised earlier) and the concentration profile of nickel determined by electron probe microanalysis.

4.3 Solidification Experiments

4.3.1 Casting Experiments:

The composition of the materials used in the preparation of Fe-2% Ni binary and Fe-2% Ni-C ternary alloys has been listed in table 4.2.1.

About 40 grams of alloy materials were melted in Edwards argon arc melting unit and cast into ingots of 3" length and 3/8" dia. The binary and ternary alloy ingots were sectioned in a direction perpendicular to the length. The sectioned faces were metallographically prepared and etched (section 4.4) to reveal the segregation structure. Following the qualitative study of the binary and ternary segregation structures, a semi-quantitative experiment was performed. Instead of casting the samples in elongated ingot

shapes, they were cast into elliptical buttons of size $1\frac{1}{4}$ " dia. x $\frac{1}{2}$ " thickness. The samples were sectioned in a direction approximately parallel to the direction of cooling and were metallographically prepared. The casting in a water cooled copper mold provided extremely high cooling rate in all these experiments. The transverse section of these samples were taken at an equal distance from the top surface and micro-probe paths were marked on these, in a micro-hardness testing machine. Concentration profiles of Ni were determined along these paths.

In order to quantitatively co-relate the micro-segregation of Ni, with solidification parameters and to obtain a precise model for the study of homogenisation the apparatus described in section 4.1 was utilised. The experiments performed are summarised in the next section.

4.3.2 Controlled Solidification Experiments:

About 40 grams of alloy materials were melted and cast into ingots of size 3" length x $\frac{3}{8}$ " dia. in the argon arc melting unit. The ingots were swaged into rods of 0.17" dia. and were subsequently chemically analysed for Ni and C. The final analysis of the alloy samples is given in table 4.3.1. The furnace was first raised to its topmost position. The sample assembly was then slowly introduced into the furnace working tube under a flow of argon. The detailed sectional view of the sample assembly is as shown in fig. 4.3.2. After the complete introduction of sample, the bottom brass sealing cap was replaced and the bottom of the working tube was sealed.

The argon flow was stopped and the working tube was evacuated. It was back filled with argon several times before the final filling. The furnace was then lowered to its bottom-most position, causing the melting of the top 10 to 15 cms of the sample. The furnace was allowed to come to a thermal equilibrium. The solid-liquid interface was then moved at a preset rate by activating the furnace drive motor. After having directionally grown about 3 to 4 cms length of the specimen, the bottom sealing cap was loosened and the entire sample assembly was dropped into a metal tube filled with water. The experimental conditions, viz. G and R were maintained the same in both binary and ternary alloy solidification experiments.

4.4 Metallographic Preparation of Specimens

The directionally solidified portion of the specimen which was macroscopically visible, was sectioned and mounted in lucite after further sectioning with a diamond wheel. The specimens were rough ground on No. 80 emery belt and subsequently hard ground on Nos. 220, 320, 400 and 600 grade metallographic emery papers lubricated with water. Polishing was carried out on 6 and 1 micron diamond impregnated cloths lubricated with kerosene. The specimens were cleansed by swabbing with methyl alcohol and rinsed with distilled water. They were subsequently dried by pressurised dry air.

The segregation pattern in Fe-Ni binary alloy was revealed by etching a freshly polished specimen in a modified

Oberhoffer solution. The optimum etching time was found to be between 5 and 8 seconds. The appearance of a reddish-brown color on the specimen surface showed a good etching contrast.

The composition of the etching solution used is as follows:

$\text{FeCl}_3, 6\text{H}_2\text{O}$	(Ferric chloride)	30 g
$\text{CuCl}_2, 2\text{H}_2\text{O}$	(Cupric chloride)	8 g
$\text{SnCl}_2, 2\text{H}_2\text{O}$	(Stannous chloride)	4 g
HCl	(Hydrochloric acid S.g 1.1)	36 c.c.
H_2O	(Distilled water)	500 c.c.
$\text{C}_2\text{H}_5\text{OH}$	(Ethanol)	500 c.c.

Ternary alloy specimens showed good etching in a slightly modified solution. The cupric chloride was reduced from 8 grams to 4 grams and HCl was reduced from 36 c.c. to 25 c.c. in this modified form.

The mechanism of etching to reveal segregation patterns and the development of the etching reagent have been dealt with by Jin and Purdy³⁶.

4.5 Preparation of Probe Standards:

Since electron probe microanalysis was a main tool in determination of the concentration profiles of nickel both in the diffusion and microsegregation studies, it was decided to fabricate some probe standards. These standards served to obtain a calibration plot between the intensity ratio and nickel concentration, which consequently eliminated the necessity of applying complicating correction procedures for the analysis of microprobe data.

Forty gram ingots of pure Fe, Fe-1 wt% Ni, Fe-2 wt% Ni and Fe-3 wt% Ni were cast in the argon arc melting unit. They were swaged to a size of 1/8" dia. rod. Samples of 1" length were cut from these rods and were sealed into a quartz tube under argon. They were then homogenised for 3 days at 1200°C. The samples were chemically analysed several times. The results of the chemical analyses are given in table 4.4.1.

These samples were mounted in bakelite along with zirconium oxide, electron cage and a sample of pure Ni. The ZrO₂ served as a fluorescent screen to adjust the beam size and also in focussing it. The electron cage served to measure the electron beam current.

4.6 Electron Probe Micro-Analysis

Segregation profiles of Ni were obtained by sectioning the directionally solidified samples in a direction perpendicular to the direction of growth. The microprobe paths were marked in micro hardness machine. The etching layer was removed by polishing, before the probe analysis was carried out.

All the analyses were performed on an Acton Camera Microanalyser with an X-ray emergence angle of 18° at McMaster University. A detailed description of the components, operation procedure and specifications of this instrument is to be found in a special publication on this³⁷.

The operating voltage and the beam current used were 15 kV and 150 na respectively. For Ni segregation studies, analysis was carried out by point counting for 10 seconds in steps of 7 microns. For diffusion, a point counting step of 30 microns was used.

A calibration plot (as mentioned in section 4.5) between $\left(\frac{I}{I_0}\right)$ intensity ratio and Ni concentration was obtained for each analysis.

CHAPTER 5

RESULTS AND DISCUSSION

The results of the experiments summarised in chapter 4 are discussed in detail in this chapter. The discussion of results is classified into two principal parts viz. (a) diffusivity of Ni in δ -Fe and (b) solidification concerning mainly with the morphology of growth and micro-segregation and homogenisation of Ni.

Diffusion data have been analysed by fitting them to error function curves and the temperature dependence of diffusivity of Ni in δ -Fe has been determined by the Arrhenius analysis.

The discussion on the solidification experiments is further classified into two sections. The first section deals with results of casting experiments performed in the argon arc melting unit. Due to the inadequate knowledge of the solidification parameters, no definite quantitative conclusions could be drawn from these experiments.

The second section deals with controlled solidification experiments. The discussion is directed mainly towards the morphology of growth and microsegregation and homogenisation of Ni in Fe-2% Ni binary and Fe-2% Ni - X% C ternary alloys. The extent of homogenisation in binary alloys has been quantitatively and experimentally estimated. The effect of C on morphology of growth and microsegregation of Ni is also discussed.

5.1 Diffusivity of Ni in δ -Fe ($D_{Ni}^{\delta Fe}$)

The results of the Fe-Fe-2 wt% Ni diffusion couples reacted at 1473^o, 1484^o and 1494^oC have been shown in figs. 5.1.1, 5.1.2, and 5.1.3. The micro-probe data and the readings for nickel concentration penetration curves at reaction temperatures are reported in tables 5.1.1, 5.1.2 and 5.1.3. The figures 5.1.1, 5.1.2 and 5.1.3 show the observed concentration of nickel in δ -Fe as a function of the diffusion distance as measured from the initial Fe-Fe-2 wt% Ni weld interface. The chemical diffusion coefficient of Ni in δ -Fe was determined by fitting an error function curve to the equilibrium data. The error function curve is represented by the following equation:

$$\frac{C - C_o}{C_s - C_o} = \text{erfc} \left(\frac{x}{2\sqrt{Dt}} \right) \quad (5.1.1)$$

where, D = diffusivity in (cm^2/sec)

C = concentration at a distance x cms from the interface.

t = time of diffusion reaction (in seconds)

C_o = concentration at $t = 0$

C_s = Interface concentration

Using equation 5.1.1, values of $D_{Ni}^{\delta Fe}$ were determined on either side of the interface at each reaction temperature. Average value of $D_{Ni}^{\delta Fe}$ was evaluated. The results are as shown in table 5.1.4(a)

The temperature dependence of $D_{Ni}^{\delta Fe}$ was studied through the Arrhenius analysis. According to this, following equation describes the temperature dependence of diffusivity of Ni in δ -Fe.

$$D_{Ni}^{\delta Fe} = D_0 \exp \left(\frac{-\Delta H}{RT} \right) \quad (5.1.2)$$

where, D_0 = frequency factor (cm^2/sec)

ΔH = Activation energy for diffusion (cal/mole)

R = Universal gas constant (1.98 cal/ $^{\circ}K$ mole)

T = Reaction temperature ($^{\circ}K$)

Rewriting equation 5.1.2 as

$$\ln D = \ln D_0 - \frac{\Delta H}{RT} \quad (5.1.3)$$

$$\text{alternatively, } \log_{10} D = \log_{10} D_0 - \frac{\Delta H}{2.303 RT} \quad (5.1.4)$$

From equation 5.1.4 it is clear that a plot between $\log_{10} D$ and $\frac{1}{T}$ will be a straight line and the slope and intercept (on $\log_{10} D$ axis) of this plot will yield the values of the activation energy ΔH and the frequency factor D_0 respectively. Table 5.1.4(b) summarises the data obtained from Arrhenius analysis of $D_{Ni}^{\delta Fe}$ and fig. 5.1.4 indicates the temperature dependence.

Although a close straight line fit is obtained between the three experimental points, not much reliance can be put on the values of ΔH and D_0 obtained from this plot. However, it does provide a good value for $D_{Ni}^{\delta Fe}$, which is the essential requirement for this study.

From fig. 5.1.4, $D_{Ni}^{\delta Fe}$ is given by

$$D_{Ni}^{\delta Fe} = 11.2 \exp \left(\frac{-62,700}{RT} \right) \quad (5.1.5)$$

Extrapolation of the Arrhenius plot for $D_{Ni}^{\alpha-Fe}$ to δ -Fe range was tried utilising the data of Borg and Lai⁴⁶. This is shown in fig. 5.1.5. A remarkable fit is obtained between the three experimental points and the Arrhenius plot of Borg and Lai⁴⁶. The values of ΔH and D_0 obtained from fig. 5.1.4 are closely comparable to that of Borg and Lai⁴⁶.

Finally, fig. 5.1.6 summarises the Arrhenius plots for Ni diffusivities in different phases of Fe (α -Fe, γ -Fe δ -Fe and liquid). Following facts are significant from fig. 5.1.6.

(i) The values of activation energies for Ni diffusivity in α -Fe and δ -Fe are closely comparable.

(ii) The activation energy for Ni diffusion in γ -Fe is highest (consequently $D_{Ni}^{\gamma Fe}$ is small).

(iii) The Ni diffusivity is highest in the liquid.

The values for ΔH and D_0 for Ni diffusion in different phases of Fe are listed in table 5.1.5(b) and the data for figs. 5.1.5 and 5.1.6 have been given in table 5.1.5(a).

5.2 Solidification

5.2.1 Casting Studies:

The results of the casting studies performed on Fe-2 wt% Ni binary and Fe-2 wt% Ni-C ternary alloys in an argon arc melting unit have been summarised in figs. 5.2.1 to 5.2.4.

Figure 5.2.1 represents the microstructures of the cross sections of ingots (size 3" length x 3/8" dia.) of Fe-1.92 wt% Ni binary and Fe-2.04 wt% Ni - 0.207 wt% C ternary alloys. The overall structure of the binary alloy is represented in fig. 5.2.1(a). The direction of dendritic growth is approximately parallel to the direction of heat removal, except in the top portion, where free dendrites appear markedly. The orientation of these dendrites is random, and the dendritic character is more developed. The central region, where dendritic growth is not very clear, indicates the homogenised region. The horizontal curved lines appearing in the structure are probably because of the thermal fluctuations.

The structure of the ternary alloy, however, is predominantly dendritic in all parts of the section. As observed in the case of the binary alloy, randomly oriented free dendrites appear in the top portion and the structure is roughly directional in the rest of the sample. There is no apparent homogenisation effect in the case of ternary alloy. From these experimental observations, we can conclude a definite morphological change in structure because of the addition of carbon and a significant homogenisation effect in the case of binary alloy.

A similar study was carried out by solidifying these alloys (binary and ternary) in the form of elliptical buttons. The alloy buttons were sectioned vertically and metallographically prepared. The structures of the directionally solidified regions of these alloys appear in figs. 5.2.2(a) and (b).

The overall structures are indicated in figs. 5.2.2(c) and (d). In the directionally solidified region, the dendritic orientation in a particular grain is the same but it varies from grain to grain. A change in dendritic morphology as observed previously, is apparent in this case also. The effect of homogenisation is visible in the bottom portion of the structure in case of binary alloy (Fig. 5.2.2(c)).

The transverse sections of these alloys, perpendicular to the approximate direction of growth (at an equal distance from the top) were studied quantitatively by electron probe microanalysis. The aims of this study were as follows:

(i) To determine the degree of segregation of Ni in both the binary and ternary alloys.

(ii) To calculate the segregation index of Ni in both alloys ($S_I = \frac{C_{\max}}{C_{\min}}$).

(iii) To study the effect of carbon on the segregation of Ni.

The structures of the transverse sections in the case of binary and ternary alloys appear in figs. 5.2.3 and 5.2.4. The dendritic morphology is more clearly visible in these sections as compared to fig. 5.2.2. The centres of the dendrite cruciforms indicate the primary arms of the dendrites and the side branches growing from the main stem represent the secondary arms. As can be seen from the figs. 5.2.3 and 5.2.4 the secondary arms are more developed in the case of ternary. The contrast between the dendritic cross sections and the light inter-dendritic region is also more pronounced in the case of the ternary alloy as compared to the binary, indicating

probably a stronger segregation effect in the presence of carbon.

The electron microprobe paths and the corresponding results of the probe analysis have been shown in figs. 5.2.3 and 5.2.4 for Fe-1.92 wt% Ni binary and Fe-2.04 wt% Ni-0.32 wt% C ternary alloys. The plots indicate the Ni concentration profiles across the dendritic cross-sections. The microprobe data for these analyses are listed in table 5.2.1. From the concentration profiles, the values of C_M (maximum Ni concentration) and C_m (minimum Ni concentration) were estimated and S_I (segregation index of Ni $\frac{C_M}{C_m}$) was evaluated in the cases of binary and ternary alloys. The results are listed in table 5.2.2.

Both the amplitude of segregation ΔC i.e. the difference between maximum solute (Ni) concentration and minimum solute concentration and segregation index S_I are slightly higher in the case of ternary alloy as compared to the binary alloy. The segregation index is 1.407 for the binary alloy and 1.485 for the ternary. Hence it may be said that the difference in S_I values is perhaps not significant. The values of the minimum Ni concentration are higher than $K_0 C_0$ values for both the cases. In the case of the binary alloy, this appears to be due to the stronger homogenisation effect both during and after solidification. This, however, is dealt with in detail in the discussion of results on controlled solidification experiments.

These qualitative and semi-quantitative results seem to agree fairly well with those of the other investigators. Subramanian et al¹⁵ observed that the addition of carbon to

a binary Fe-base alloy increased the degree of branching of the dendrite. Flemings et al.³⁰ observed a much clearer dendritic growth in an Fe base binary alloy (Fe-26 wt% Ni) after the addition of carbon. Our results summarised in figs. 5.2.1 and 5.2.2 qualitatively agree with these observations.

Philibert et al.²⁶ observed a very small change in the segregation index of Ni after addition of carbon. The results obtained on the values of segregation indices of Ni in Fe-2 wt% Ni binary alloy and Fe-2 wt% Ni-0.320 wt%C ternary, are in accordance (table 5.2.2) with their observations. However, as discussed previously, their results did not take into account the interaction effects of other solutes (such as As) present in the system. Nevertheless, it should be emphasised at this stage, that the inadequate knowledge of the solidification parameters (viz. G and R) in the case of these results does not permit us to draw any definite conclusions regarding the effect of carbon on the degree of segregation of Ni.

5.2.2 Controlled Solidification Studies

These experiments were taken up essentially to improve upon the results summarised in section 5.2.1. The experimental conditions in this case permitted a fairly adequate and precise estimation of the solidification parameters, viz. thermal gradient G and rate of S-L interface advance R . The method of estimation of G has been indicated in fig. 4.3.1. The value of R could be evaluated from the motor-reduction gear assembly used for the furnace travel. The

principal aim of these experiments was to study the effect of carbon on important aspects of solute distribution after solidification such as the morphology of growth, micro-segregation of Ni and extent of homogenisation of Ni. For this, the controlled solidification of Fe-2 wt% Ni and Fe-2 wt% Ni - X wt%C alloys was carried out. The values of G , R and C_0 (initial average Ni concentration) were kept constant for both alloys. These carefully controlled conditions permitted a more precise study of the effect of carbon on the aspects described above.

As mentioned earlier in this section, the discussion is classified into three parts: morphology, microsegregation and homogenisation.

Morphology of Growth

The compositions of the specimens selected for the study of morphology of growth are as follows:

No.	Composition
1 (binary)	Fe-2.06 wt% Ni
2 (ternary)	Fe-1.98 wt% Ni - 0.48 wt% C
3 (ternary)	Fe-2.01 wt% Ni - 0.58 wt% C
4 (ternary)	Fe-2.02 wt% Ni - 0.40 wt% C
5 (binary)	Fe-2.90 wt% Ni

Table 5.2.3 summarises the solidification conditions (G and R) for these specimens. The possible sources of error involved in estimating these parameters appear to be:

- (i) the fluctuations in temperature during the solidification experiment,
- and (ii) change in the speed of drive motor.

In a typical solidification experiment the temperature fluctuation was estimated to be within 2°C (Hone²⁴). The error involved in evaluating the value of R was found to be ± 0.1 cm/hr. The temperature fluctuation resulting from this error is also within 2°C . Hence the extent of errors resulting from these sources is insignificantly small. The experiments were carried out under steady state. The absence of convection in the controlled solidification experiments has already been demonstrated by Hone²⁴ through a liquid diffusion couple experiment.

The solidification structures of the specimens 1 to 5 parallel to the macroscopic growth direction have been presented in figs. 5.2.5, 5.2.6 and 5.2.7. From the photomicrographs of these specimens, it is concluded that the growth morphology is cellular dendritic in nature. The dendritic structure in binary alloys (figs. 5.2.5(a) and 5.2.7) appears plate-like whereas the structure in ternary alloys (figs. 5.2.5(b) and 5.2.6(a), (b)), due to the presence of well developed secondary arms, appears more rod-like. In plate-like structures, the spaces between the secondary arms fill in at an early stage of solidification, whereas those in rodlike structures, fill in at a later stage. As a result, considerable amount of solute build-up takes place between the secondary arms in rodlike structures. Kattamis and Flemings³¹ have described the columnar dendritic morphology in AISI 4340 steel (composition as given in section 2.5) as intermediate between perfect rodlike and sheetlike morphologies. Out of the morphologies described

in figs. 5.2.5 to 5.2.7 only the morphology in fig. 5.2.5 (b) somewhat resembles the one discussed by them. The growth morphology in fig. 5.2.6 (b) is predominantly dendritic and can be classified more as rodlike.

The transverse sections of specimens 1 to 4 have been presented in figs. 5.2.8 to 5.2.11. The top transverse section is closer to the final position of solid-liquid interface. The primary arms, which are clearly visible in the parallel section, form the central portions of the cruciform structure seen in figs. 5.2.8 to 5.2.11. The secondary arms that grow from the main stem are more clearly visible in these sections. In fig. 5.2.10(a) tertiary arms can be seen to have grown from well developed secondary arms. The structure in the binary alloy (fig. 5.2.8) especially in the bottom section, appears to be of an open type. This has been dealt with in a greater detail by Hone²⁴, who represented the open structure as follows:

```

+   +   +
+   +   +
+   +   +

```

From the study of figs. 5.2.5 to 5.2.7, it is evident that the dendritic character is more developed in the case of ternary alloys as compared to binary.

A tie-line section for Fe-2.01 wt% Ni - 0.58 wt% C ternary alloy has been superimposed on Fe-Ni binary phase diagram as indicated in fig. 3.1.1. It can be seen that the addition of carbon to Fe-2 wt% Ni binary alloy,

- (i) increases the slope of liquidus,
- and (ii) increases the temperature range of solidification

(i.e. the difference between liquidus and solidus).

The higher liquidus slope increases the amount of constitutional supercooling in front of the solid-liquid interface, in the case of ternary and hence favours dendritic growth (Weinburg and Buhr²⁸). As discussed earlier in this section, the structure of the directionally solidified specimens under a positive thermal gradient in liquid is cellular dendritic. The added increase in the amount of constitutional supercooling for ternary alloy should act to make it predominantly dendritic in nature.

The increased temperature range of solidification for ternary increases the extent of liquid-solid region, which eventually increases the local solidification time and hence results in a slower rate of thickening of primary arms. This presumably favours a stronger development of secondary and tertiary arms and hence a more strongly dendritic character for the ternary. This, along with the experimental conditions for binary and ternary, has been schematically illustrated in fig. 3.1.1

Microsegregation:

To obtain definite quantitative results on Ni redistribution, electron probe microanalysis of directionally solidified specimens was carried out. Transverse sections were chosen for this study, essentially because the electron microprobe paths could be more precisely marked. Again, as reviewed in section 2.4, maximum segregation occurs across the primary dendritic cross sections, which are clearly visible in transverse sections.

The main aims of the segregation study were to obtain the degree of segregation of Ni both in the binary and ternary alloys and to study the effect of carbon on this.

The electron microprobe paths were marked in a microhardness testing machine and following precautions were taken in selecting a microprobe path.

(i) The transverse section should be such that the dendrite cross sections (cruciform structures) are exactly perpendicular to the macroscopic direction of growth.

(ii) The microprobe paths chosen for comparative study, should incorporate the dendrites of an essentially similar morphology.

(iii) The wavelengths of the segregation profiles selected for comparison should be nearly the same.

It was decided to carry out the electron microprobe analyses only on specimens 1 and 3 (Fe-2.06 wt% Ni binary and Fe-2.01 wt% Ni-0.58 wt% C respectively). In specimen 2, no adequate probe path could be chosen and the growth in specimen 4 was very much inclined to the vertical so that an exact transverse section could not be obtained. The geometry chosen for microprobe paths was of $|X|$ type because maximum segregation occurs along this path (Hone²⁴).

The results of electron microprobe analysis conducted on specimens 1 and 3 have been presented in figs. 5.2.12 to 5.2.16, along with microprobe paths marked on the dendritic structures. From the figs. it is clear that the Ni segregation profiles are periodic in nature, with the concentration maximum appearing at the centre of interdendritic region and

the minimum at the centre of the primary dendrite arm. The experimental data on microprobe analyses are listed in tables 5.2.4 and 5.2.5. Values of the maximum and minimum solute concentrations in both binary and ternary appear in tables 5.2.6 and 5.2.7. These values were estimated by approximating the electron microprobe data points, by an average line profile drawn through them.

The segregation indices of Ni could be evaluated from the values of C_{\max} and C_{\min} in both binary and ternary alloys. For the comparison of segregation indices of Ni the electron microprobe data of figs. 5.2.12(b) and fig. 5.2.14 were used. The results have been summarised in tables 5.2.6 5.2.7 and 5.2.9. The segregation indices of Ni in binary and ternary alloys are 1.59 and 1.55 respectively. The change in S_I , due to addition of carbon is quite small. However, it is necessary at this stage, to discuss the validity of using the segregation index as a parameter to describe the degree of segregation of solute.

Segregation index has been used extensively in literature to characterise microsegregation. It is however a rather incomplete measure of the degree of segregation. It takes into account only two points on the solute distribution profile. It is thus conceivable for two entirely different segregation patterns to yield the same segregation ratio. In addition to this the position of maximum solute concentration cannot be determined exactly, since it is very much dependent upon the geometry of the growth, whereas the position

and value of the minimum solute concentration can be more precisely determined and should be formed on a basis for describing the degree of segregation of solute.

Before considering this aspect, it is essential to review the basis on which the binary phase diagrams (Fe-Ni and Fe-C) were determined. The binary phase diagrams given in figs. 3.1.1 and 3.1.2 are based on the data on respective (Fe-Ni and Fe-C) peritectic reactions and melting temperature of γ -Fe. The value for the melting temperature of γ -Fe was taken from Hone²⁴ as 1529.5°C . The peritectic reactions in Fe-Ni binary and Fe-C binary have already appeared in chapter 3. Based on these diagrams, the values of equilibrium distribution coefficients of Ni in δ -Fe and γ -Fe and that of carbon in γ -Fe were calculated. The values of K_0 for Ni in δ -Fe and γ -Fe are 0.545 and 0.67 respectively. The value of K_0 for C in γ -Fe is 0.315. The solute interaction in dilute Fe-Ni-C ternary alloy was assumed to be negligible ($\epsilon_{\text{Ni-C}} = \epsilon_{\text{C-Ni}} = +2.9$). The binary distribution coefficients for both Ni and C served as very good approximations to the ternary distribution coefficients (Hone et al.⁴⁸).

As mentioned earlier, a 'tie line section' of ternary alloy was constructed from the segregation paths on liquidus and solidus surfaces of ternary (fig. 3.2.3). The points A and B in fig. 3.2.3 form the end points of a tie line in ternary. This can be approximately shown on the Fe-Ni binary diagram (f.g. 3.1.1). The tie line section is superimposed on the binary diagram in fig. 3.1.1. The composition of the first solid to form from liquid of comp. C_0 is given by $K_0 C_0$; this

has been shown on Fe-Ni binary and on the tie line section. The value of C_{\min} i.e. the final dendritic tip concentration has also been plotted. The tip undercooling in the case of binary and ternary can be closely estimated from these plots. It is clearly seen that the tip undercooling is much larger in the case of ternary (16°C) as compared to that for binary (3°C). A larger tip undercooling indicates a more flat dendrite tip and a larger solute build up in front of the solid-liquid interface. In the absence of Gibbs Thomson effect and kinetic effect, a higher value of tip undercooling eventually implies a higher value of solute concentration at the tip (i.e. C_{\min}). As can be seen from the results of electron probe microanalysis conducted on binary and ternary alloys, the C_{\min} value in the case of Fe-2.06 wt% Ni binary (1.6 wt% Ni) is smaller than that in Fe-2.01 wt% Ni - 0.58 wt% C ternary alloy (1.8 wt% Ni).

From fig. 3.1.1 the fractional undercoolings for binary and ternary alloys could be estimated, by comparing the actual tip undercooling to the maximum possible undercooling in each case. It is seen that, in ternary alloy the fractional undercooling (~ 0.7) is higher than that in the binary (0.5). A higher fractional undercooling implies a reduction in the degree of segregation of solute. Thus a higher tip concentration coupled with the higher fractional supercooling for ternary appear to reduce the degree of segregation of Ni in it.

The addition of carbon to the binary Fe-2% Ni alloy changes the mode of crystallization from δ -Fe to γ -Fe. The higher value of Ni distribution coefficient in γ -Fe (0.67 for γ -Fe, 0.545 for δ -Fe) tends to attenuate the degree of segregation by reducing the difference between the interface solute concentrations in liquid and solid.

A positive thermodynamic interaction parameter between nickel and carbon further tends to attenuate the degree of segregation of Ni, but, however, the contribution of this appears to be negligibly small because of the small value (+2.9) of the interaction parameter (Hone²⁴).

It may finally be said that, the addition of carbon to a binary Fe-2% Ni alloy tends to reduce the degree of segregation of Ni in it, for the conditions of freezing employed in this work.

Homogenisation

As reviewed in section 2.6, the homogenisation of a solute is a necessary consequence of the concentration gradients created by solute redistribution during solidification. The total homogenisation effect may be classified into two parts viz.

- (i) Homogenisation during solidification
- (ii) Homogenisation after solidification.

The results obtained on the electron probe analyses of transverse sections of the directionally solidified alloys indicate that the dendritic tip concentration (C_{\min}) is much higher than the value K_0C_0 ; the composition of the first

solid to form from a liquid of initial composition C_0 . This has been shown in figs. 5.2.12 to 5.2.15 for binary and ternary alloys.

Fig. 5.2.16 compares the experimentally obtained Ni distribution (fig. 5.2.12(a)) with the Scheil-Chipman plot (eq. 3.2.1) for Fe-2.06 wt% Ni alloy. It is quite clear from fig. 5.2.16 that the assumption of negligible back diffusion during solidification is incorrect for this alloy.

Brody and Flemings²¹ have modified the Scheil Chipman mass balance approach by estimating the amount of back diffusion during solidification. For this, they defined a dimensionless homogenisation parameter α_s as;

$$\alpha_s = \frac{D_s t_f}{L^2} \quad (5.2.1)$$

where,

D_s = solute diffusivity in solid phase

t_f = local solidification time

(defined by Brody and Flemings²¹ as time at a given location in a casting or ingot between initiation and completion (or near completion) of solidification)

L = half dendrite arm spacing.

For a large amount of back diffusion:

$$\alpha_s \gg 1 \quad (5.2.2)$$

and, for the negligible back diffusion;

$$\alpha_s \ll 1 \quad (5.2.3)$$

The parameter α_s was estimated for the Fe-2.06 wt% Ni binary alloy; from the experimental data, which are listed below.

$$D_{Ni} = 1.60 \times 10^{-7} \text{ cm}^2/\text{sec} \text{ (Average value over the } \delta\text{-Fe temperature range)}$$

$$L = 280 \times 10^{-4} \text{ cms}$$

$t_f \approx 65$ seconds (estimated from the knowledge of the speed of interface advance and approximate position of the transverse section with respect to the final solid-liquid interface).

Hence,

$$\begin{aligned} (\alpha_s)_{\text{Fe-2.06\%Ni binary}} &= \frac{1.6 \times 10^{-7} \times 65}{(280 \times 10^{-4})^2} \\ &= 0.01326 \quad (5.2.4) \end{aligned}$$

The extremely small value of α_s obtained for the binary alloy, implies a very small amount of back diffusion; which is not consistent with the experimental results. This calls for a closer inspection of the approach used by Brody and Flemings²¹. The parameter t_f used by them is rather loosely defined and a precise estimation of it is quite difficult. Moreover, Brody and Flemings³¹ have used an undefined correction factor of 0.32 to the experimentally observed dendrite arm spacings. Hence, the value of α_s seems to be a rather misleading estimate of the solute homogenisation during solidification. Nevertheless, since it is very difficult to obtain experimentally the solute distribution prior to completion or near completion of solidification, the extent of solute back diffusion during solidification can only be theoretically estimated.

The same model may be applied to estimate the homogenisation during freezing for the ternary alloy for which the data are as follows:

$$D_s = 3.41 \times 10^{-9} \text{ (from Jin and Purdy}^{35}\text{)}$$

$$L = 263 \times 10^{-4} \text{ cms}$$

$t_f = 130$ seconds (from fig. 3.1.1 the estimated local solidification time is approximately two times that in the binary),

$$\begin{aligned} \text{hence, } (\alpha_s)_{\text{ternary}} &= \frac{3.41 \times 10^{-9} \times 130}{(263 \times 10^{-4})^2} \\ &= \frac{3.41 \times 130}{(2.63)^2} \times 10^{-5} \\ &= 6.42 \times 10^{-4} \end{aligned} \quad (5.2.5)$$

From this, it is evident that the homogenisation during freezing for ternary is insignificantly small, in spite of a higher value of local solidification time.

Homogenisation of solute after solidification, however, can be experimentally and quantitatively studied. This is governed solely by the solid state diffusion of the solute, the value of which in itself, is dependent upon the crystalline state of the solid formed from the liquid. As stated in the introduction, the Fe-2% Ni binary alloy undergoes a L- δ transformation and Fe-2% Ni-C alloy undergoes a L- γ transformation. From fig. 5.1.6, it is seen that the diffusivity of Ni in δ -Fe ($\sim 10^{-7}$ cm²/sec) is approximately two orders of magnitude higher than that in γ -Fe ($\sim 10^{-9}$ cm²/sec) at L-S transformation temperatures. Hence, a much larger post solidification homogenisation should take place in binary as compared to the ternary alloy.

This can be seen qualitatively from a study of figs. 5.2.8 to 5.2. 11. Here the transverse sections of the binary (fig. 5.2.8) and ternary (figs. 5.2.9, 5.2.10, 5.2.11) alloys indicate that the dendritic character diminishes much faster in the binary than in the case of ternary. This means that the solute concentration gradients are leveled out at a much faster rate in the binary alloy.

The decay of the solute segregation profile is quantitatively described by the parameter called "index of residual segregation" which is defined as follows (Section 2.6).

$$\delta_i = \frac{\text{Final Amplitude of Segregation}}{\text{Initial Amplitude of Segregation}} \quad (5.2.6)$$

The larger the value of this parameter, the smaller is the extent of homogenisation after solidification.

From the Ni concentration profiles presented in figs. 5.2.12 to 5.2.15, this parameter was evaluated for Fe-2.06 wt% Ni binary and Fe-2.01 wt% Ni - 0.58 wt% C ternary alloys. The values of δ_i for binary and ternary alloys are 0.473 and 0.88 respectively. This suggests that only a minimal homogenisation takes place in the ternary as compared to the binary alloy. Indeed, this is to be expected from the fact that the addition of carbon changes the mode of crystallization from δ -Fe to γ -Fe for the ternary alloy. Although no quantitative results are available, the Fe-2.90 wt% Ni alloy (fig. 5.2.7) indicates a strong post solidification solute homogenisation effect, in spite of a much smaller δ -Fe temperature range as compared to that of Fe-2 wt% Ni binary alloy.

As reviewed in section 2.6, the decay of an arbitrary solute distribution function $f(r')$ possessing cylindrical symmetry is described by the following equation:

$$c(r,t) = \frac{2}{a^2} \left\{ \int_0^a r' f(r') dr' + \sum_{n=1}^{\infty} e^{-\tilde{D}\alpha_n^2 t} \frac{J_0(r\alpha_n)}{J_0^2(a\alpha_n)} \right. \\ \left. \times \int_0^a r' f(r') J_0(\alpha_n r) dr' \right\} \quad (5.2.7)$$

where,

\tilde{D} = solute diffusivity in the solid

$f(r')$ = Initial solute distribution function

a = half wavelength of the segregation wave

and α_n = roots of $J_1(\alpha_n) = 0$

The equation 5.2.6. is valid only for an idealised cylindrical growth morphology which seems to be a reasonable approximation for the Fe-2.06 wt% Ni alloy (fig. 5.2.5(a)). The values of D and a were obtained from experimental results and $f(r')$ was evaluated by fitting a polynomial to the experimental points in fig. 5.2.12(a). The values of the parameters used for this computation are as follows:

$$D_{Ni}^{\delta-Fe} = 1.6 \times 10^{-7} \text{ cm}^2/\text{sec} \quad \text{fig. (5.1.4)}$$

$t = 130.11$ seconds (estimated from distance between the
transverse sections and R)

$$a = 280 \times 10^{-4} \text{ cms}$$

and $f(r') = 1.60399 - 7.09r + 2967.2r^2 - 16053.16r^3 + 4273793.27r^4$.

The theoretically computed decay of Ni segregation profile due to solid state homogenisation has been compared with the experimental points (fig. 5.2.13) in fig. 5.2.17. A reasonably close fit is obtained, indicating thereby that homogenisation after solidification is essentially governed by the solid state diffusion of the solute. A theoretical computation of the initial segregation profile was obtained with increasing times and the results are shown in fig.

5.2.18. From the figure, it appears that after about 1 hour, the binary Fe-2.06 wt% Ni alloy completely homogenises.

Thus, for the Fe-2.06 wt% Ni binary alloy, the extent of homogenisation after solidification appears to be a major part of the total homogenisation effect. The extent of homogenisation during solidification is small in comparison, probably because of a very small value of local solidification time and because of the small concentration gradients formed in the solid immediately behind the dendrite tips, in spite of the high Ni diffusivity in solid state (δ -Fe).

The homogenisation during freezing for ternary is insignificantly small even though the value of local solidification time is higher in this case as compared to the binary. The homogenisation after solidification for ternary is minimal as it is expected from a much lower value of Ni diffusivity in γ -Fe, which is the mode of crystallisation for ternary.

As pointed out earlier in this chapter, the homogenisation parameter α_s provided only a misleading estimate of the back diffusion during solidification of the solute.

An attempt was made to apply the eq. 5.2.7 to estimate the homogenisation during solidification. Fig. 5.2.19 indicates the results obtained. An initial Ni distribution (prior to solidification) was assumed and its decay for the local solidification time was studied. The theoretically computed final profile and experimental results agree very well, indicating thereby that back diffusion during solidification is closely controlled by diffusivity of the solute in solid state.

CHAPTER 6

CONCLUSIONS

(i) The diffusivity of Ni in δ -Fe, determined experimentally in this work is described by the equation

$$D_{\text{Ni}}^{\delta\text{-Fe}} = 11.2 \exp. \left(\frac{-62,700}{RT} \right) \quad (6.1)$$

(ii) The addition of carbon to Fe-2% Ni binary alloy increases the temperature range of solidification and changes the nature of morphology of growth to strongly dendritic.

(iii) There is no significant change in the value of the segregation index of Ni, both in casting studies and controlled solidification experiments, because of the addition of carbon to the Fe-2% Ni binary alloy. The addition of carbon to binary, however, results in a higher tip concentration and a larger fractional undercooling for ternary.

(iv) For the binary Fe-2.06 wt% Ni alloy, the extent of homogenisation during solidification appears to be smaller as compared to the post solidification homogenisation, for the conditions of freezing employed in this work.

(v) For the Fe-Ni-C ternary alloy, homogenisation during freezing is negligible and post solidification homogenisation appears to be minimal, as observed in this investigation.

REFERENCES

1. G. S. Cole, Can. Met. Quart. 8, 189 (1969)
2. H. Biloni and B. Chalmers cited in "Principles of Solidification" by B. Chalmers; John Wiley and Sons, New York, (1964)
3. W. A. Tiller, K. A. Jackson, J. W. Rutter and B. Chalmers, Acta Met. 1, 428 (1953)
4. V. G. Smith, W. A. Tiller and J. W. Rutter, Can. J. Phys. 33, 723 (1955)
5. J. W. Rutter and B. Chalmers, Can. J. Phys. 31, 15 (1953)
6. D. E. Coates, S. V. Subramanian and G. R. Purdy, Trans. Met. Soc. AIME 242, 800 (1968)
7. J. W. Rutter in "Liquid Metals and Solidification" American Society for Metals, Cleveland, 250 (1958)
8. B. Chalmers and W. C. Wineguard, Trans. ASM 46, 1214 (1954)
9. W. Morris, W. A. Tiller, J. W. Rutter and W. C. Wineguard, Trans. ASM 47, 463 (1955)
10. W. A. Tiller and J. W. Rutter, Can. J. Phys. 34, 96 (1956)
11. W. A. Tiller, J. Iron Steel Inst. 192, 338 (1959)
12. E. L. Holmes, J. W. Rutter and W. C. Wineguard, Can. J. Phys. 35, 1223 (1957)
13. J. O. Coulthard and R. Elliot in "The Solidification of Metals" ISI Publication 110, London 61 (1967)

14. G. J. Davies *ibid* 66 (1967).
15. S. V. Subramanian, G. W. Howarth and D. H. Kirkwood
J. Iron Steel Inst. 206, 1027 (1968) and 206, 1124
(1968)
16. H. Biloni in "The Solidification of Metals" ISI
publication 110 London, 74 (1967)
17. E. Scheil, *Z. Metallkunde* 23, 70 (1942)
18. G. H. Gulliver, Metallurgical Alloys, Chas. Griffin,
London (1922)
19. J. Chipman and A. Hayes, *Trans. AIME* 135, 85 (1939)
20. W. G. Pfann, *Trans. AIME* 194, 747 (1952)
21. H. D. Brody and M. C. Flemings, *Trans. Met. Soc. AIME*
236, 615 (1966)
22. D. H. Kirkwood and D. J. Evans in "The Solidification
of Metals" ISI Publication 110 London 108 (1967)
23. J. B. Murphy, *Acta Metallurgica* 9, 563 (1961)
24. M. R. Hone, Ph.D. Thesis, McMaster University,
October, 1970
25. C. deBeaulieu and A. Kohn, *C. R. Acad. Sci. France*
246, 3615 (1958)
26. T. S. Philibert, E. Weinryb and M. Ancey, *Metallurgica*
72, 203 (1965)
27. R. D. Doherty and D. A. Melford, *J. Iron Steel Inst.*
208, 482 (1970)
28. F. Weinburg and R. K. Buhr in "The Solidification of
Metals", ISI Publication 110, London 295 (1967)
29. E. T. Turkdogan and R. A. Grange, *J. Iron Steel Inst.*
208, 482 (1970)

30. M. C. Flemings, D. R. Poirier, R. V. Barone and H. D. Brody, J. Iron Steel Inst. 208, 371 (1970)
31. T. Z. Kattamis and M. C. Flemings, Trans. Met. Soc. AIME 233, 992 (1965)
32. F. Weinburg and R. K. Buhr, J. Iron Steel Inst., 204, 16 (1966)
33. J. D. Lavender and F. W. Jones, J. Iron Steel Inst. 163, 14 (1949)
34. R. G. Ward, J. Iron Steel Inst. 203, 930 (1965)
35. G. R. Purdy and J. S. Kirkaldy, Met. Trans. AIME 2, 371, (1971)
36. I. Jin, G. R. Purdy "Research Note on Metallographic Reagents for Microsegregation", McMaster University Feb. 1971
37. "The Electron Probe Microanalyser" edited by A. Dalvi, McMaster University, December 1969.
38. M. Hansen "Constitution of Binary Alloys" 2nd ed. McGraw Hill, New York (1958)
39. A. Halawell and Hume Rothery, W. Phil. Trans. Royal Soc. London A 249, 417 (1957)
40. J. S. Kirkaldy, "Aspects of Modern Ferrous Metallurgy" University of Toronto Press, Toronto, p. 263 (1963)
41. J. S. Marsh, "Alloys of Iron and Nickel" 57, McGraw Hill Book Company (1938)
42. T. Kase, Sci. Rep. Sendai, 1925 (1) 14, 173
43. J. H. Andrews and G. T. C. Bottomelly in ISI Spec. Pub. 23, 5, (1938)

44. R. A. Buckley and W. Hume Rothery, *Journal of Iron and Steel Inst.* 202, 895 (1964)
45. M. Hone, S. V. Subramanian and G. R. Purdy, Unpublished research, McMaster University, Hamilton, Ontario, Canada.
46. R. J. Borg and D.Y. G. Lai, *Acta Metallurgica* Vol. 11, p. 861 (1963)
47. K. Hirano, M. Cohen and B. L. Averbach, *Acta Metallurgica* vol. 9, p. 440 (1961)
48. M. R. Hone, S. V. Subramanian and G. R. Purdy, *Can. Met. Quart.* 8, no. 3 (1969)

Table 3.2.1 Scheil Chipman Plot for Ni in Fe-2.06 wt% Ni

binary alloy

$$C_S^* = K_O C_O (1-g)^{K_O-1}$$

$$K_O = 0.545$$

$$C_O = 2.06$$

No.	g	$(1-g)^{K_O-1}$	C_S^* wt%	C_L^* wt%
1	0.0	1	1.12	2.06
2	0.1	1.05	1.18	2.18
3	0.2	1.10	1.24	2.28
4	0.3	1.17	1.32	2.42
5	0.4	1.26	1.41	2.59
6	0.5	1.37	1.53	2.82
7.	0.6	1.51	1.70	3.12
8	0.7	1.73	1.94	3.56
9	0.8	2.08	2.33	4.28
10	0.9	2.85	3.20	5.87
11	1.0	∞	∞	∞

Table 3.2.2 Scheil Chipman Plot for Ni in Fe-2.01 wt% Ni-

0.58 wt% C alloy

$$C_{S_1}^* = K_{O_1} C_{O_1} (1-g)^{K_{O_1}^{-1}}$$

$$K_{O_1} = 0.67$$

$$C_{O_1} = 2.01$$

No.	g	$(1-g)^{K_{O_1}^{-1}}$	$C_{S_1}^*$ wt%	$C_{L_1}^*$ wt%	$C_{S_1}^*$ At%	$C_{L_1}^*$ At%
1	0.0	1.00	1.34	2.01	1.271	1.89
2	0.1	1.03	1.39	2.08	1.31	1.96
3	0.2	1.07	1.45	2.16	1.36	2.04
4	0.3	1.12	1.51	2.26	1.43	2.13
5	0.4	1.18	1.59	2.38	1.50	2.24
6	0.5	1.25	1.69	2.52	1.59	2.37
7	0.6	1.35	1.82	2.72	1.71	2.55
8	0.7	1.48	2.00	2.99	1.88	2.81
9	0.8	1.70	2.28	3.41	2.14	3.20
10	0.9	2.14	2.88	4.29	2.69	4.02
11	1.0	∞	∞	∞	∞	∞

Table 3.2.3 Scheil Chipman Plot for C in Fe-2.01 wt% Ni
-0.58 wt% C ternary alloy

$$C_{S_2}^* = K_{O_2} C_{O_2} / (1-g + K_{O_2} g)$$

$$K_{O_2} = 0.315$$

$$C_{O_2} = 0.58$$

No	g	(1-g + K _{O₂} g)	C _{S₂} [*] (wt%)	C _{L₂} [*] (wt%)	C _{S₂} [*] (At%)	C _{L₂} [*] (At%)
1	0.0	1.00	0.18	0.58	0.84	2.67
2	0.1	0.93	0.19	0.62	0.91	2.88
3	0.2	0.86	0.21	0.67	0.97	3.09
4	0.3	0.79	0.23	0.73	1.06	3.39
5	0.4	0.72	0.25	0.79	1.16	3.69
6	0.5	0.65	0.27	0.88	1.28	4.07
7	0.6	0.58	0.31	0.98	1.42	4.52
8	0.7	0.52	0.35	1.11	1.61	5.13
9	0.8	0.45	0.40	1.28	1.85	5.89
10	0.9	0.38	0.47	1.51	2.18	6.94
11	1.0	0.31	0.58	1.84	-	-

Table 4.2.1 Chemical Analysis of the Materials used in
the Preparation of Alloy Specimens

Material	Impurities	Wt%
Derby Iron	C	0.0050
	Mn	0.0028
	S	0.0030
	P	0.0010
	Si	0.0040
	Cu	0.0054
	Ni	0.0040
	Cr	0.0020
	Al	<0.0010
Electrolytic Nickel	C	0.0053
	Co	0.0046
	Cu	0.0009
	Fe	0.0006
	Pb	0.0010
	O ₂	0.0086
Graphite	EVC (Union Carbide)	

Table 4.3.1 Analysis of the alloys used for directional solidification studies (for micro probe studies)

No	Alloy	Wt% Ni	Wt% C	Wt% Fe
1	Binary Fe-Ni	2.06	-	Bal.
2	Ternary Fe-Ni-C	2.01	0.58	Bal.

Table 4.4.1 Chemical Analysis of Probe Standards

No.	Proposed Composition	Wt of Fe added (g)	Wt of Ni added (g)	Wt% Ni estimated (calc.)	Wt% Ni analysed chemically
1	Fe-1% Ni	39.6218	0.3970	0.99	(i) 1.035 (ii) 1.034 (iii) 0.966
2	Fe-2 Ni	39.2048	0.7940	1.99	(i) 2.0556 (ii) 2.0180 (iii) 2.0320
3	Fe-3 Ni	38.8290	1.2093	3.02	(i) 3.2553 (ii) 3.0440 (iii) 3.0391

Table 5.1.1(a) Electron Microprobe data on Fe-Fe-2% Ni
diffusion couple reacted at 1473°C for 1800 seconds

Initial	Serial No.	wt% Ni	I (cps)	background (cps)	Final I (cps)	$\frac{I}{I_0}$
	1	100	7013	36	6977	1.0
	2	1	96	36	60	0.0086
	3	2	157	36	121	0.0173
	4	3	218	36	182	0.0261

Final	Serial No.	wt% Ni	I (cps)	background (cps)	Final I (cps)	$\frac{I}{I_0}$
	1	100	6331	27	6304	1.0
	2	1	85	27	58	0.0092
	3	2	150	27	123	0.0195
	4	3	207	27	180	0.0285

Table 5.1.1 (b) Concentration Penetration curve of Ni at 1473°C

Dist. from Interface (μm)	wt% Ni	Dist. from Int. (μm)	wt% Ni	Dist. from Int. (μm)	wt% Ni	Dist. from Int. (μm)	wt% Ni
-480	0.05	-180	0.55	120	1.48	420	1.97
-450	0.07	-150	0.56	150	1.47	458	1.98
-420	0.03	-120	0.57	180	1.55		
-390	0.09	- 90	0.69	210	1.67		
-360	0.09	- 60	0.80	240	1.68		
-330	0.32	- 30	1.0	270	1.71		
-300	0.10	0(Int.)	0.98	300	1.72		
-270	0.38	30	1.06	330	1.80		
-240	0.20	60	1.35	360	1.94		
-210	0.32	90	1.47	390	1.96		

Table 5.1.2(a) Electron Microprobe Data on Fe-Fe-2% Ni
Diffusion couple reacted at 1484°C for 1500 seconds

Initial	Serial No.	wt% Ni	I (cps)	background (cps)	Final I (cps)	$\frac{I}{I_0}$
	1	100	19110	85	19025	1.00
	2	1	253	85	168	0.00883
	3	2	448	85	363	0.01900
	4	3	615	85	530	0.02780

Final	Serial No.	wt% Ni	I (cps)	background (cps)	Final I (cps)	$\frac{I}{I_0}$
	1	100	20483	88	20395	1.0000
	2	1	277	88	189	0.0093
	3	2	491	88	403	0.01970
	4	3	685	88	597	0.0292

Table 5.1.2(b) Concentration Penetration Curve of Ni at 1484°C

Distance from Int. (μm)	wt% Ni	Dist. from Int. (μm)	wt% Ni	Dist. from Int. (μm)	wt% Ni	Dist. from Int. (μm)	wt% Ni
-520	0.00	-210	0.36	90	1.28	390	1.86
-480	0.01	-180	0.41	120	1.27	420	1.92
-450	0.02	-150	0.46	150	1.48	450	1.87
-420	0.035	-120	0.58	180	1.54	480	1.88
-390	0.050	- 90	0.59	210	1.58	510	1.89
-360	0.06	- 60	0.61	240	1.65	540	1.91
-330	0.09	- 30	0.90	270	1.73	570	1.92
-300	0.17	- 10	1.020	300	1.78	600	1.92
		0 (Int.)	0.98				
-270	0.16	30	1.06	330	1.83		
-240	0.19	60	1.16	360	1.94		

Table 5.1.3(a) Electron Microprobe Data on Fe-Fe-2% Ni Diffusion
couple reacted at 1494°C for 1200 seconds

Initial	Serial No	wt% Ni	I (cps)	background (cps)	Final I (cps)	$\frac{I}{I_0}$
	1	100	18817	87	18730	1.0
	2	1	299	87	212	0.0113
	3	2	493	87	406	0.0216
	4	3	681	87	594	0.0317
Final	Serial No	wt% Ni	I (cps)	background (cps)	Final I (cps)	$\frac{I}{I_0}$
	1	100	21321	90	21231	1.0
	2	1	306	90	216	0.01017
	3	2	479	90	389	0.01832
	4	3	712	90	622	0.02930

Table 5.1.3(b) Concentration Penetration Curve of Ni at 1494°C

Dist. from Interface (μm)	wt% Ni	Dist. from Int. (μm)	wt% Ni	Dist. from Int. (μm)	wt% Ni	Dist. from Int. (μm)	wt% Ni
-580	0.02	-250	0.15	50	1.24	380	1.83
-550	0.01	-220	0.27	80	1.31	410	1.88
-520	0.025	-190	0.31	110	1.42	440	1.90
-490	0.04	-160	0.36	140	1.48	470	1.98
-460	0.03	-130	0.41	170	1.55	500	1.95
-430	0.03	-100	0.60	200	1.57	530	1.94
-400	0.045	- 70	0.66	230	1.64	560	1.93
-370	0.080	- 40	0.86	260	1.69	590	1.97
-340	0.130	- 10	1.04	290	1.73	620	1.87
-310	0.14	Int.= 0	0.95	320	1.77	650	1.91
-280	0.17	20	1.05	350	1.81	680	1.92

Table 5.1.4 (a) Diffusivity of Ni in δ -Fe

Temperature $^{\circ}\text{C}$	Reaction time seconds	$D_{\text{Ni}}^{\delta\text{-Fe}}$ cm^2/sec $\times 10^7$
1473	1800	1.38
1484	1500	1.55
1494	1200	1.72

Table 5.1.4 (b) Data for Arrhenius Plot for $D_{\text{Ni}}^{\delta\text{-Fe}}$

Temp. $^{\circ}\text{C}$	Temp. $^{\circ}\text{A}$	$\frac{1}{T} \times 10^4 \text{ } ^{\circ}\text{K}^{-1}$	$D \text{ cm}^2/\text{sec}$ $\times 10^7$	Log D
1473	1746	5.72	1.38	-6.8601
1484	1757	5.69	1.55	-6.8097
1494	1767	5.66	1.72	-6.7645

Table 5.1.5(a) Data on Diffusivities of Ni in α -Fe, γ -Fe δ -Fe and liquid-Fe

No.	Phase	Temp. °C	Temp. °A	$\frac{1}{T}$ °K ⁻¹ x10 ⁴	D cm ² /sec.	Log ₁₀ D
1	α -Fe (ref.46)	699.6	972.6	10.2	3.75x10 ⁻¹⁴	-13.426
		723.7	996.7	10.0	9.96x10 ⁻¹⁴	-13.001
		740.2	1013.2	9.86	2.32x10 ⁻¹³	-12.634
		759.7	1032.7	9.68	4.70x10 ⁻¹³	-12.328
		781.7	1054.7	9.48	1.17x10 ⁻¹²	-11.932
		800.3	1073.3	9.31	2.56x10 ⁻¹²	-11.592
		828.8	1101.8	9.07	4.91x10 ⁻¹²	-11.309
		858.6	1131.6	8.83	11.50x10 ⁻¹²	-10.939
		891.6	1164.6	8.58	24.0x10 ⁻¹²	-10.619
		899.6	1172.6	8.52	29.9x10 ⁻¹²	-10.524
2	γ -Fe (ref.47)	930	1203	8.31	4.25x10 ⁻¹³	-12.3716
		960	1233	8.11	1.31x10 ⁻¹²	-11.8827
		1000	1273	7.85	2.37x10 ⁻¹²	-11.6253
		1050	1323	7.56	6.01x10 ⁻¹²	-11.2211
3	δ -Fe (This work)	1473	1746	5.72	1.38x10 ⁻⁷	-6.8601
		1484	1757	5.69	1.55x10 ⁻⁷	-6.8095
		1494	1767	5.66	1.72x10 ⁻⁷	-6.7645
4	Liquid (ref.45)	1576	1849	5.41	4.08x10 ⁻⁵	-4.3893
		1600	1873	5.34	4.82x10 ⁻⁵	-4.3170
		1650	1923	5.20	5.22x10 ⁻⁵	-4.2823

Table 5.1.5(b) Activation Energies for Ni diffusion in
 α -Fe, δ Fe, γ Fe

No.	α -Fe	γ -Fe	δ -Fe
Activation energy (cal/mole)	61,900	67,000	62,700
D_0 (cm ² /sec)	9.9	0.77	11.2

Table 5.2.1(a) Electron microprobe data for Ni Concentration
Profile in Fe-1.92 wt% Ni binary alloy
(elliptical button)

Stage	No.	Composition wt% Ni	Av. counts	background counts	Final I (cps)	$\frac{I}{I_0}$
Initial	1	100	17849	78	17771	1.0
	2	1	224	78	146	0.00822
	3	2	386	78	308	0.01728
	4	3	536	78	458	0.02580
Final	1	100	18788	78	18710	1.0
	2	1	243	78	165	0.00882
	3	2	433	78	325	0.01820
	4	3	586	78	508	0.02620

Table 5.2.1(b) Electron Microprobe data for Ni concentration profile in Fe-2.04 wt% Ni - 0.32 wt% C ternary alloy (elliptical button)

Stage	No	Composition wt% Ni	Average counts	background counts	Final I (cps)	$\frac{I}{I_0}$
Initial	1	100	19597	87	19510	1.00
	2	1	249	87	162	0.0083
	3	2	425	87	338	0.01732
	4	3	601	87	514	0.02670
Final	1	100	20980	87	20893	1.00
	2	1	262	87	175	0.00838
	3	2	444	87	357	0.0170
	4	3	650	87	563	0.0270

Table 5.2.2 Segregation Indices of Ni in Fe-1.92 wt% Ni binary and Fe-2.04 Wt% Ni-0.32 wt% C ternary alloys (elliptical buttons)

Sample	C_M	C_m	ΔC_{Ni}	$S = \frac{C_M}{C_m}$
Binary Fe-1.92% Ni	2.25	1.60	0.650	1.407
Ternary Fe-2.04% Ni-0.32C	2.675	1.80	0.875	1.485

Table 5.2.3 Composition of the directionally solidified samples

No	Composition			G °C/cm	R cm/sec
	wt% Ni	wt% C	wt% Fe		
1	2.06	-	Bal.	22.7	2.778×10^{-3}
2	1.98	0.48	Bal.	22.7	2.778×10^{-3}
3	2.02	0.40	Bal.	22.7	2.778×10^{-3}
4	2.01	0.58	Bal.	22.7	2.778×10^{-3}
5	2.90	-	Bal.	22.7	2.778×10^{-3}

Table 5.2.4 Electron Probe data for Ni concentration Profiles of Ni in Fe-2.06% Ni alloy for (a) Top Transverse Section

Initial	Serial No.	wt% Ni	I (cps)	background (cps)	Final I (cps)	$\frac{I}{I_0}$
	1	100	17596	80	17516	1.0
	2	1	234	80	154	0.008791
	3	2	392	80	312	0.017812
	4	3	555	80	475	0.027118
Final	Serial No	wt% Ni	I (cps)	background (cps)	Final I (cps)	$\frac{I}{I_0}$
	1	100	18315	85	18230	1.0
	2	1	243	85	158	0.008667
	3	2	405	85	320	0.017553
	4	3	589	85	504	0.027646

Table 5.2.4 (b) Bottom transverse section

Initial	Serial No.	wt% Ni	I (cps)	background (cps)	Final I (cps)	$\frac{I}{I_0}$
	1	100	16315	72	16063	1.0
	2	1	205	72	133	0.008280
	3	2	333	72	261	0.016250
	4	3	489	72	417	0.02600

Final	Serial No.	wt% Ni	I (cps)	background (cps)	Final I (cps)	$\frac{I}{I_0}$
	1	100	16503	73	16430	1.0
	2	1	211	73	138	0.00840
	3	2	350	73	271	0.016860
	4	3	475	73	402	0.024467

Table 5.2.5 Electron microprobe data for Ni concentration profiles in Fe-2.01 wt% Ni - 0.58 wt% C ternary alloy for (a) Top transverse section

Initial	Serial No	% Ni	I (cps)	background (cps)	Final I (cps)	$\frac{I}{I_0}$
	1	100	18425	75	18350	1.0
	2	1	226	75	151	0.008229
	3	2	403	75	328	0.017875
	4	3	563	75	488	0.026594

Final	Serial No.	% Ni	I (cps)	background (cps)	Final I (cps)	$\frac{I}{I_0}$
	1	100	19726	82	19644	1.0
	2	1	244	82	162	0.008213
	3	2	414	82	332	0.016831
	4	3	577	82	495	0.025094

Table 5.2.5

(b) Bottom Transverse Section

Initial	Serial No.	% Ni	I (cps)	background (cps)	Final I (cps)	$\frac{I}{I_0}$
	1	100	17210	73	17137	1.0
	2	1	224	73	151	0.008811
	3	2	350	73	277	0.016164
	4	3	525	73	452	0.026376

Final	Serial No.	% Ni	I (cps)	background (cps)	Final I (cps)	$\frac{I}{I_0}$
	1	100	17093	82	17011	1.0
	2	1	231	82	149	0.008759
	3	2	376	82	294	0.017283
	4	3	527	82	445	0.026160

Table 5.2.6

Results on Microsegregation of Ni in Fe-2.06 wt% Ni binary alloy

Position of sect.	$\cdot G$ $^{\circ}C/cm$	R cm/sec $\times 10^3$	$\frac{G}{R} \times 10^{-3}$	C_{Max}	C_{min}	$S_I = \frac{C_M}{C_m}$
Top	22.7	2.778	7.2	2.76	1.62	1.7
3.6144 m m from top	22.7	2.778	7.2	2.22	1.68	1.32

Table 5.2.7 Results on Microsegregation of Ni in Fe
-2.01 wt% Ni - 0.58 wt% C ternary alloy

Position of sect.	G $^{\circ}\text{C}/\text{cm}$	R cm/sec $\times 10^3$	$\frac{G}{R} \times 10^{-3}$	C_{Max}	C_{min}	$S_{\text{I}} = \frac{C_{\text{M}}}{C_{\text{m}}}$
Top	22.7	2.778	7.2	2.8	1.8	1.55
3.07 mm from top	22.7	2.778	7.2	2.7	1.82	1.48

Table 5.2.8 Residual segregation in Fe-2.06 wt% Ni binary and
Fe-2.01 wt% Ni - 0.58 wt% C ternary alloys

Alloy	C_{M}	C_{m}	$S_{\text{I}} = \frac{C_{\text{M}}}{C_{\text{m}}}$	$\delta_{\text{i}} = \frac{C_{\text{M}}^{\text{t}} - C_{\text{m}}^{\text{t}}}{C_{\text{M}}^{\text{o}} - C_{\text{m}}^{\text{o}}}$
Binary Top	2.76	1.62	1.70	$\frac{0.54}{1.14} = 0.473$
3.6144 mm from top	2.22	1.68	1.32	
Ternary top	2.8	1.8	1.55	$\frac{0.88}{1.00} = 0.880$
3.07 mm ^m from top	2.7	1.82	1.48	

Table 5.2.9 Comparison of Segregation Indices of Ni
in Fe-2.06 wt% Ni binary and Fe-2.01 wt% Ni
- 0.58 wt% C ternary alloys (controlled direc-
tional solidification)

Serial No.	Alloy	Composition (wt%)			C_{Max}	C_{min}	$S_I = \frac{C_{Max}}{C_{min}}$
		% Ni	% C	% Fe			
1	Binary	2.06	-	Bal.	2.63	1.65	1.59
2	Ternary	2.01	0.58	Bal.	2.80	1.80	1.55

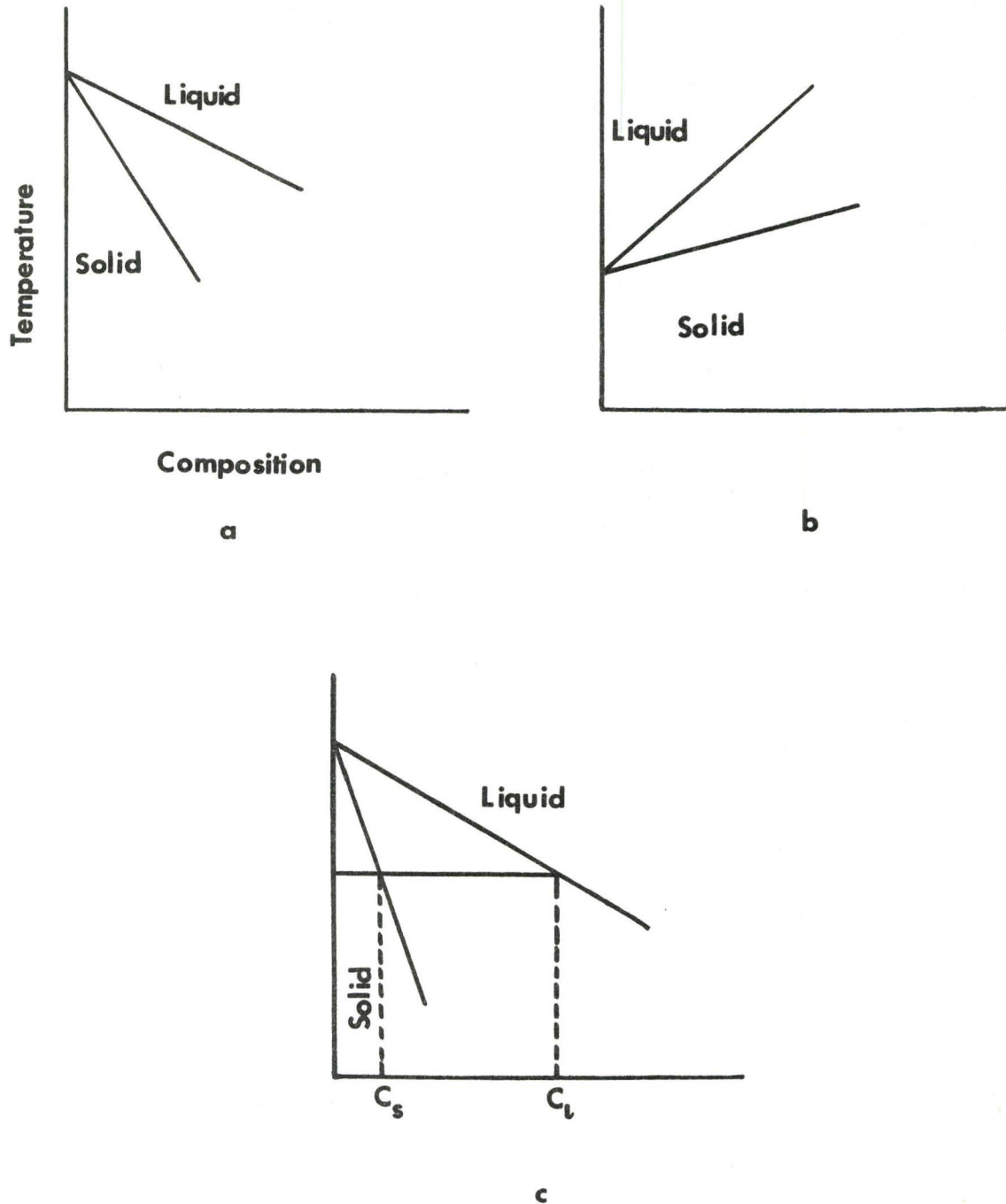


Fig. 2.2.1 (a) } Solidus Liquidus Relationships for a
 (b) } Dilute Binary Alloy

(c) Relationship between equilibrium compositions of Solid and Liquid

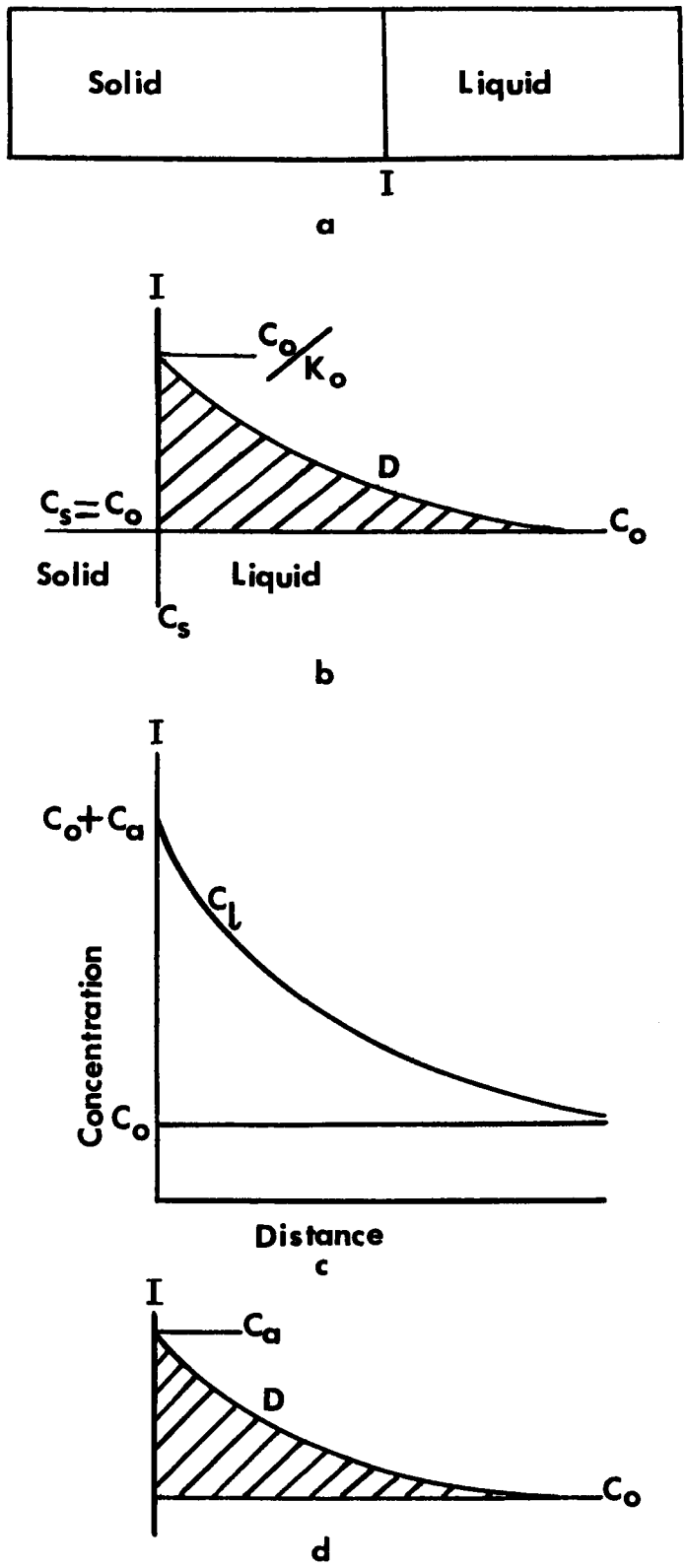


Fig. 2.2.2 (a) Geometry of unidirectional solidification
 (b) } Steady state distribution of solute
 (c) }
 (d) Distribution of solute during unidirectional solidification

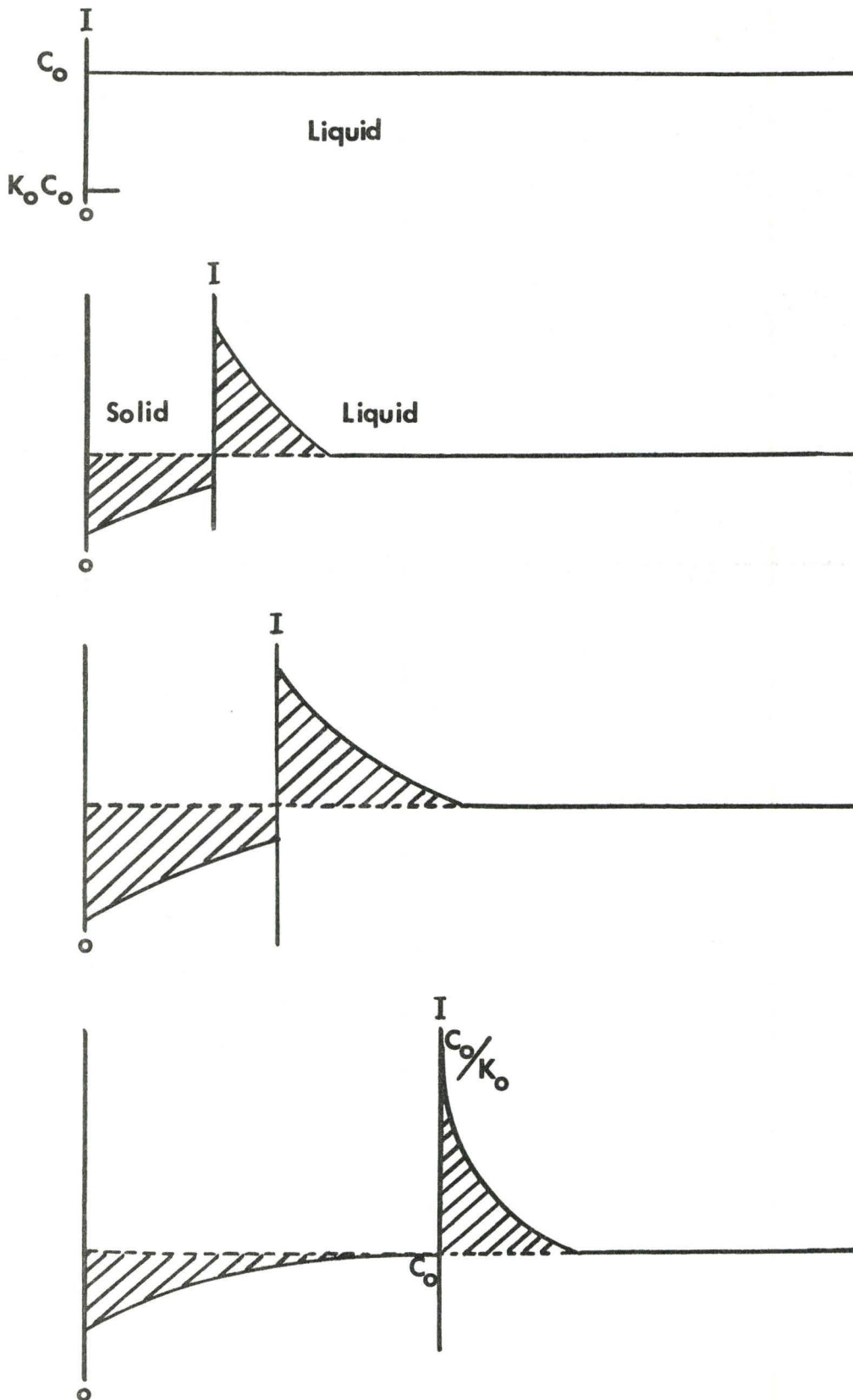


Fig. 2.2.3 Distribution of solute during initial transient

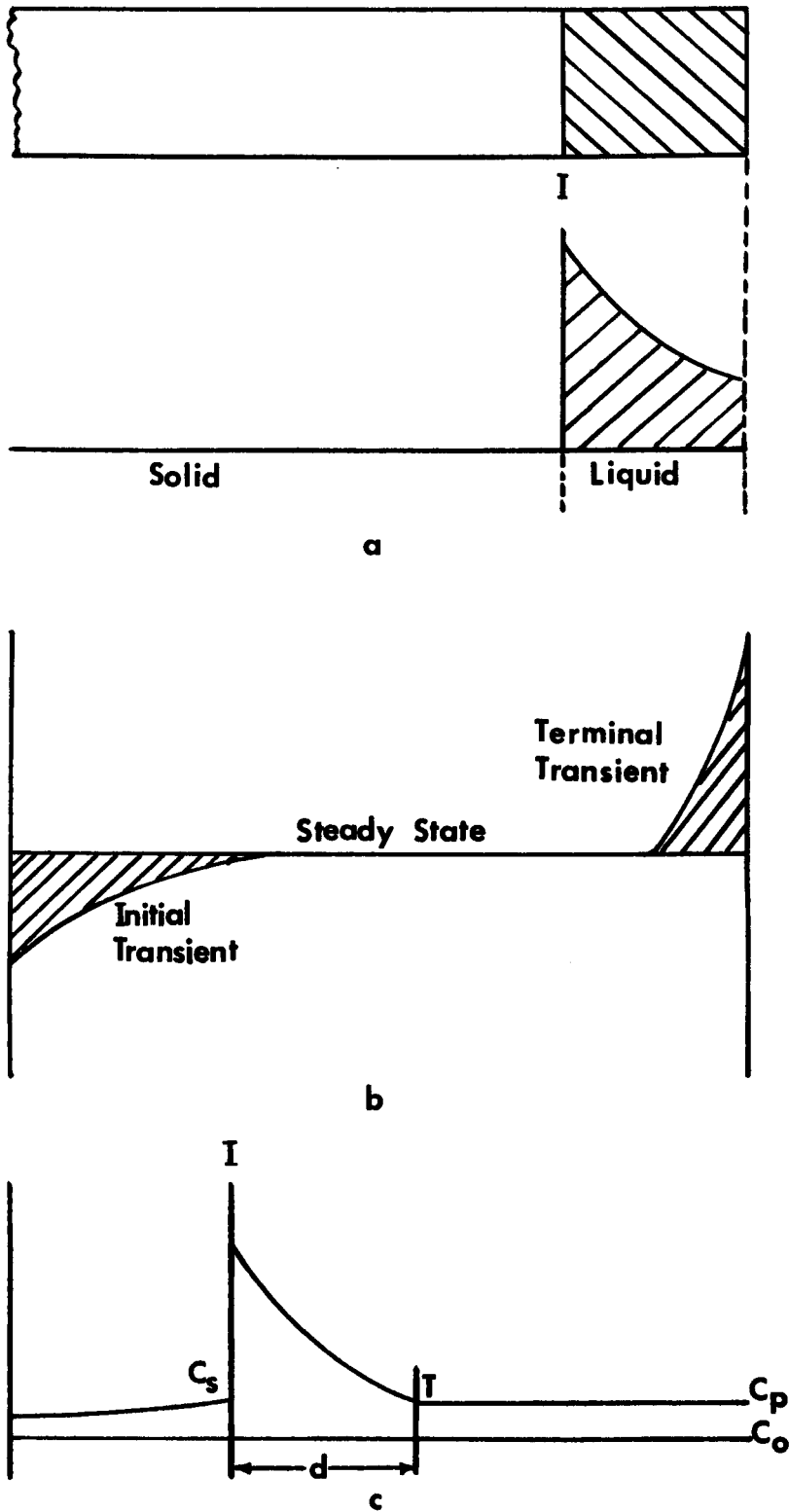


Fig. 2.2.4 (a) Distribution of solute during terminal transient
 (b) Final solute distribution
 (c) Effect of mixing on diffusion zone

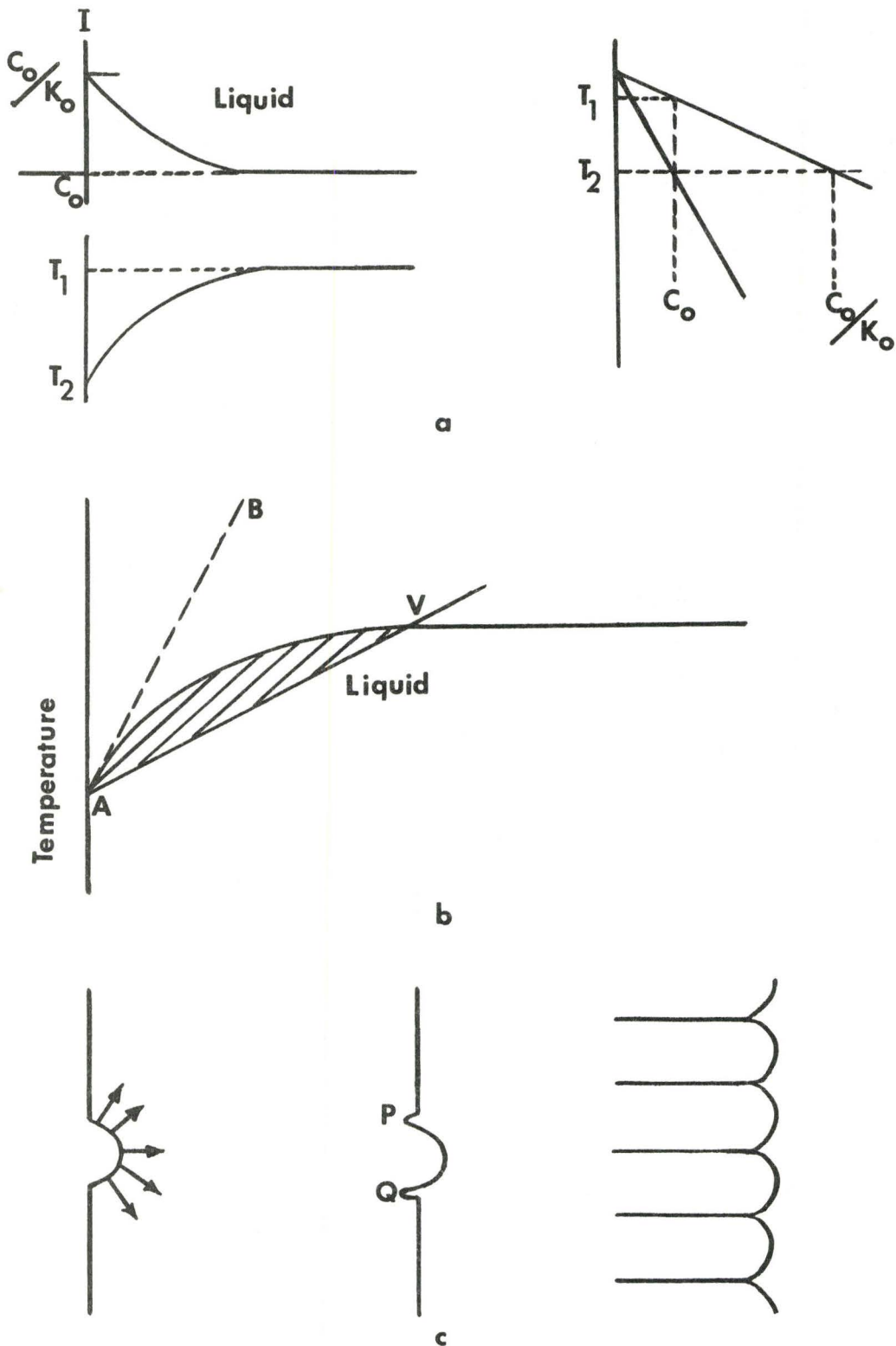


Fig. 2.3.1 (a) Variation of concentration and liquidus temperature ahead of solid-liquid interface
 (b) Constitutional supercooling ahead of Planar Interface
 (c) Development of cellular interface

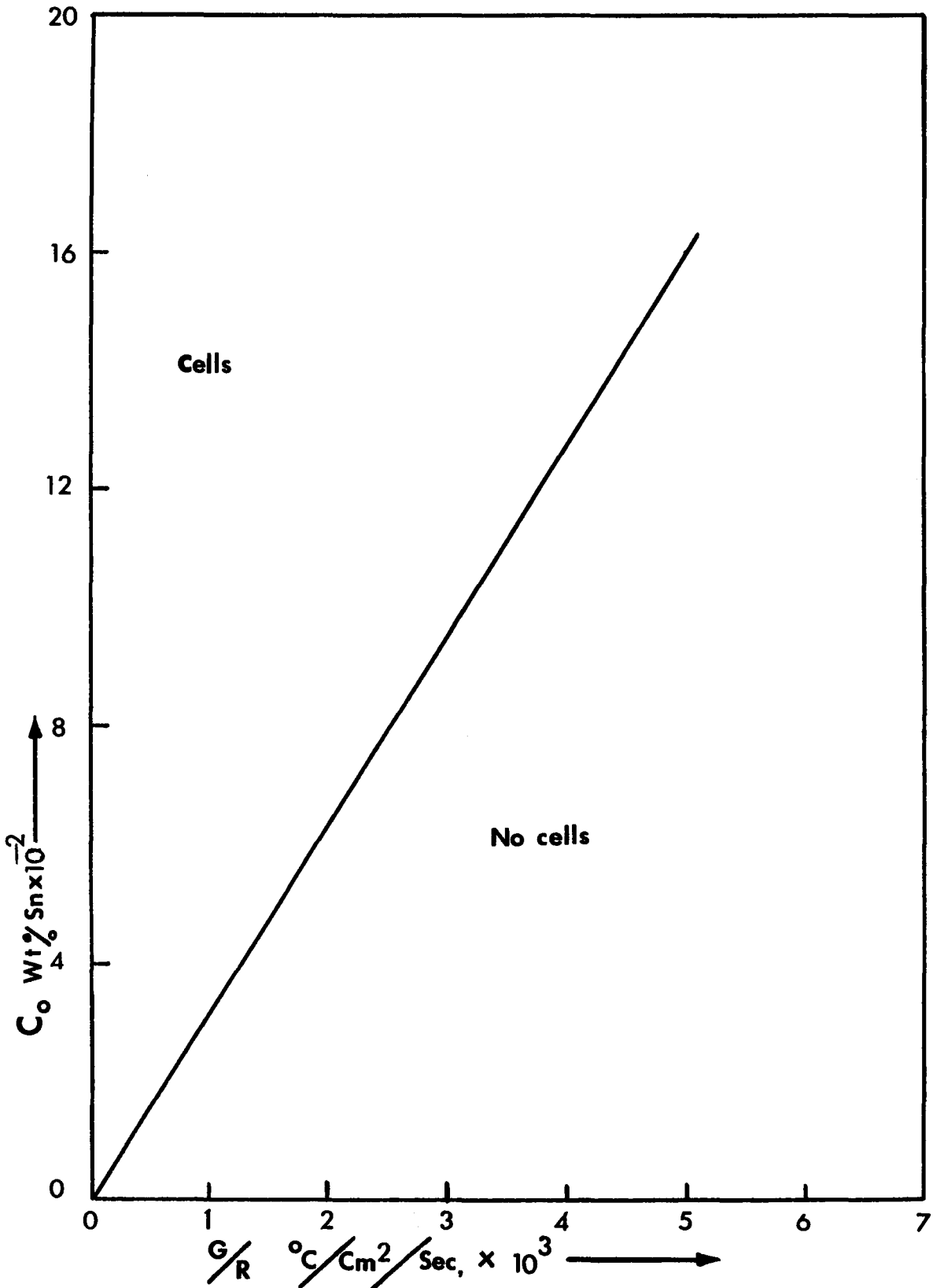


Fig. 2.3.2 Conditions for cellular solidification (Rutter ref.7)

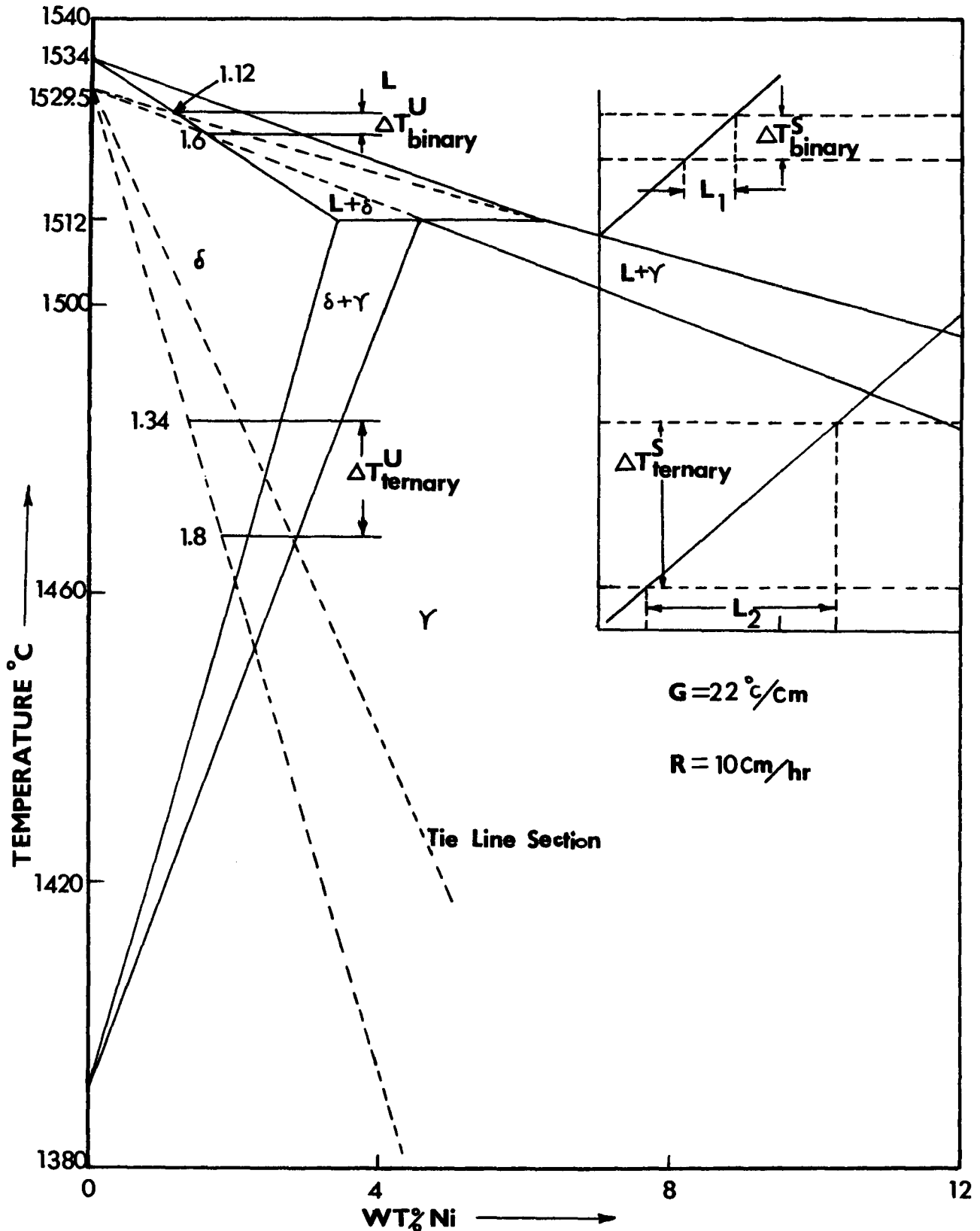


Fig. 3.1.1 Peritectic Region of Fe-Ni Binary Phase Diagram and Tie-Line Section for Fe-2.01 wt% Ni-0.58 wt% C Ternary

$\Delta T_{\text{Binary}}^{\text{U}}$ = Tip undercooling for Binary

$\Delta T_{\text{ternary}}^{\text{U}}$ = Tip undercooling for ternary

$\Delta T_{\text{Binary}}^{\text{S}}$ = Temperature range of solidification for Binary

$\Delta T_{\text{ternary}}^{\text{S}}$ = Temperature range of solidification for Ternary

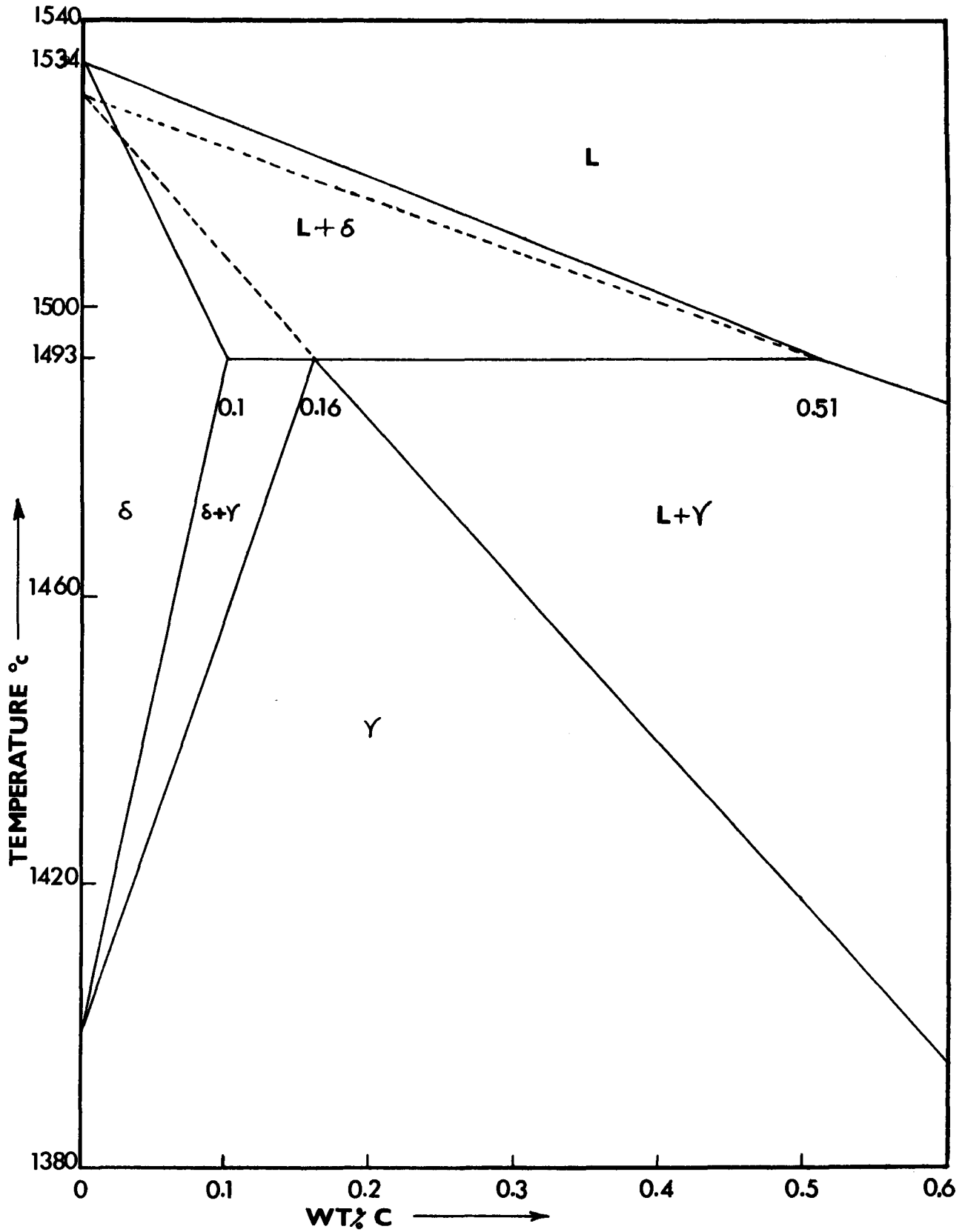
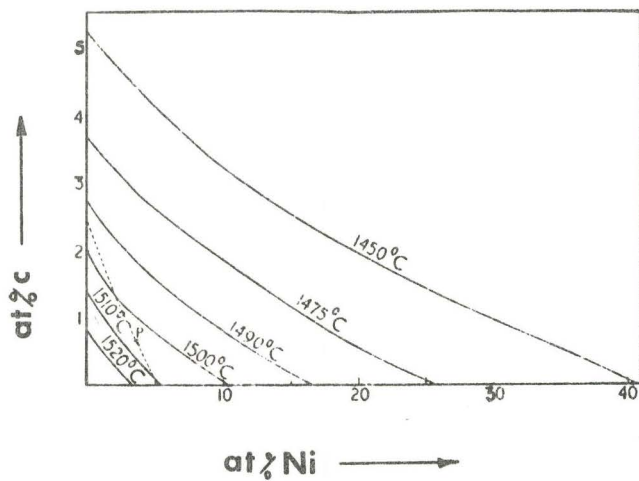
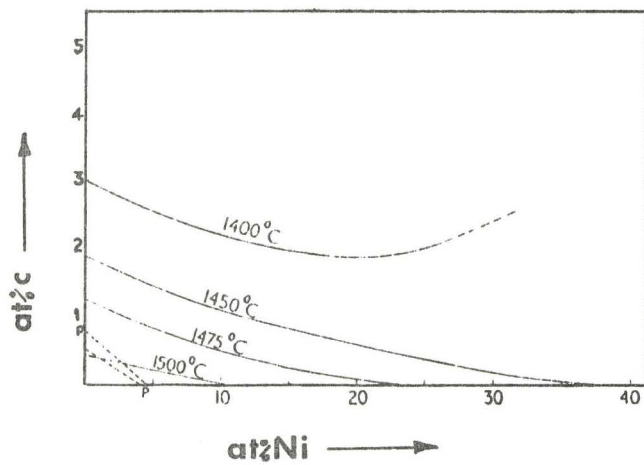


Fig. 3.1.2 Peritectic Region of Fe-C Binary Phase Diagram



a



b

Fig. 3.1.3 (a) Liquidus surface of Fe-Ni-C Ternary alloy
 (b) Solidus surface of Fe-Ni-C Ternary Alloy

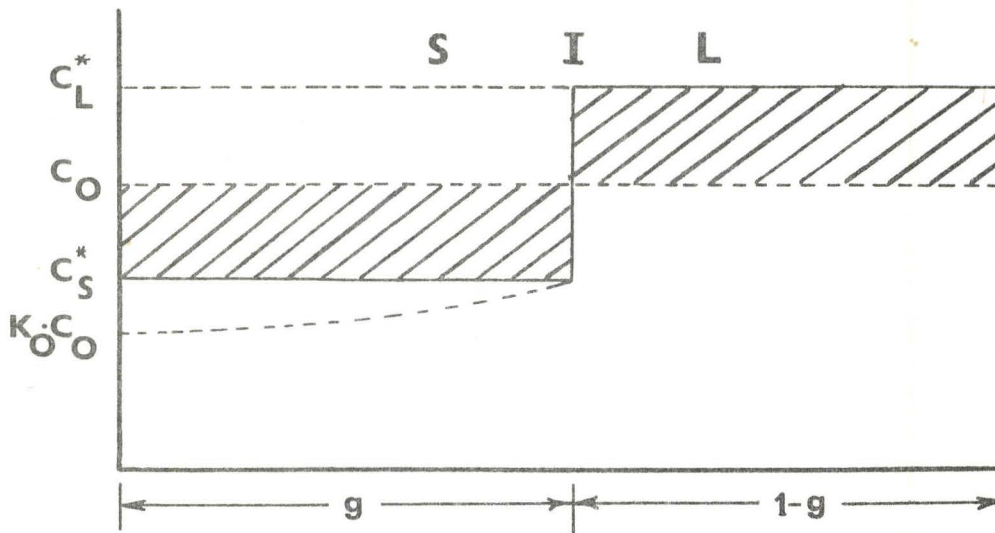


Fig. 3.2.2 (a) Mass Balance at S-L Interface in unidirectional solidification assuming complete mixing in both solid and liquid

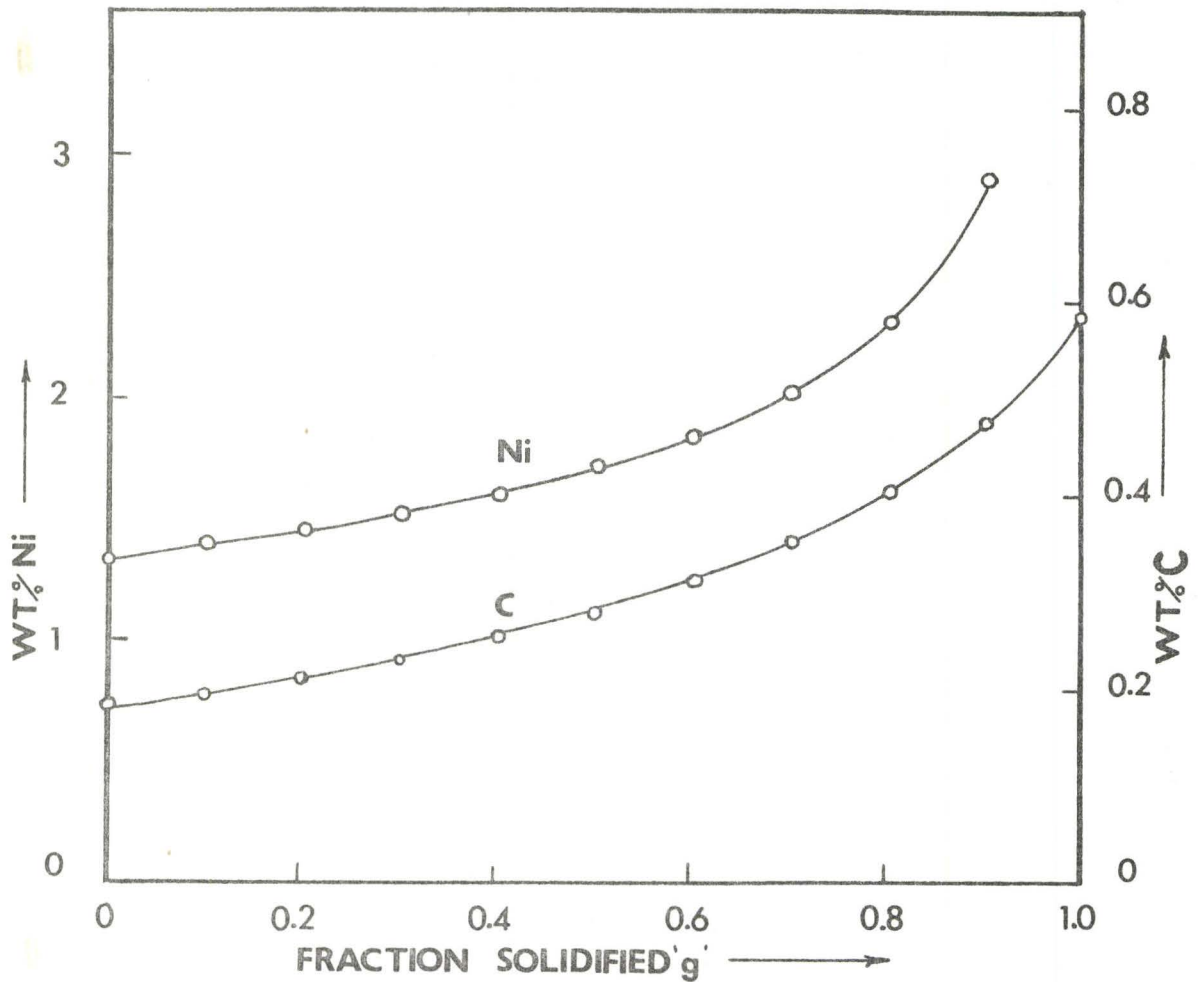


Fig. 3.2.2 (b) Scheil Chipman plots for Ni and C in Fe-2.01 wt% Ni-0.58 wt% C alloy

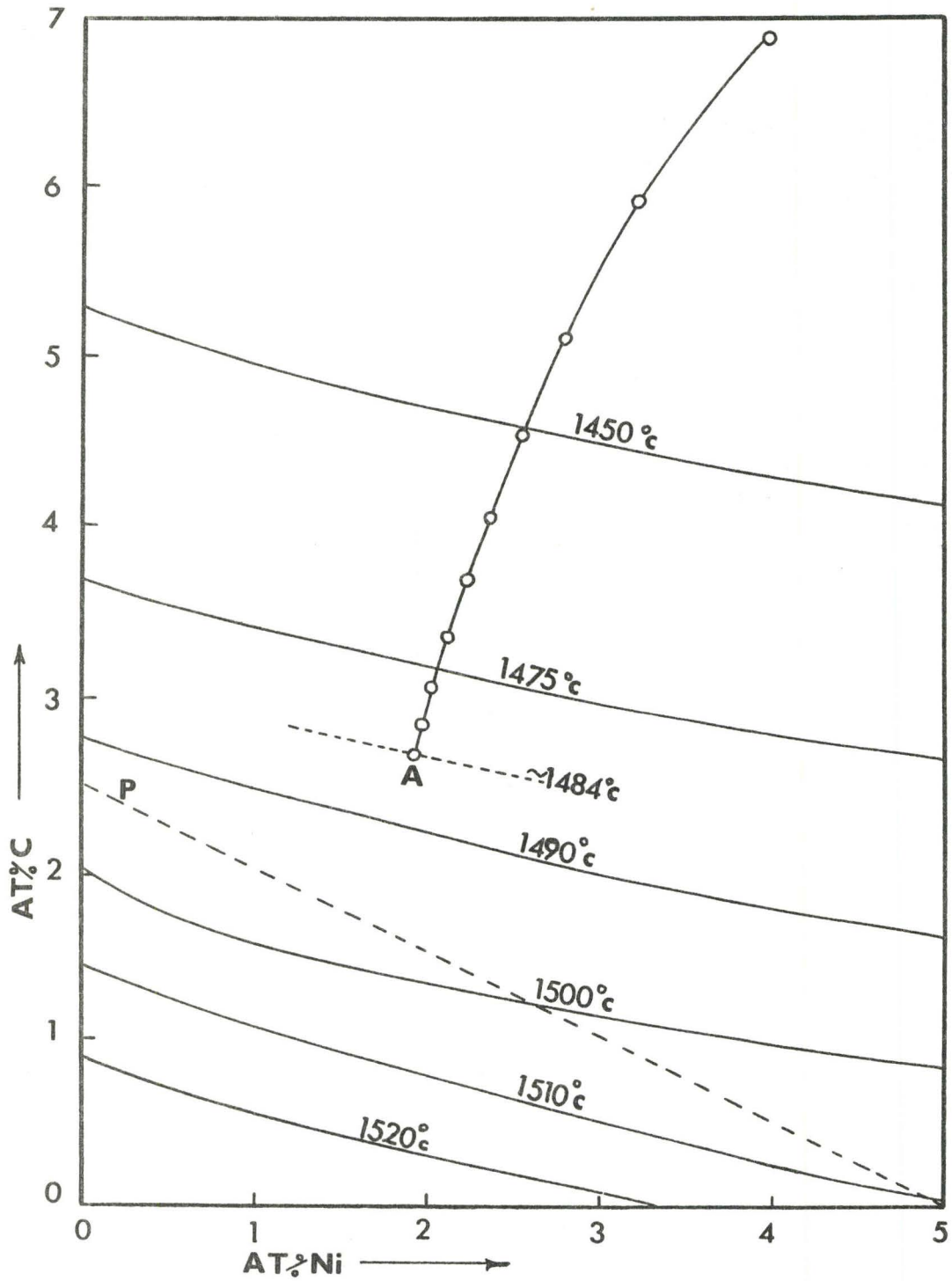


Fig. 3.2.3 (a) Segregation Path for Fe-2.01 wt% Ni-0.58 wt% C Ternary Alloy (Liquidus surface)

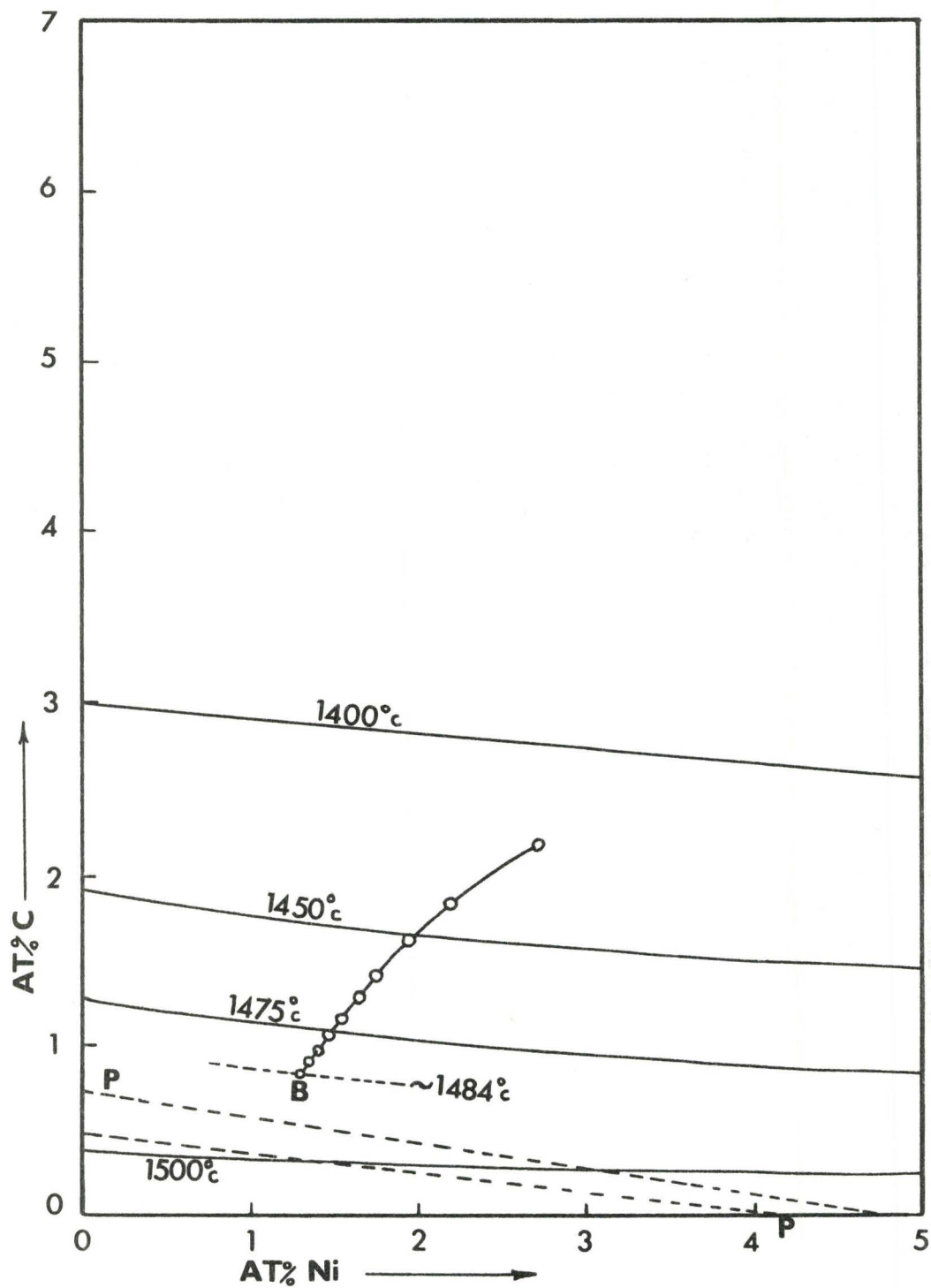


Fig. 3.2.3 (b) Segregation Path for Fe-2.01 wt% Ni - 0.58 wt% C Ternary Alloy (Solidus surface)

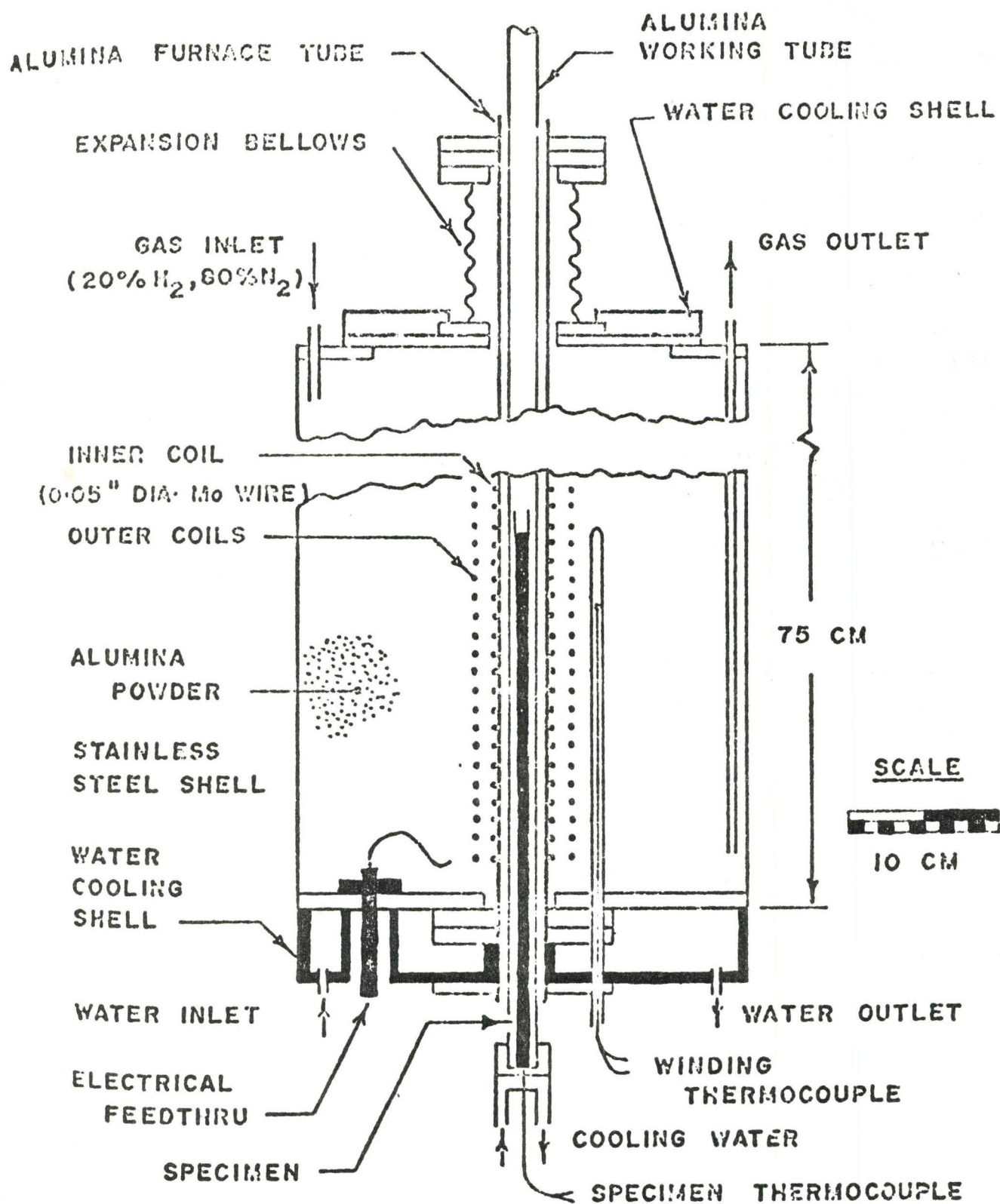


Fig. 4.1.1 Sectional view of the Resistance Furnace

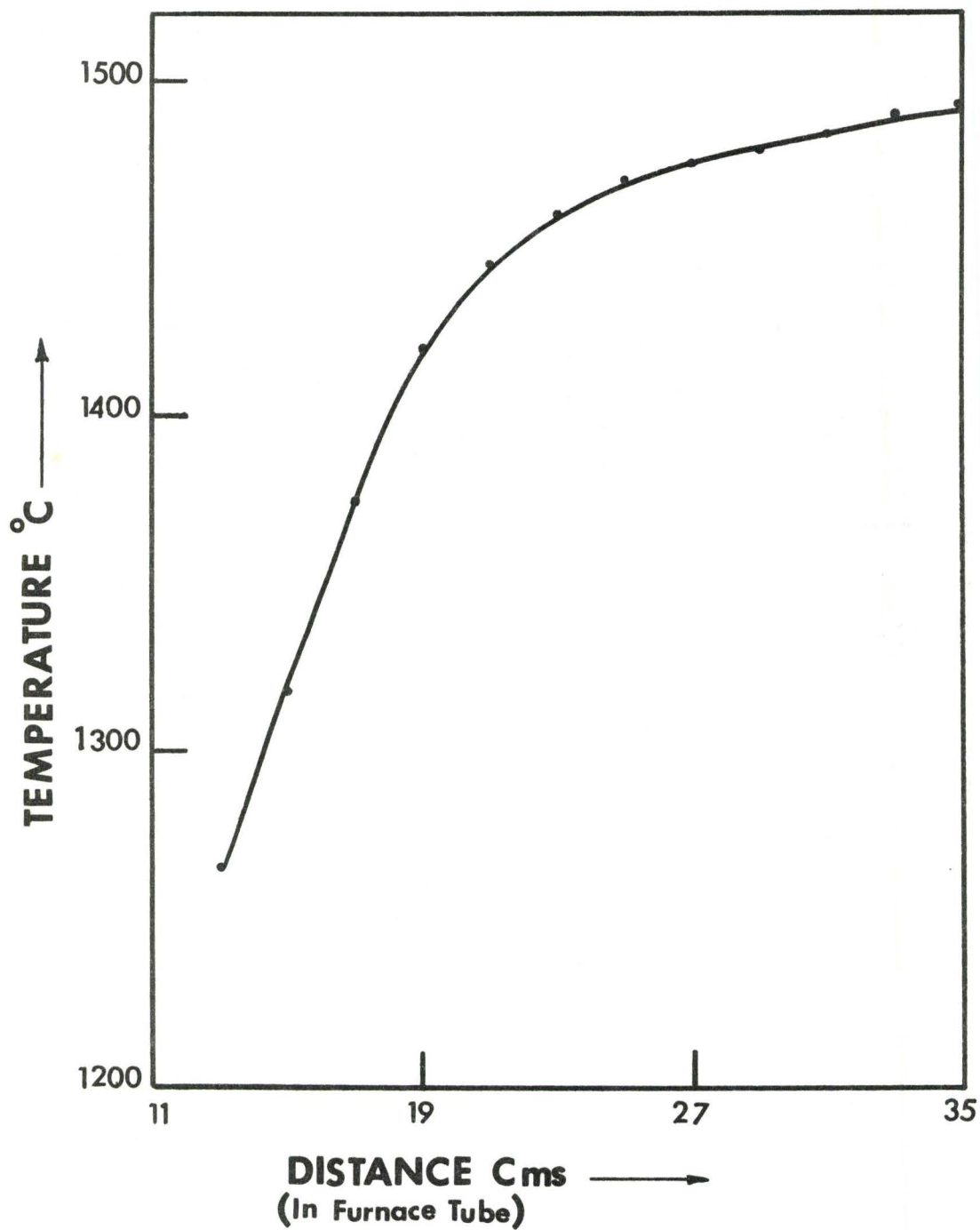


Fig. 4.2.1 Temperature profile for diffusivity experiment

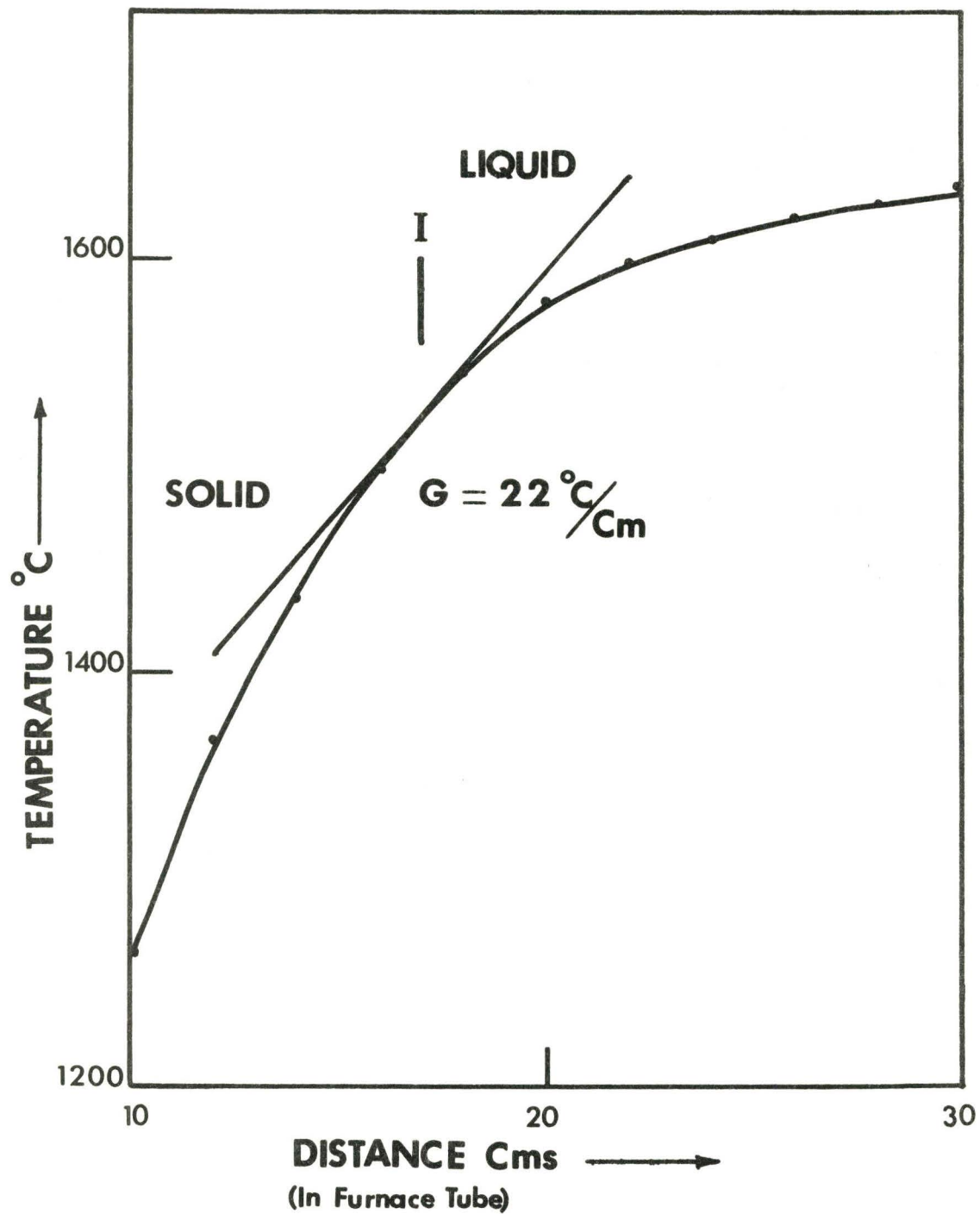


Fig. 4.3.1 Temperature Profile for a typical solidification run

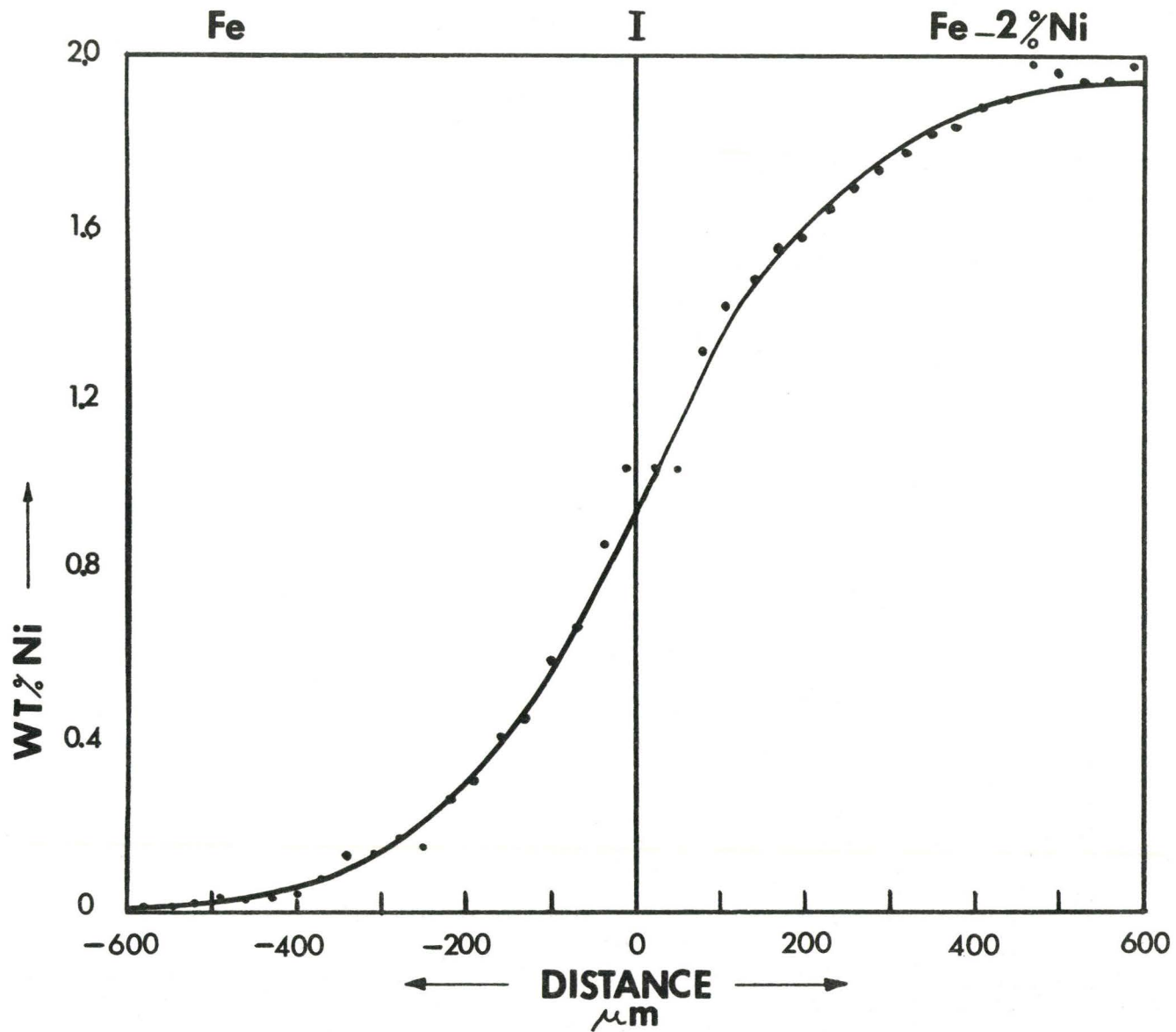


Fig. 5.1.1 Ni concentration penetration curve for Fe-Fe-2% Ni diffusion couple
 Reacted at 1473°C for 1800 seconds

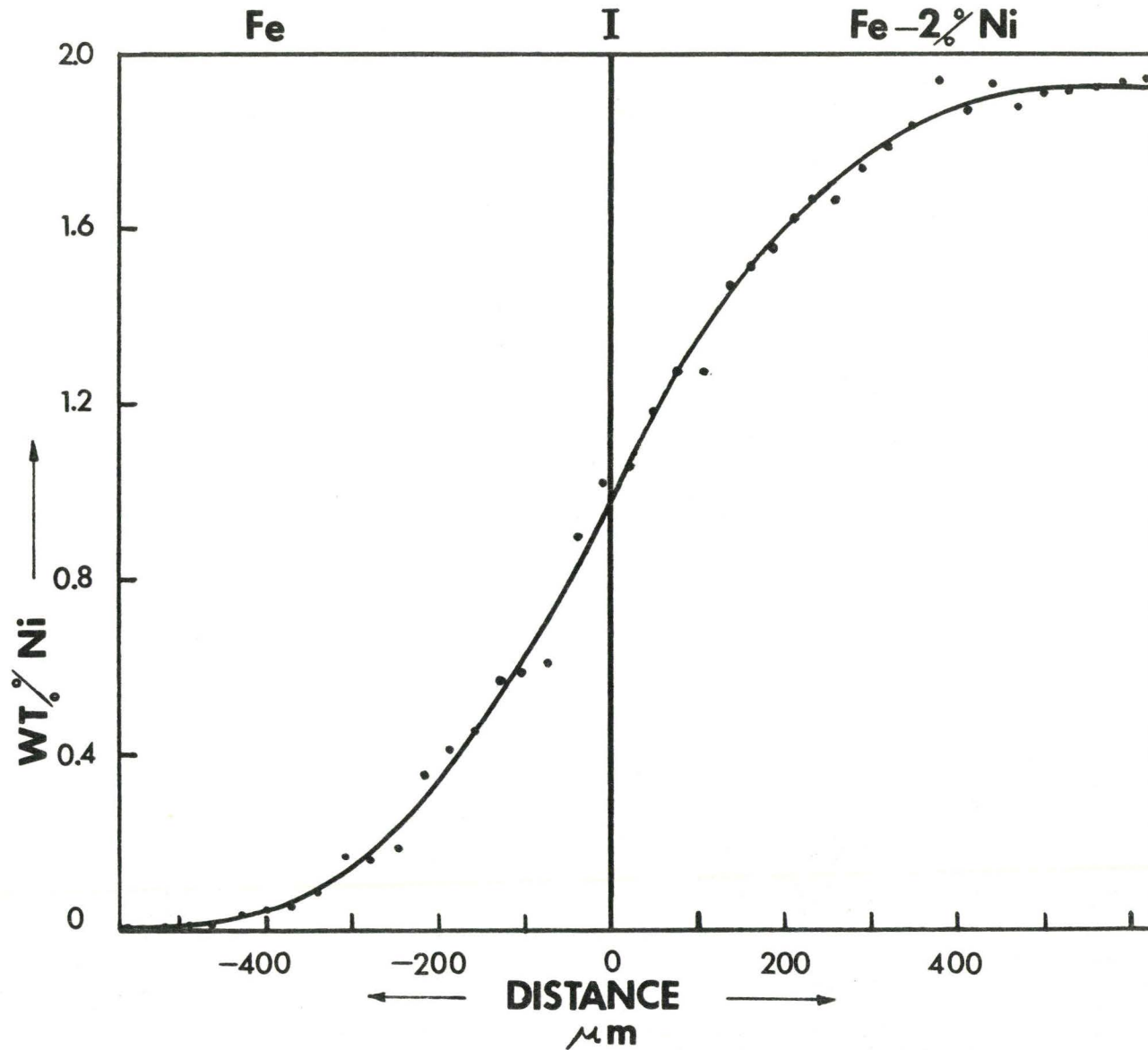


Fig. 5.1.2 Ni concentration penetration curve for Fe-2% Ni Diffusion couple
 Reacted at 1484°C for 1500 seconds

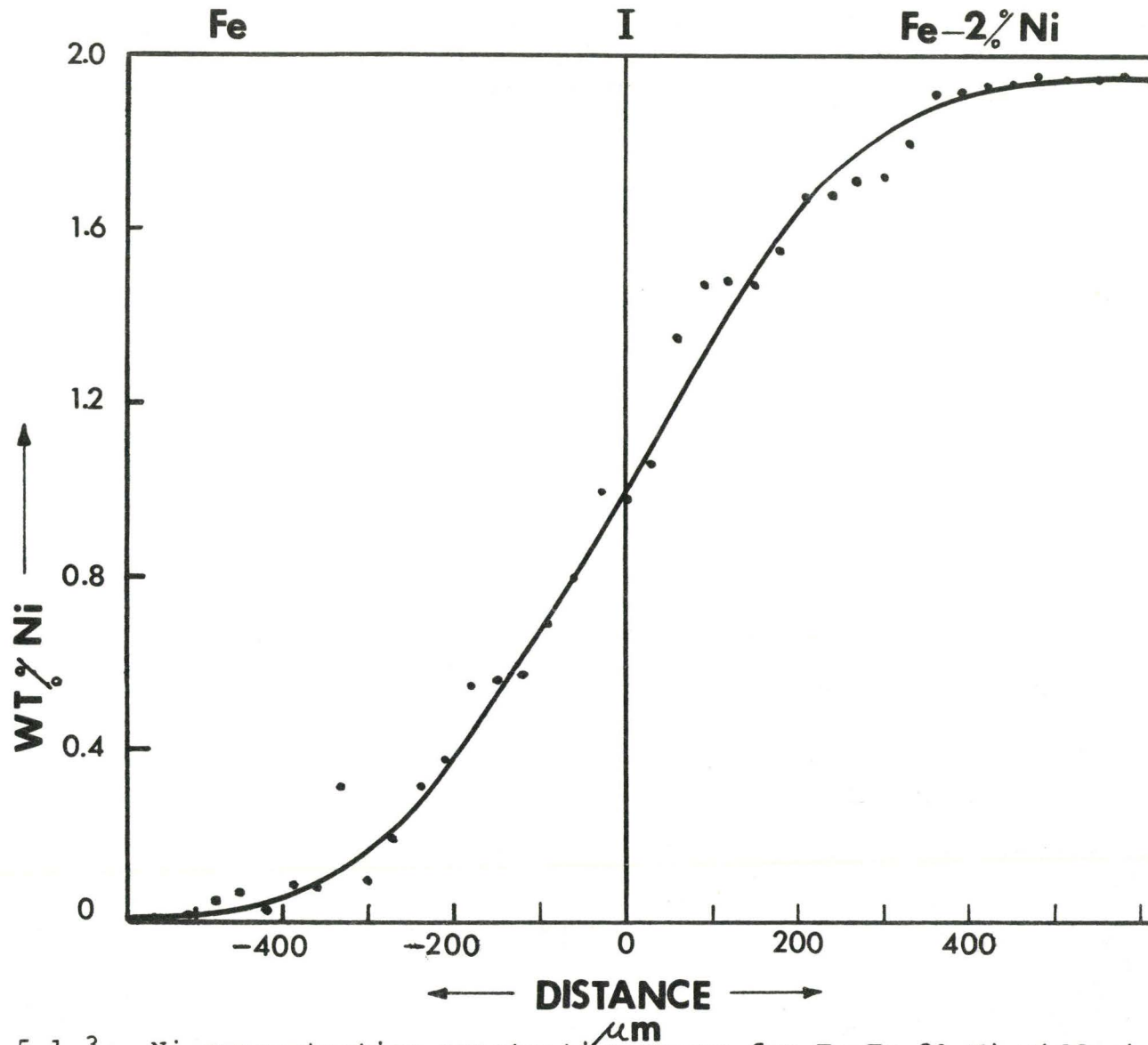


Fig. 5.1.3 Ni concentration penetration curve for Fe-Fe-2% Ni Diffusion couple
 Reacted at 1494°C for 1200 seconds

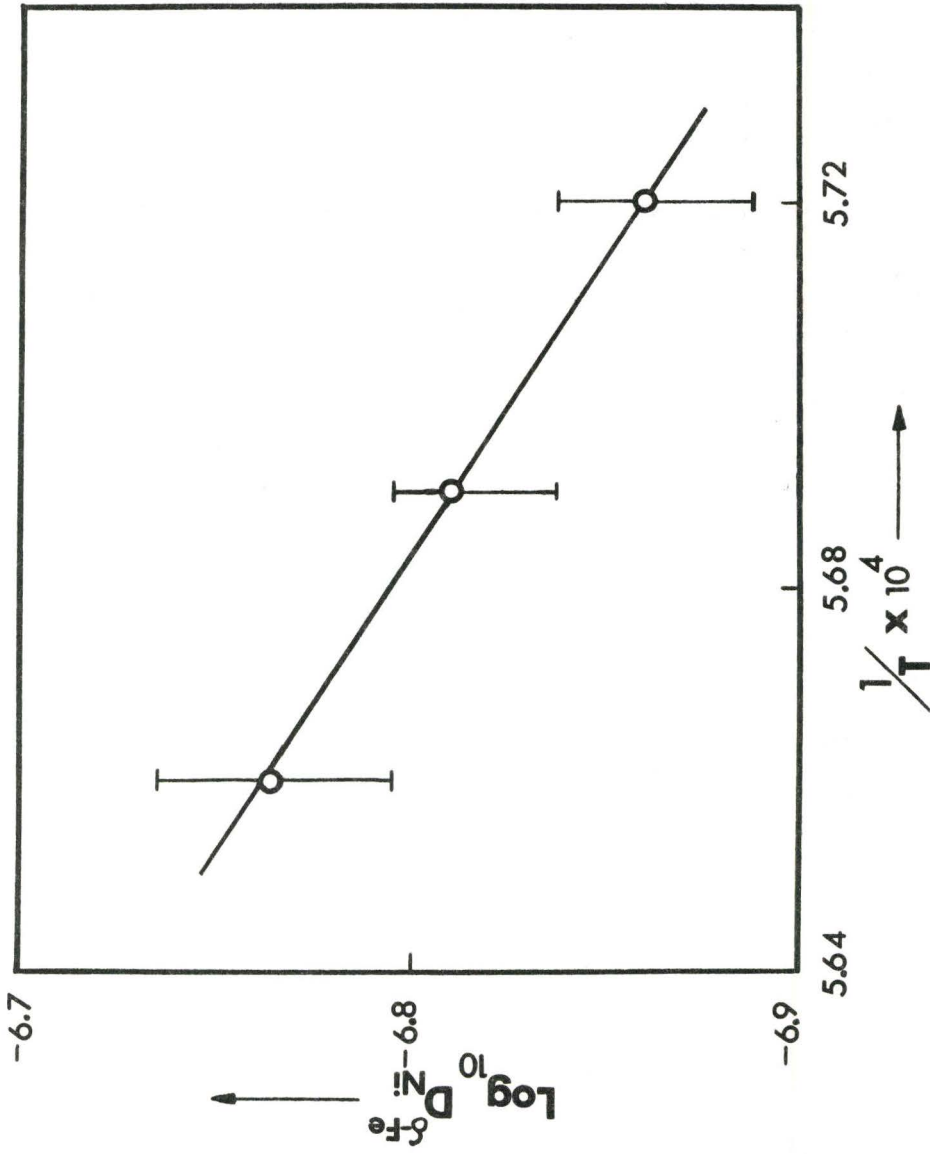


Fig. 5.1.4 Temperature dependence of $D_{Ni}^{\delta-Fe}$

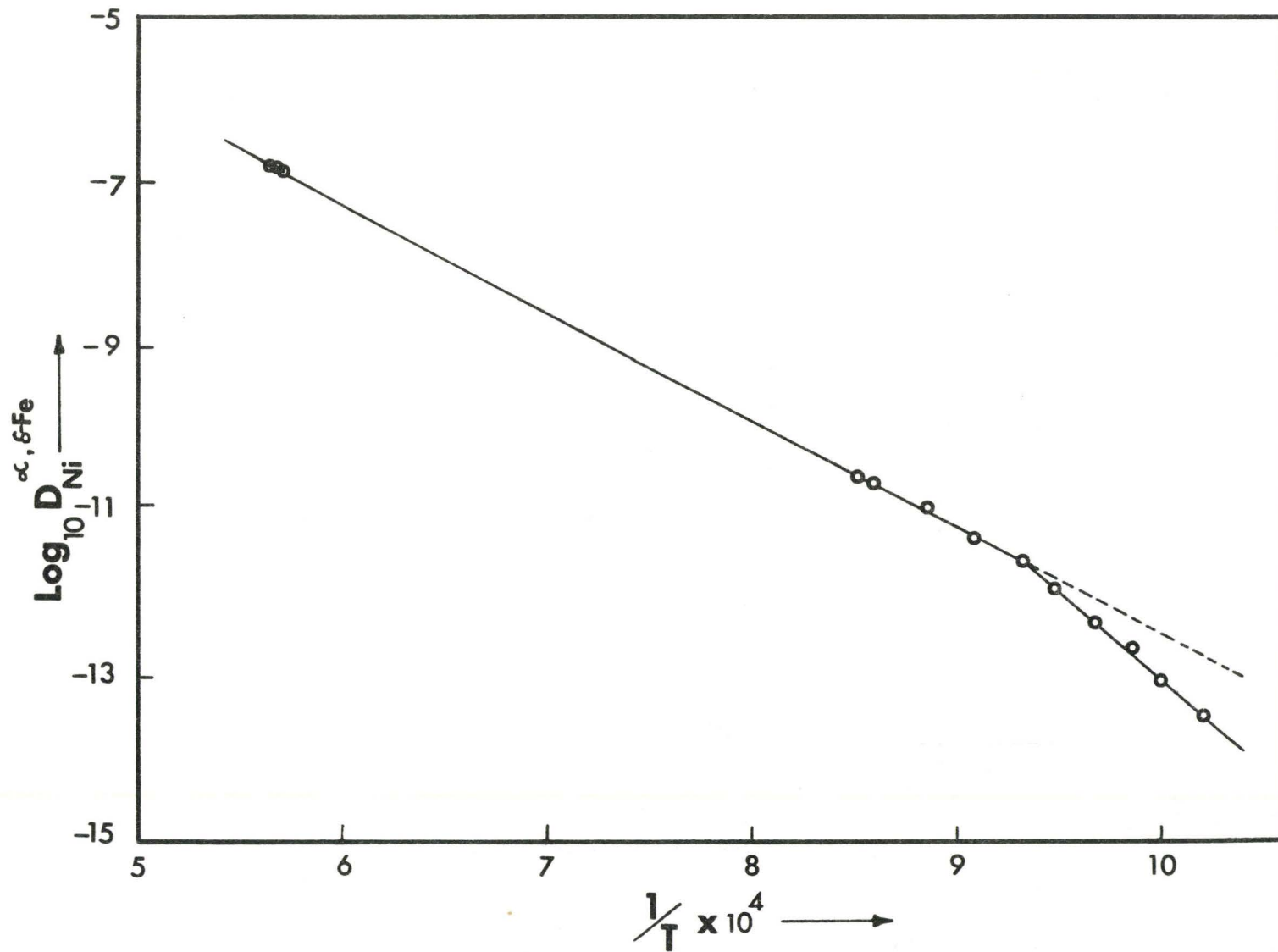


Fig. 5.1.5 Extrapolation of Temperature Dependence of $D_{\text{Ni}}^{\alpha\text{-Fe}}$ to $\delta\text{-Fe}$ range

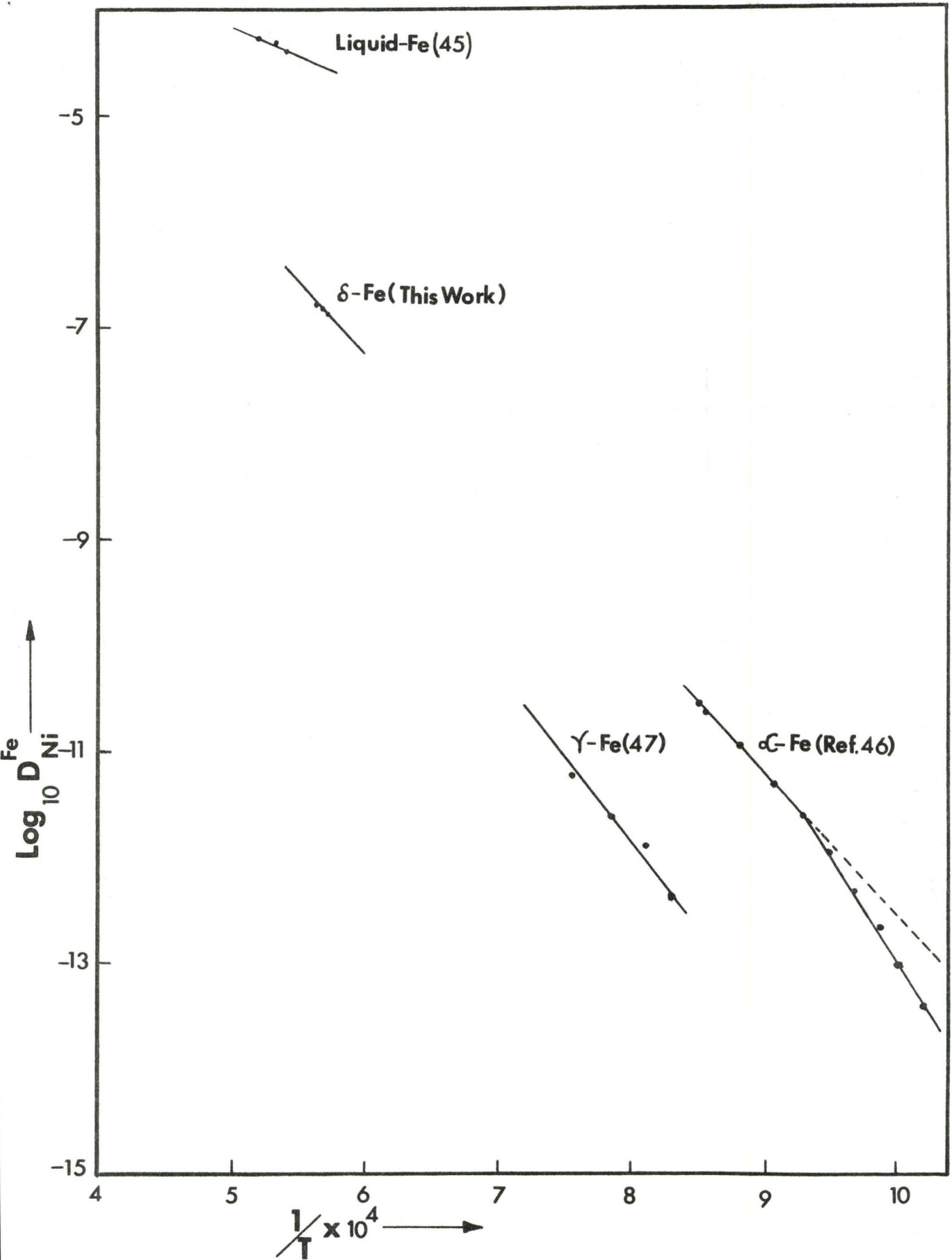
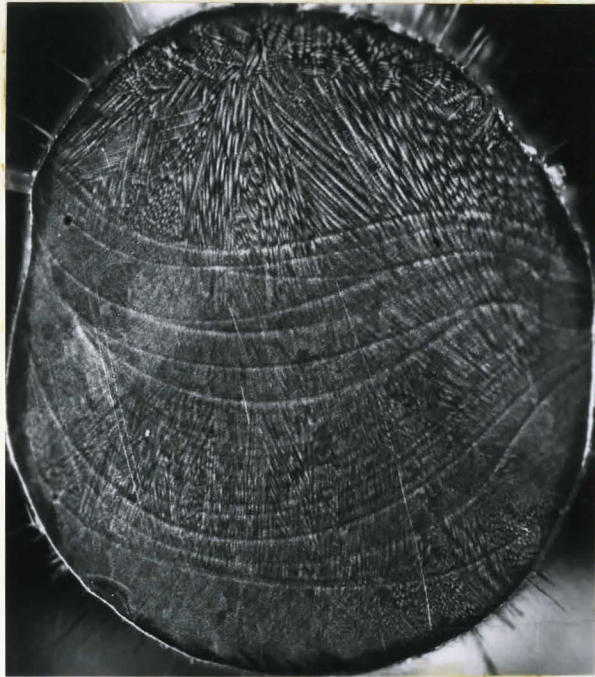
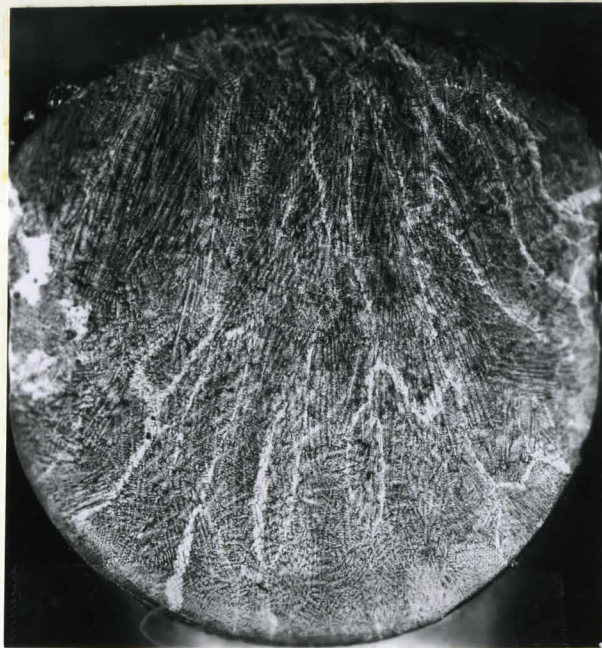


Fig. 5.1.6 Ni Diffusivities in different phases of Iron



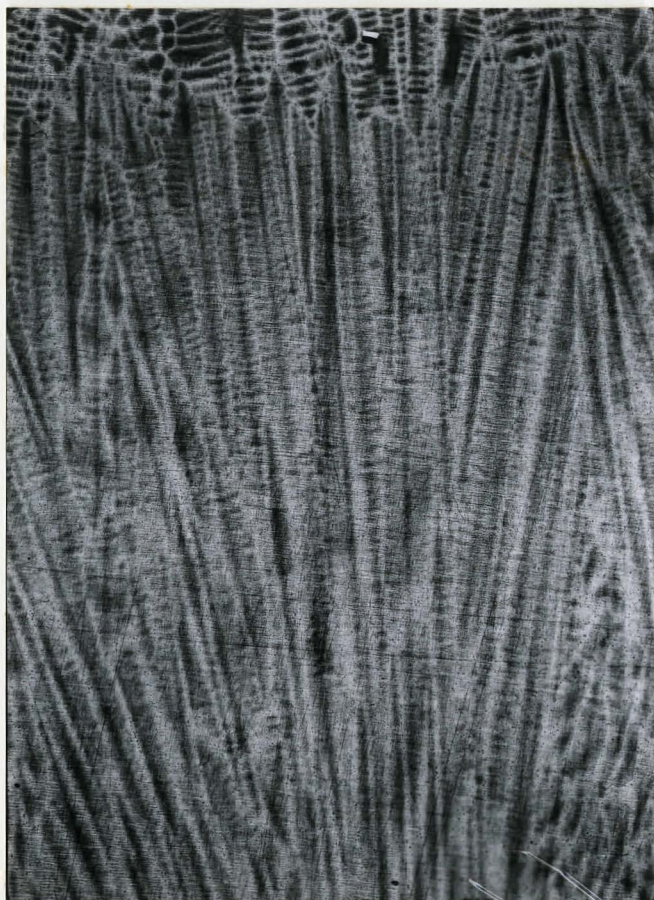
(a)



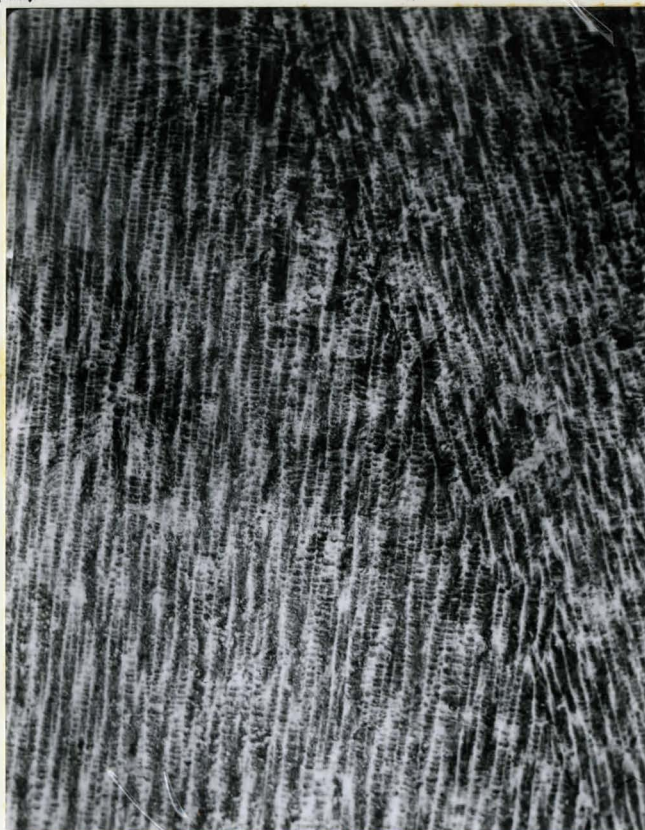
(b)

Fig. 5.2.1 (a) Growth morphology in Fe-1.92 wt% Ni Binary Alloy
(Argon arc ingot, section parallel to overall
growth direction)
(b) Growth morphology in Fe-2.04 wt% Ni - 0.207 wt% C
Ternary Alloy

Mag. 8x



(a)

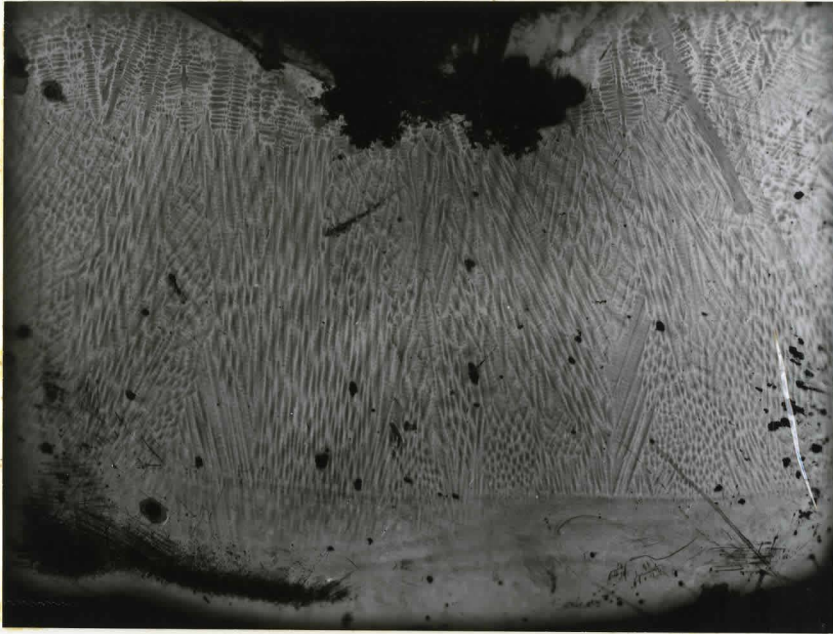


(b)

Fig. 5.2.2 (a) Directionally solidified portion of Fe-1.92 wt% Ni alloy (elliptical button)

(b) Directionally solidified portion of Fe-2.04 wt% Ni -0.32 wt% C alloy

Mag. 22x



(c)



(d)

Fig. 5.2.2 (c) Overall Dendritic growth in Fe-1.92 wt% Ni alloy
(elliptical button)

(d) Overall Dendritic growth in Fe-2.04 wt% Ni
0.32 wt% C alloy

Mag. 12 x

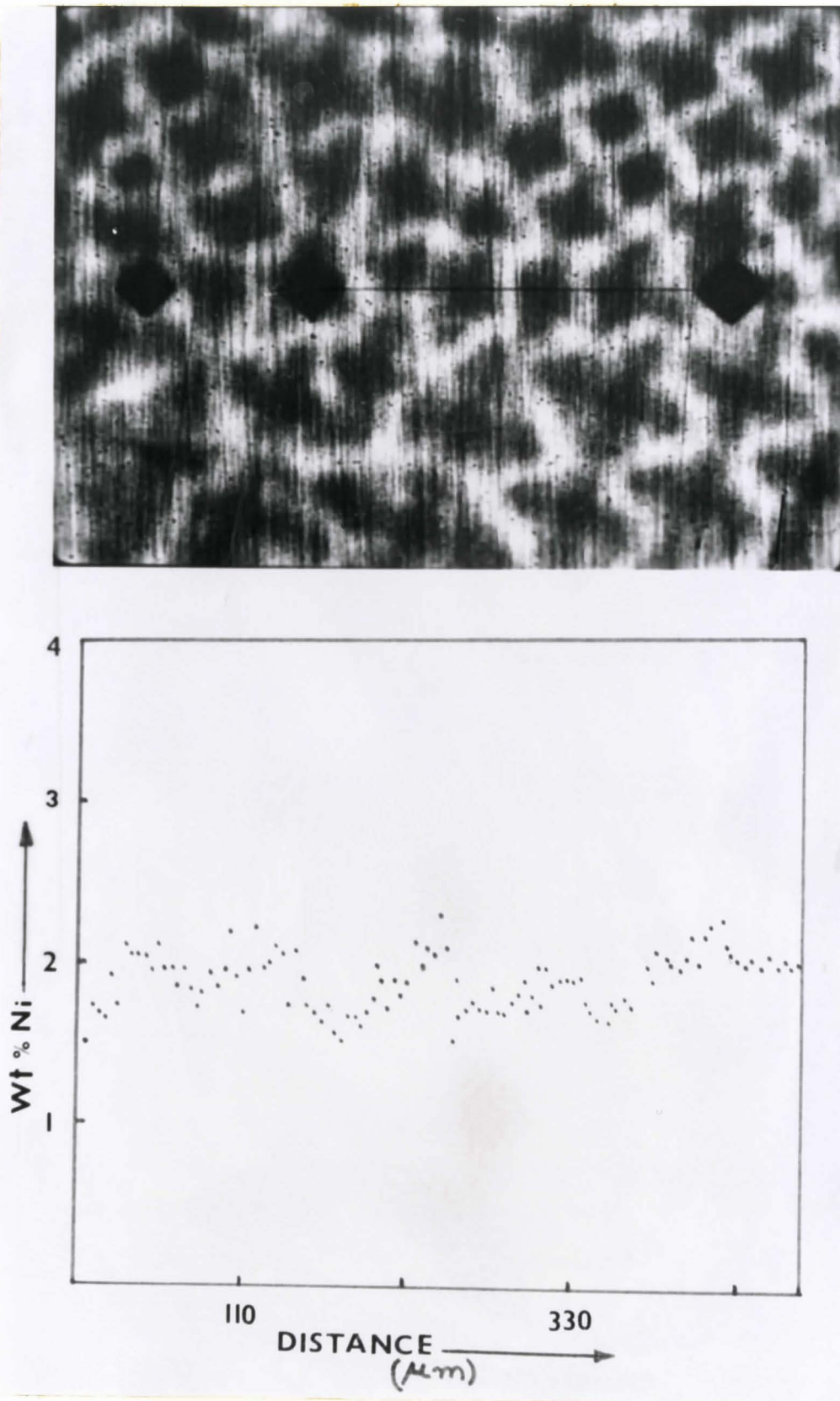


Fig. 5.2.3 Dendritic structure and Ni concentration profile in transverse section of Fe-1.92 wt% Ni alloy (elliptical button)

Mag. 60x

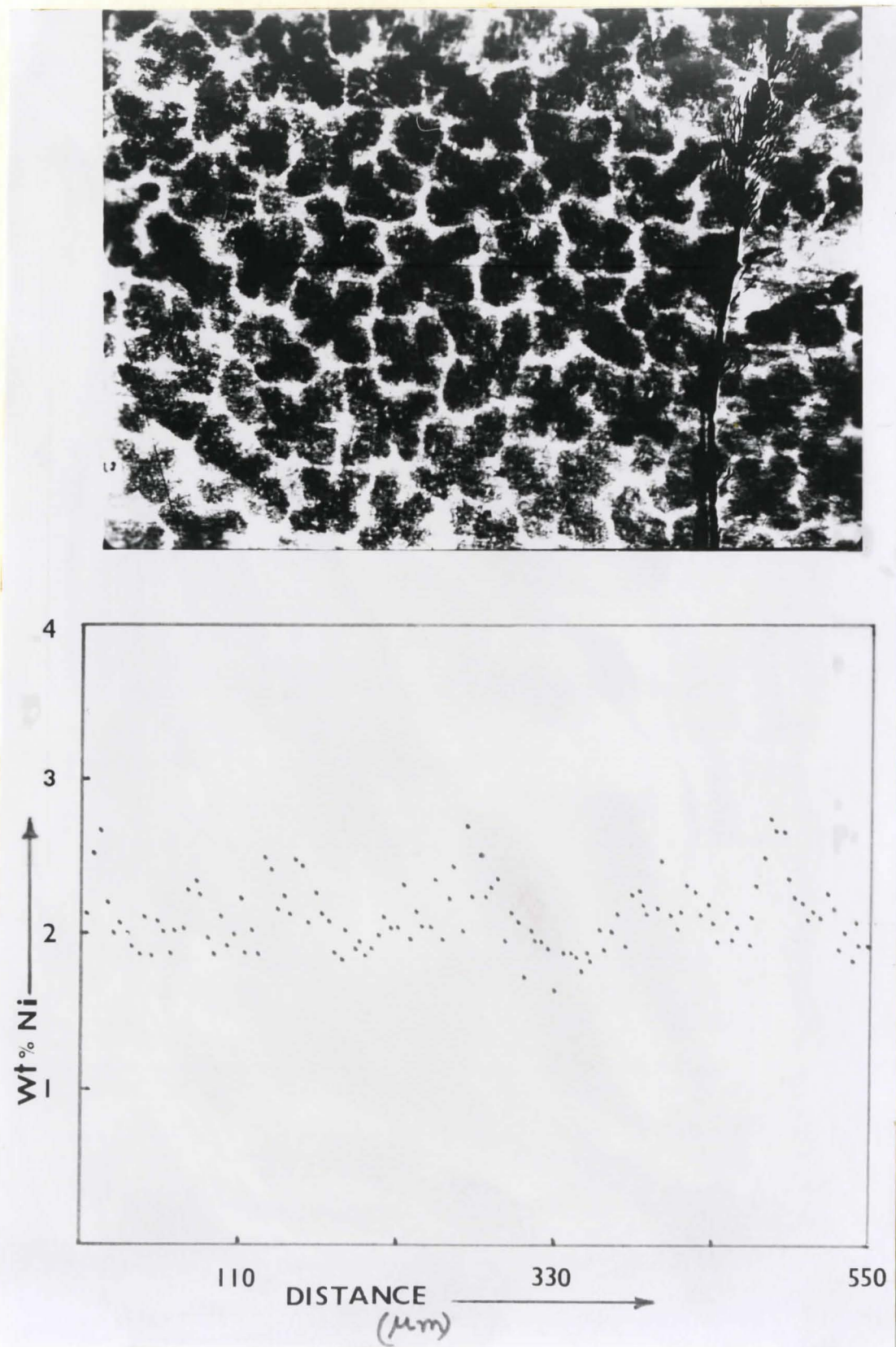
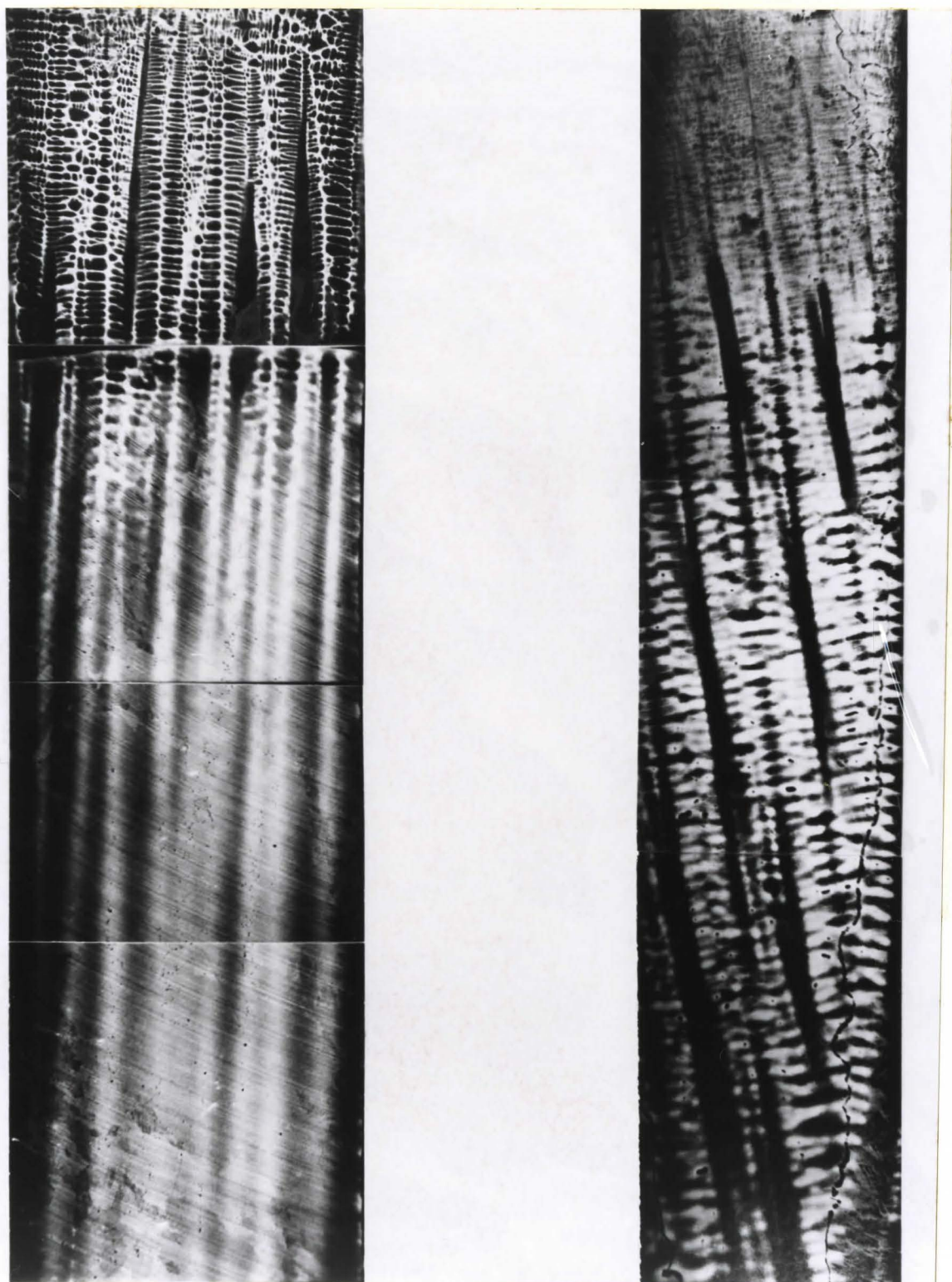


Fig. 5.2.4 Dendritic structure and Ni concentration profile in transverse section of Fe-2.04 wt% Ni -0.32 wt% C Alloy (elliptical button)

Mag. 60x

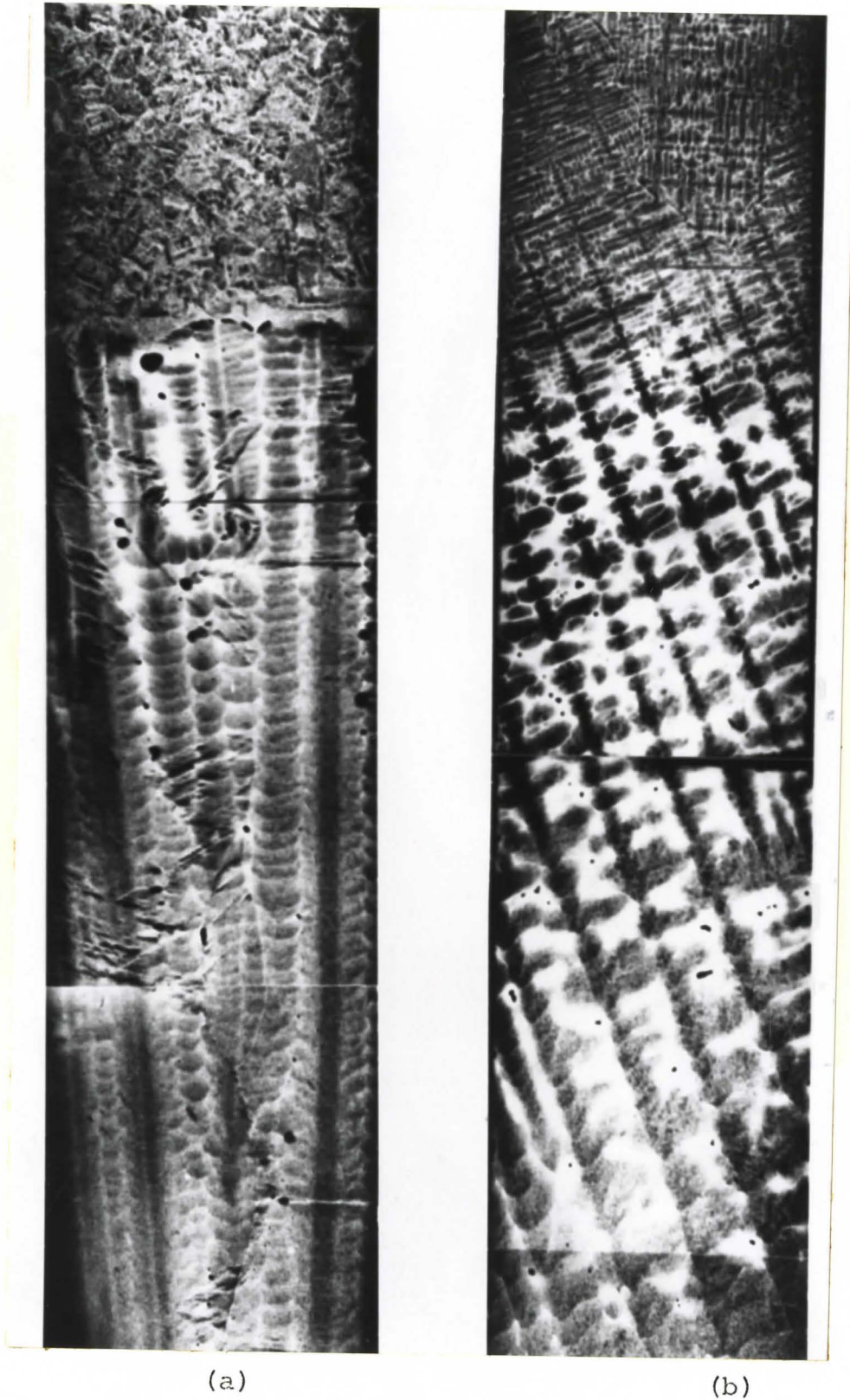


(a)

(b)

Fig. 5.2.5 Fe-2.06 wt% Ni alloy directionally solidified, section parallel to macroscopic growth direction
 $G = 22.7^{\circ}\text{C}/\text{cm}$ $R = 100 \text{ mm}/\text{hrs}$

(b) Fe-1.98 wt% Ni-0.48 wt% C alloy directionally solidified section parallel to macroscopic growth direction. $G = 22.7^{\circ}\text{C}/\text{cm}$ $R = 100 \text{ mm}/\text{hrs}$
 Mag.22x



(a)

(b)

- Fig. 5.2.6 (a) Directionally solidified Fe-2.01 wt% Ni-0.58 wt% C alloy; section parallel for macroscopic growth direction. $G = 22.7^{\circ}\text{C}/\text{cm}$ $R = 100 \text{ mm}/\text{hr}$
- (b) Directionally solidified Fe-2.02 wt% Ni-0.40 wt% C alloy; section parallel for macroscopic growth direction. $G = 22.7^{\circ}\text{C}/\text{cm}$ $R = 100 \text{ mm}/\text{hr}$

Mag. 22x

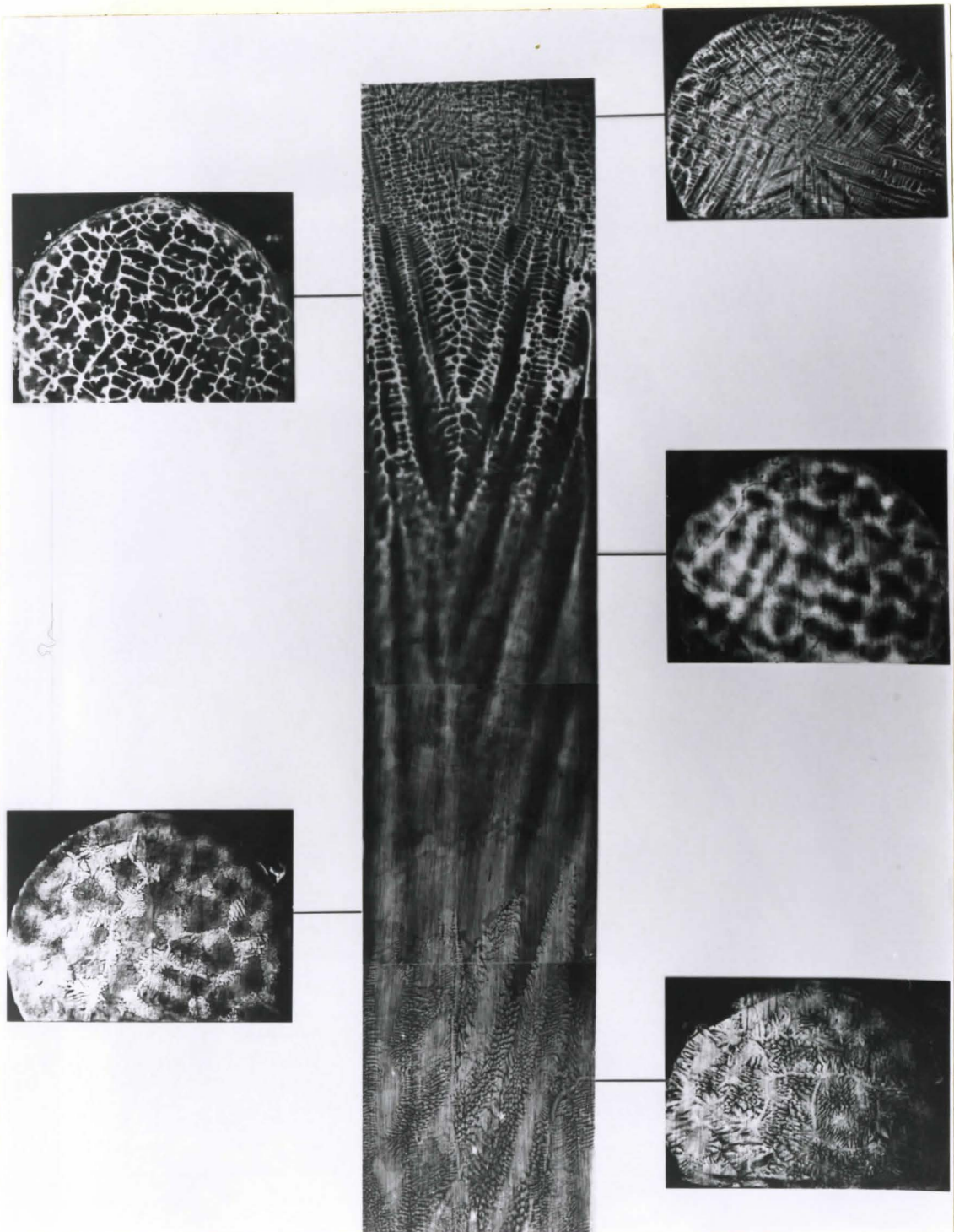
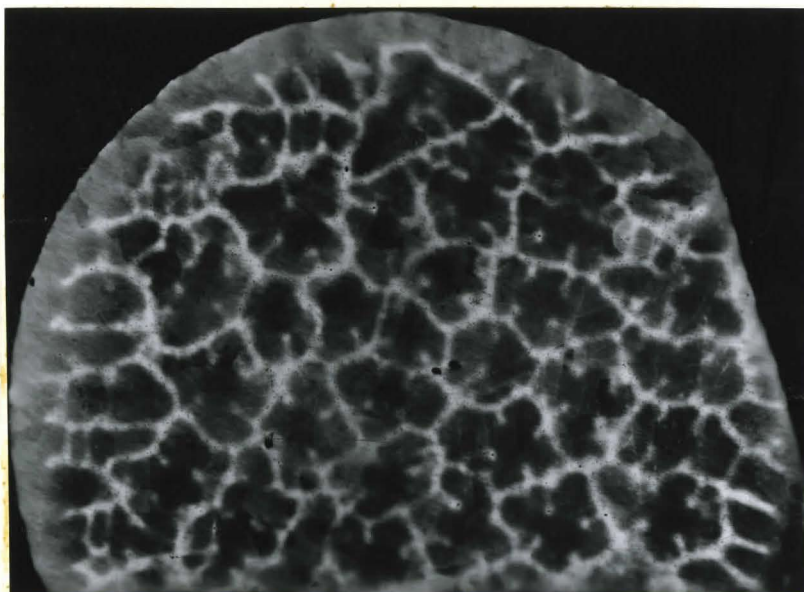
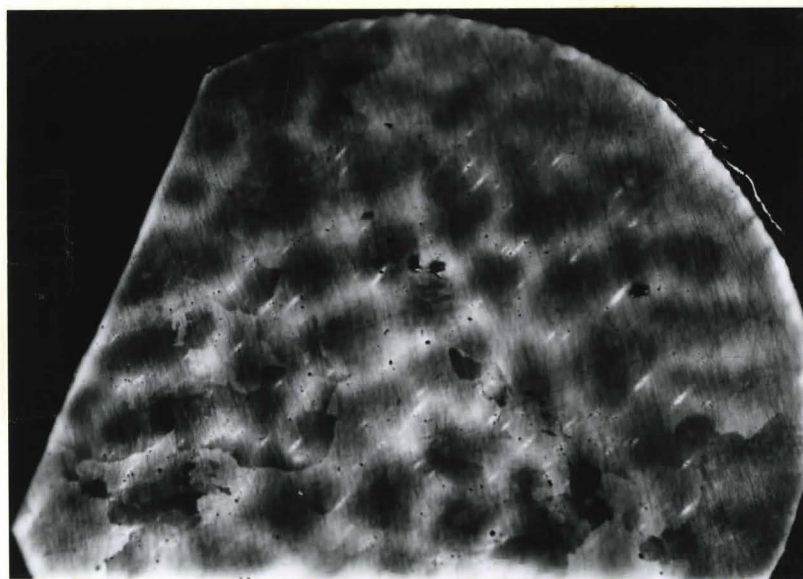


Fig. 5.2.7 Directionally solidified Fe-2.9028 wt% Ni alloy,
section parallel to macroscopic growth direction
 $G = 22.7^{\circ}\text{C}/\text{cm}$ $R = 100 \text{ mm}/\text{hr}$

Mag. 22x



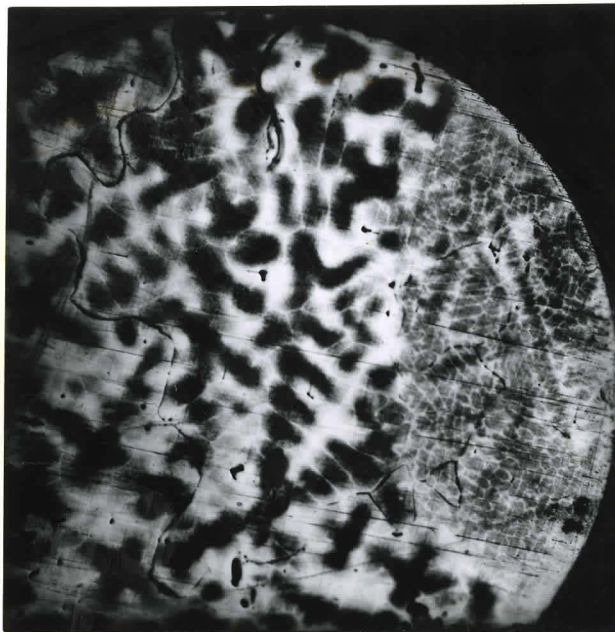
(a)



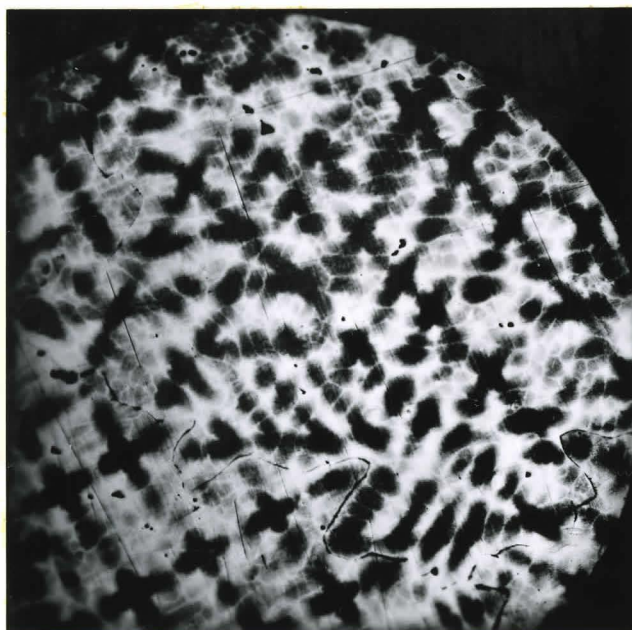
(b)

Fig. 5.2.8 Transverse sections of the directionally solidified Fe-2.06 wt% Ni alloy
(a) Top section (b) 3.6 mm from top

Mag. 22x



(a)



(b)

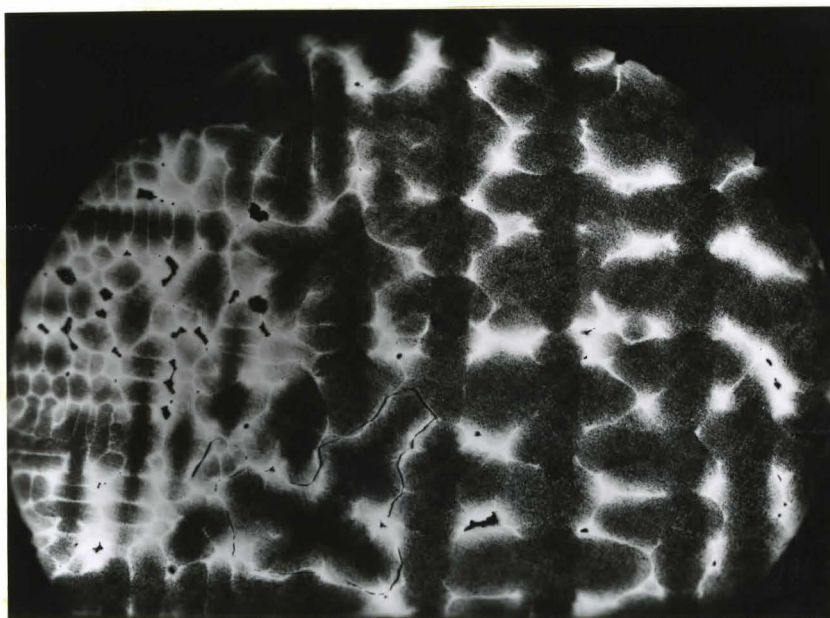
Fig. 5.2.9 Transverse sections of the directionally solidified Fe-1.98 wt% Ni-0.48 wt% C alloy

- (a) Top section
- (b) 3.1 mm from top

Mag. 22x



(a)

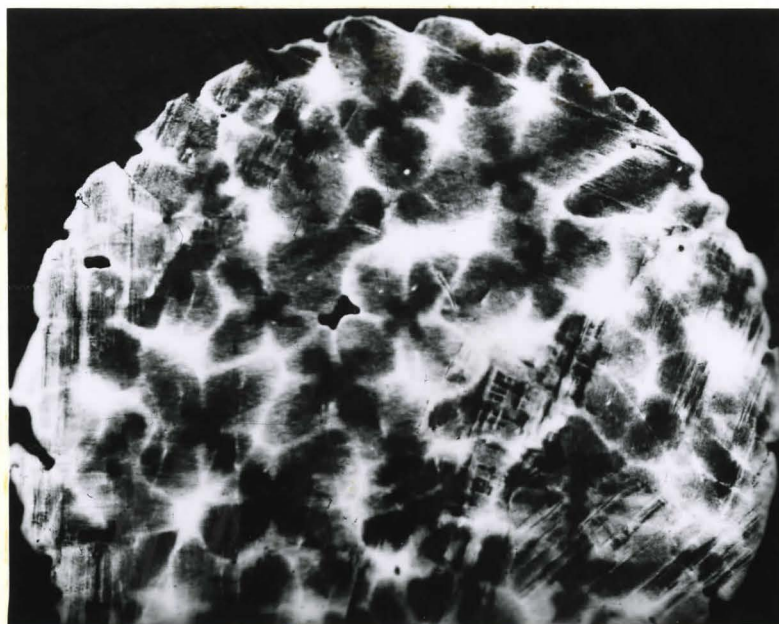


(b)

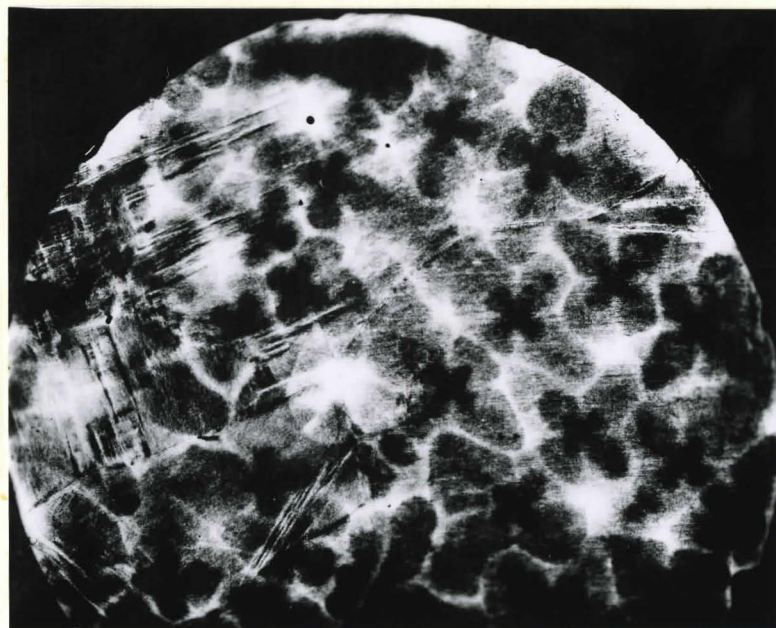
Fig. 5.2.10 Transverse sections of the directionally solidified Fe-2.02 wt% Ni - 0.4 wt% C alloy

(a) Top section
(b) 5.1 mm from top

Mag. 22x



(a)



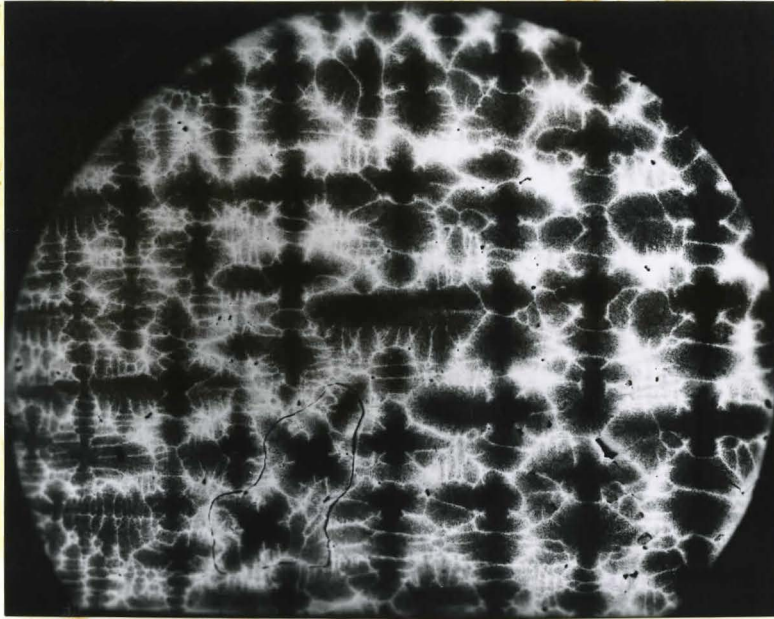
(b)

Fig. 5.2.11 Transverse section of the directionally solidified Fe-2.01 wt% Ni-0.58 wt% C alloy

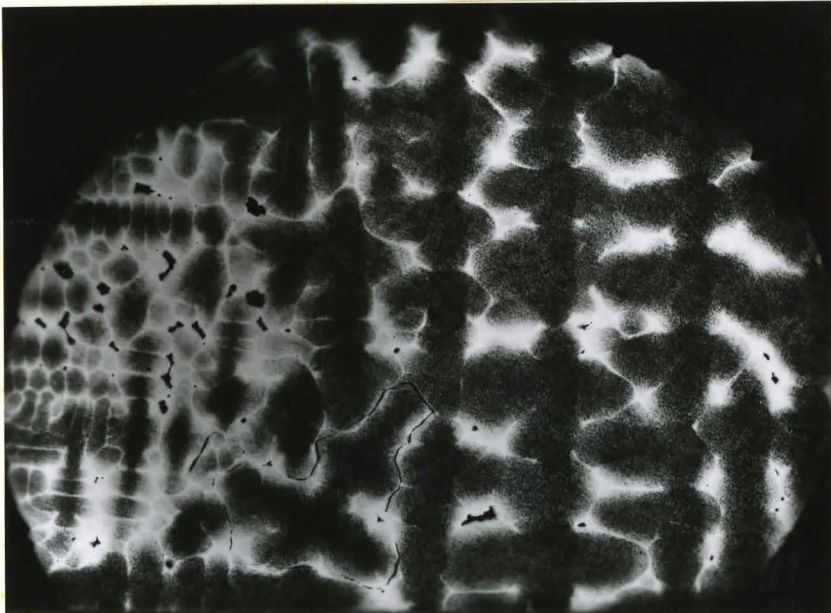
(a) Top section

(b) 3.07 mm from top

Mag. 22x



(a)

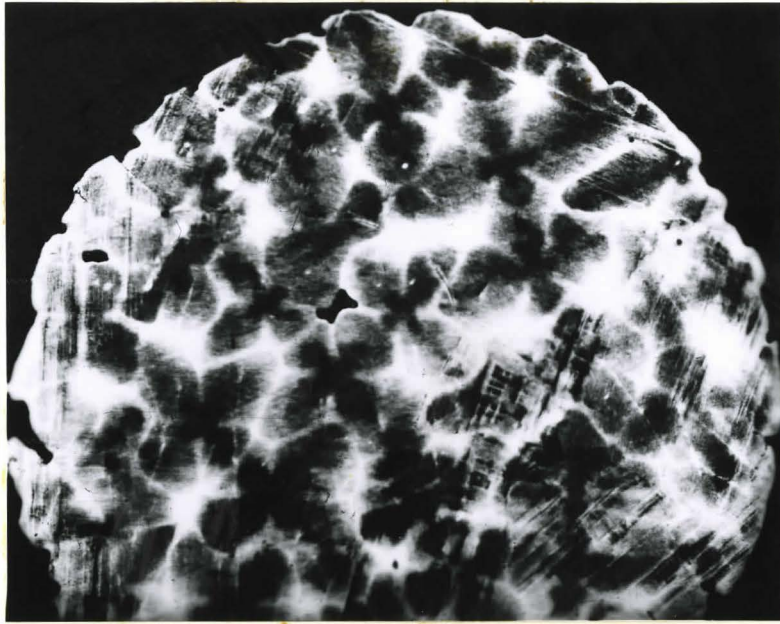


(b)

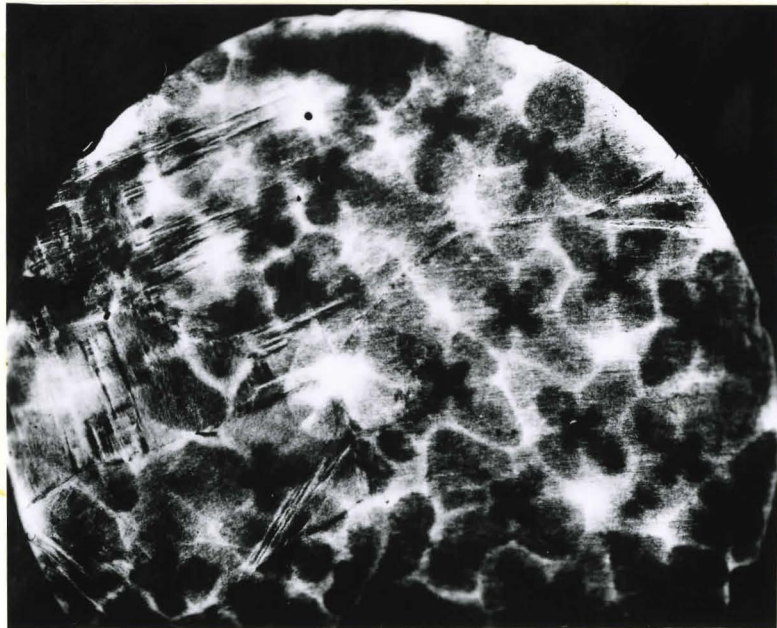
Fig. 5.2.10 Transverse sections of the directionally solidified Fe-2.02 wt% Ni - 0.4 wt% C alloy

- (a) Top section
- (b) 5.1 mm from top

Mag. 22x



(a)



(b)

Fig. 5.2.11 Transverse section of the directionally solidified Fe-2.01 wt% Ni-0.58 wt% C alloy

(a) Top section

(b) 3.07 mm from top

Mag. 22x

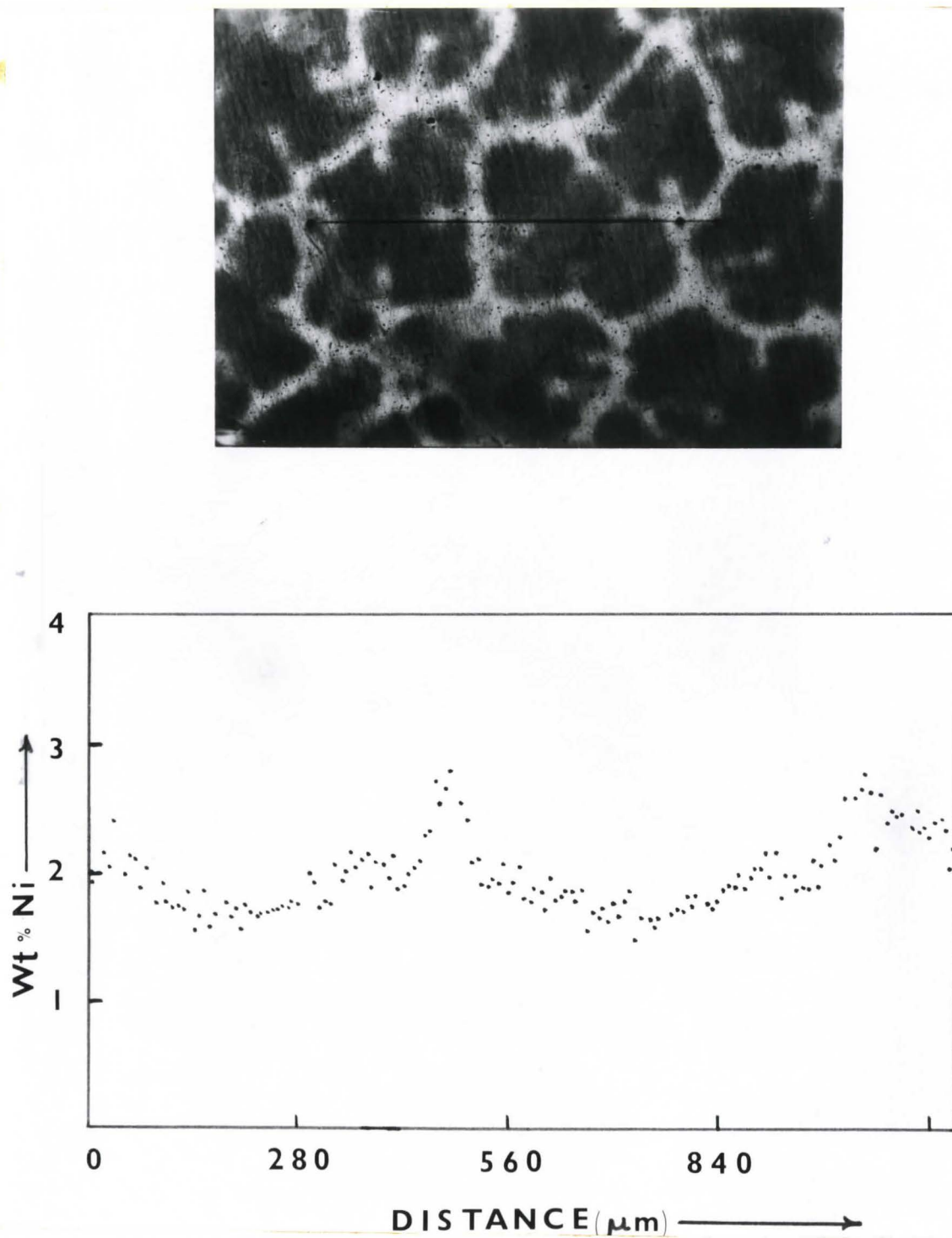


Fig. 5.2.12(a) Dendritic structure and Ni concentration profile in the top transverse section of Fe-2.06 wt% Ni alloy

Mag. 60x

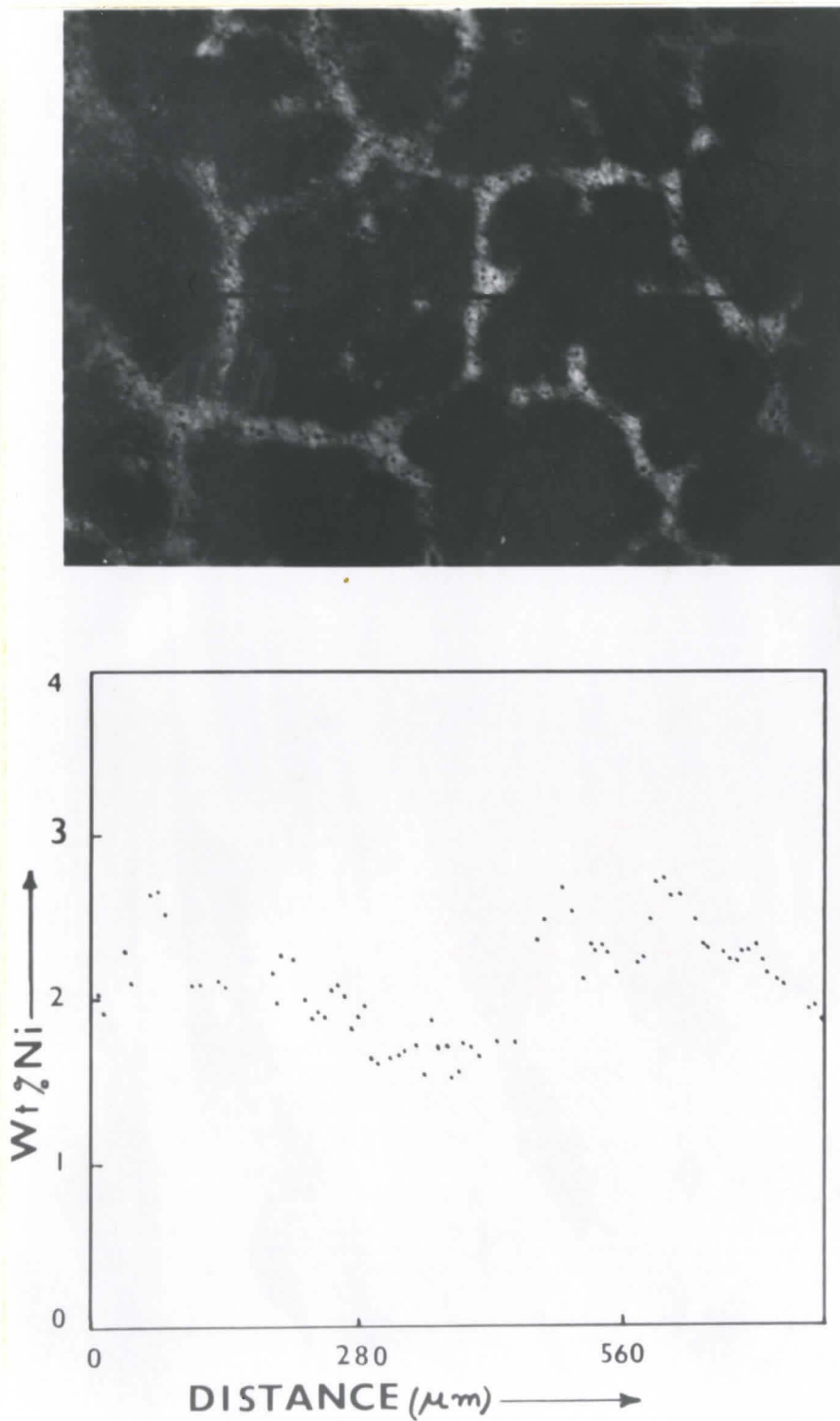


Fig. 5.2.12(b) Dendritic structure and concentration profile of Ni in Fe-2.06 wt% Ni alloy (section just below the one in fig. 5.2.12(a))

Mag. 60x

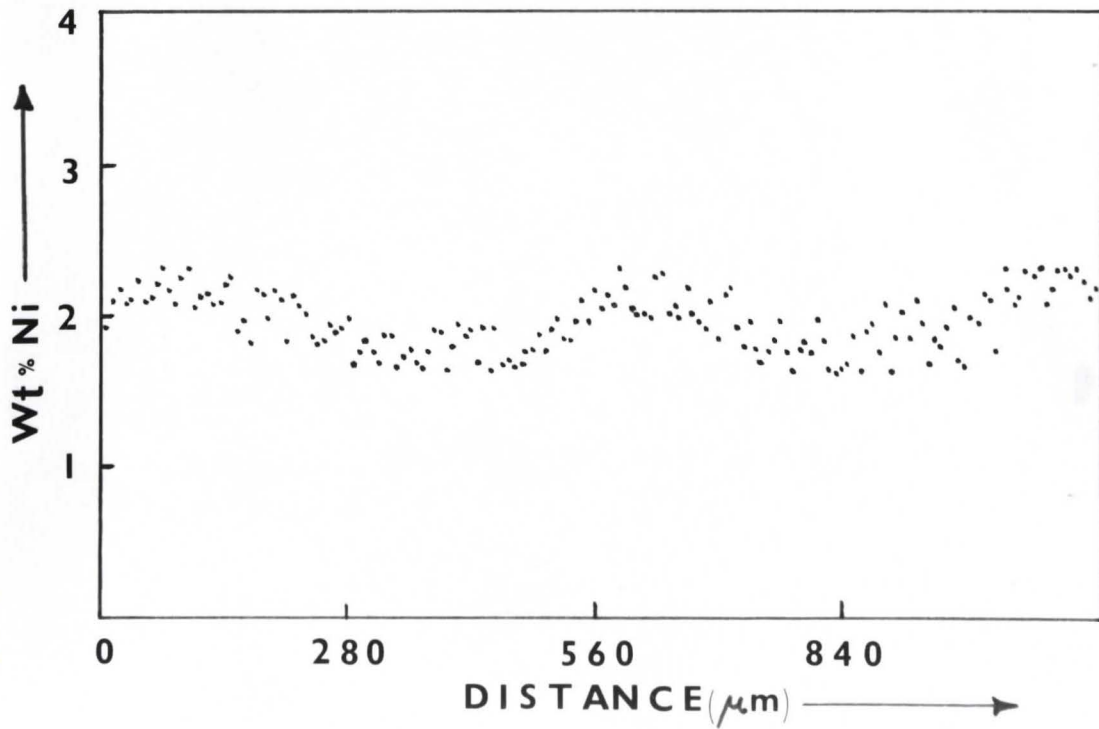


Fig. 5.2.13 Dendritic structure and Ni concentration Profile in the Bottom transverse section of Fe-2.06 wt% Ni alloy

Mag. 60x

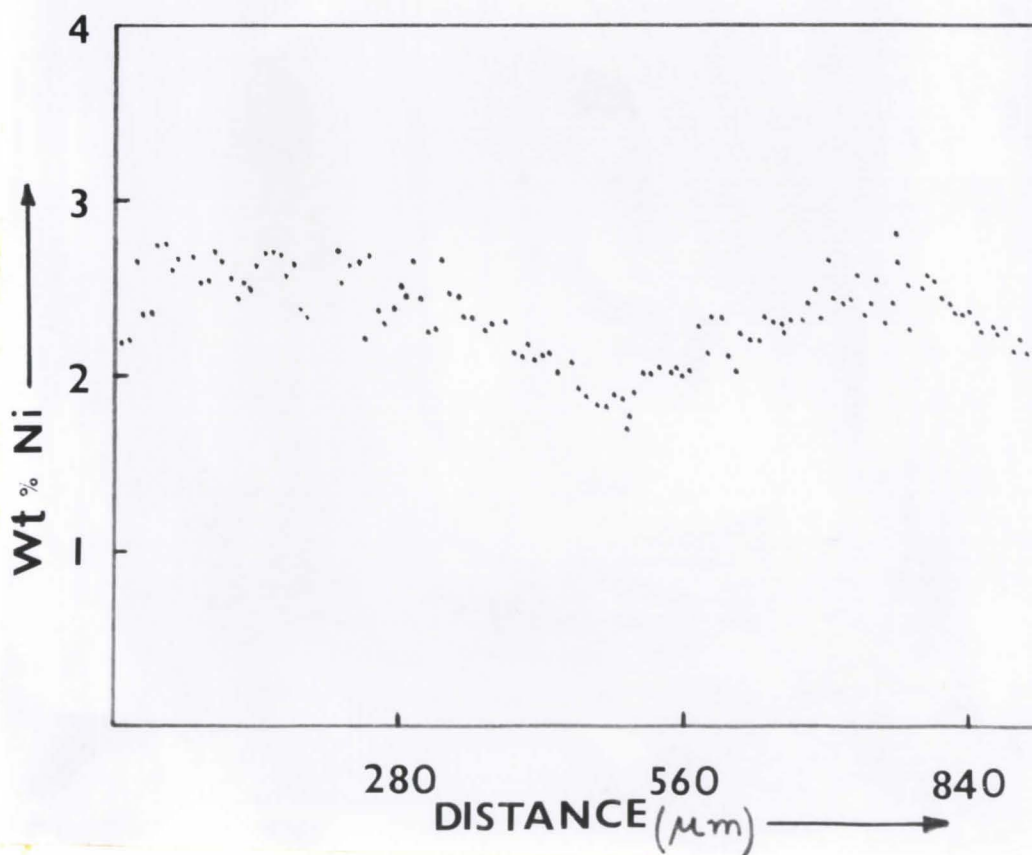
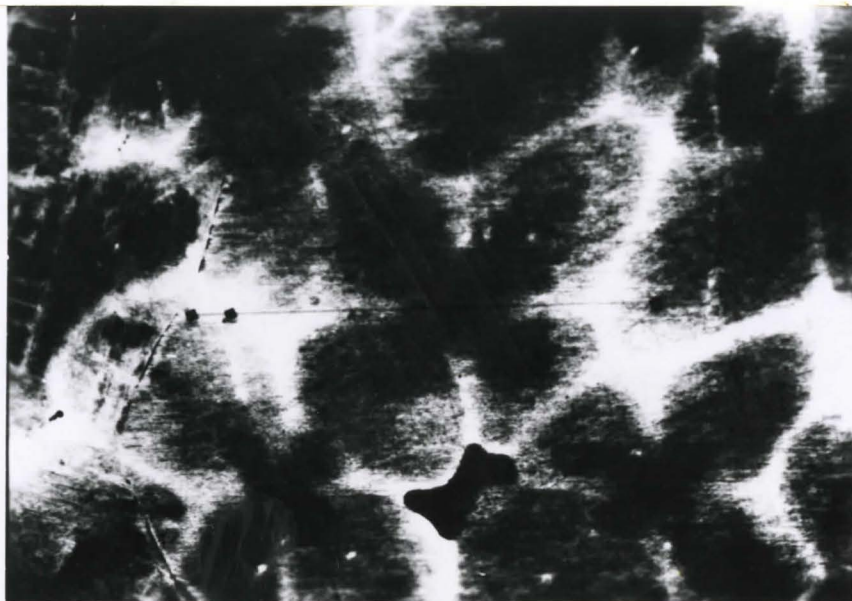


Fig. 5.2.14 Dendritic structure and Ni concentration profile in the top transverse section of Fe-2.01 wt% Ni-0.58 wt% C alloy

Mag. 60x

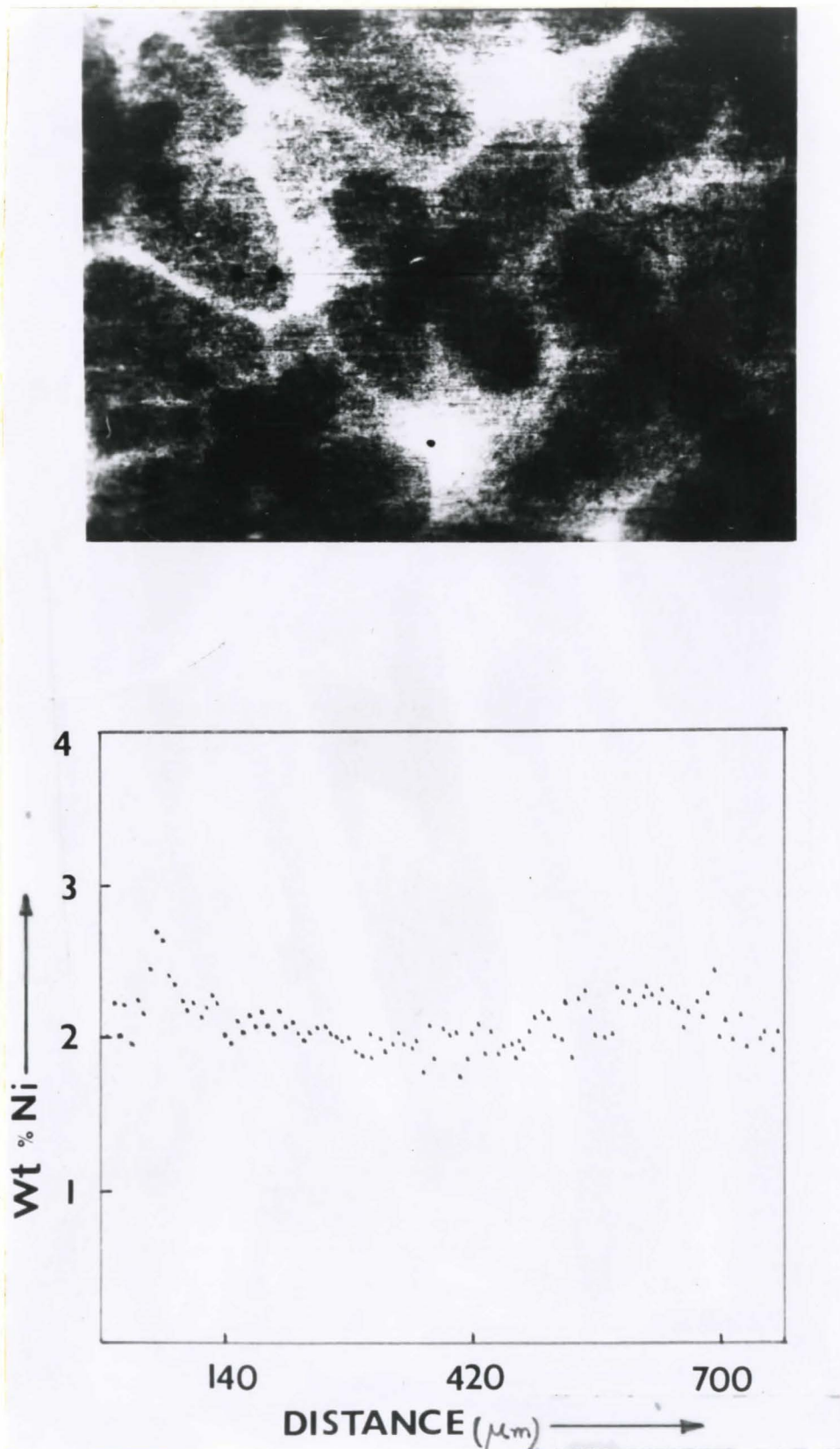


Fig. 5.2.15 Dendritic structure and Ni concentration profile in bottom transverse section of Fe-2.01 wt% Ni-0.58 wt% C alloy

Mag. 60x

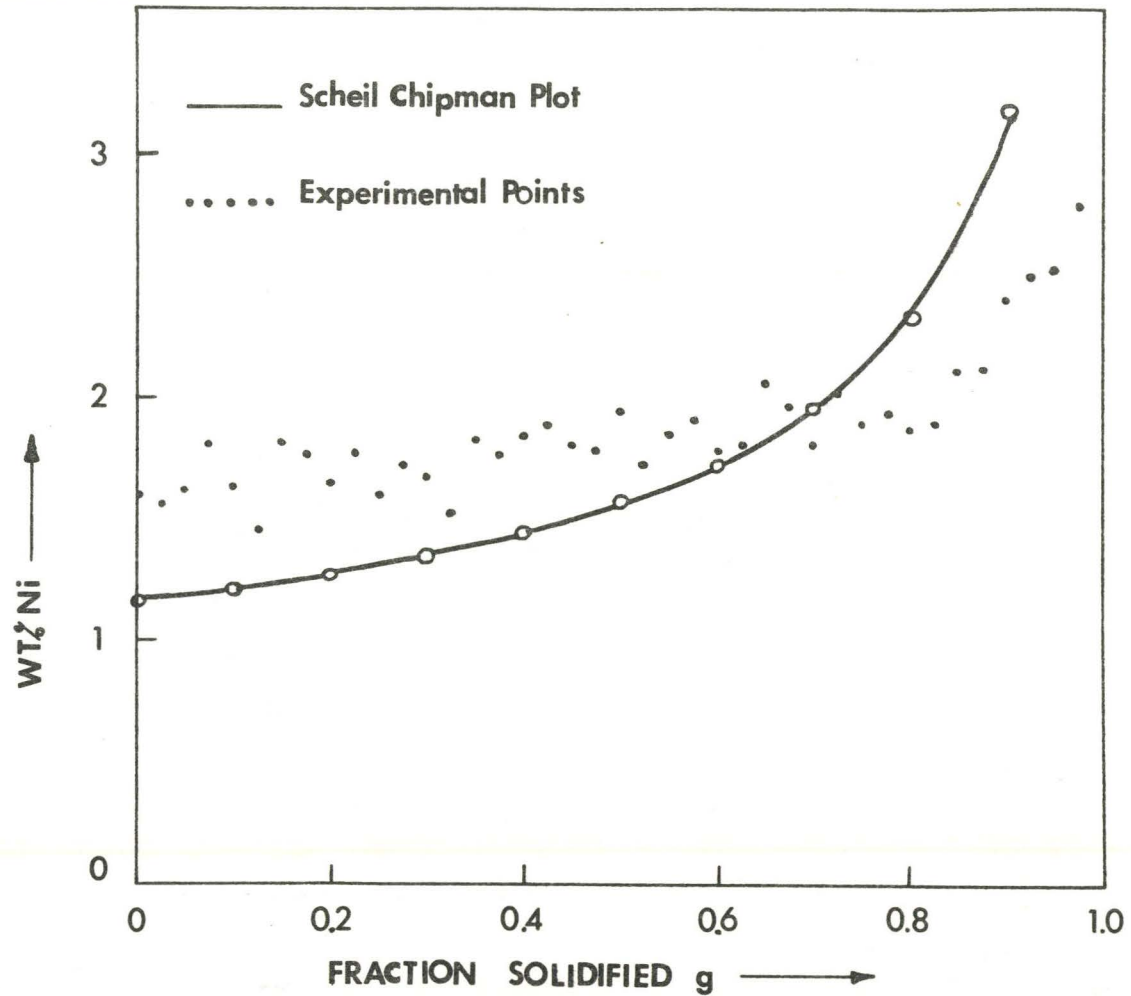


Fig. 5.2.16 Comparison of Scheil Chipman Plot with the concentration profile of Ni in Fe-2.06 wt% Ni alloy

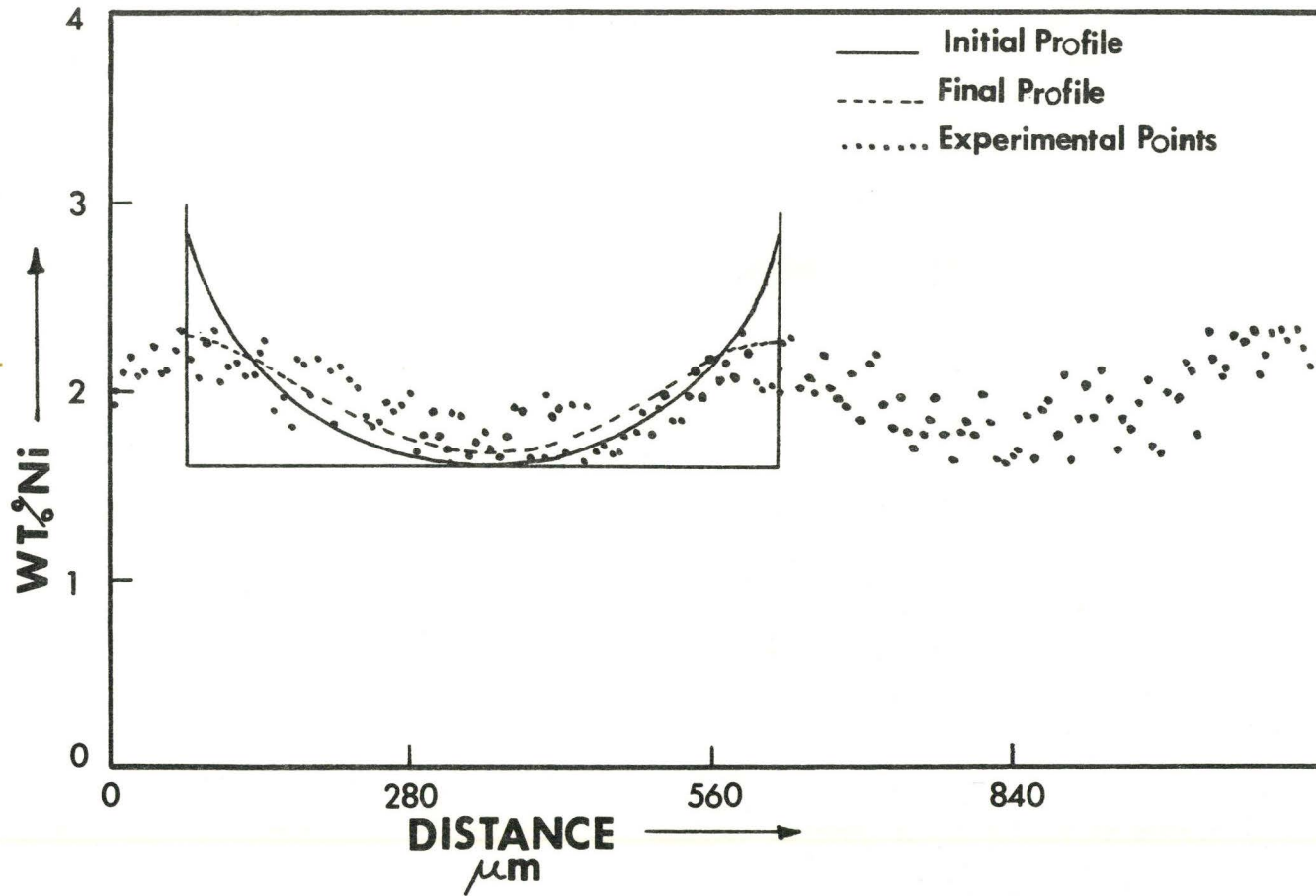


Fig. 5.2.17 Decay of the initial segregation profile of Ni in Fe-2.06 wt% Ni Binary alloy

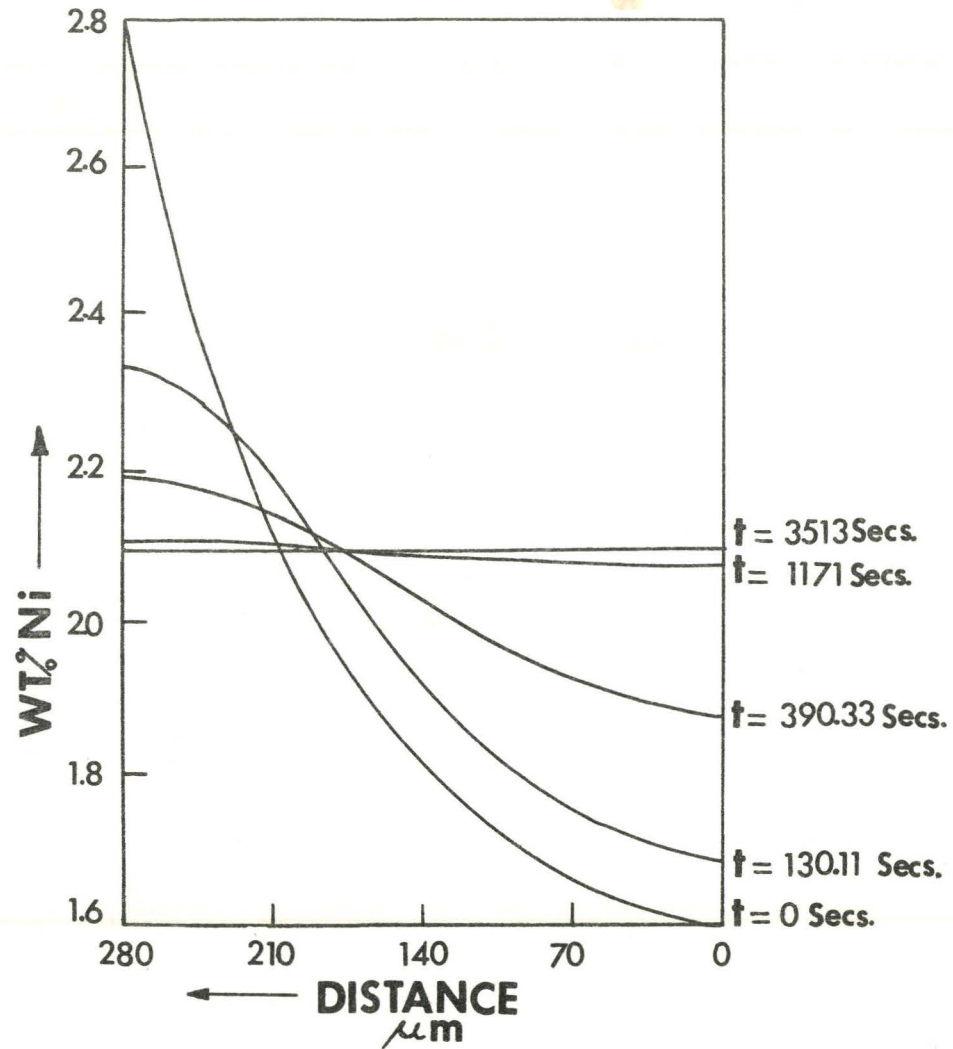


Fig. 5.2.18 Computed decay curves for the Dendritic solidification for Fe-2.06 wt% Ni alloy assuming cylindrical geometry

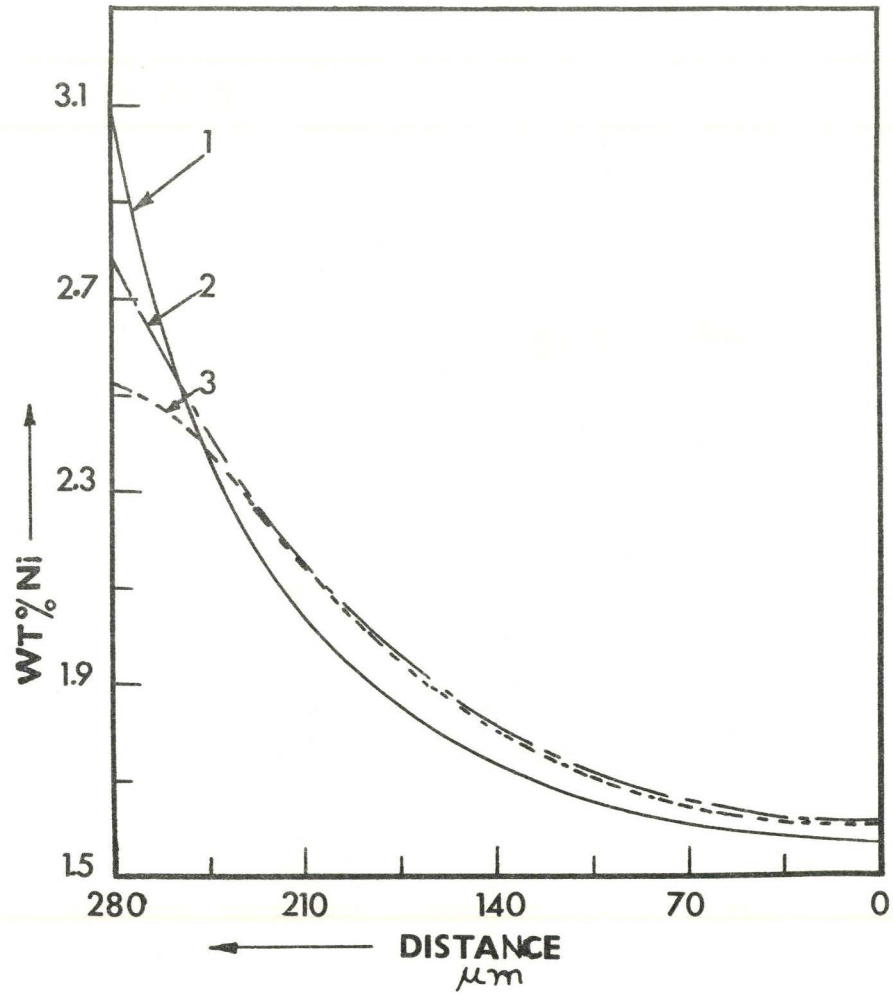


Fig. 5.2.19 Homogenisation during solidification for Fe-2.06 wt% Ni Binary alloy

- (1) Assumed Ni distribution before solidification
- (2) Ni distribution after solidification (experimental)
- (3) Ni distribution after solidification (computed from 1)